

# **Study on Failure of Landslide Dam and Slope**

**By**

**REGMI Ram Krishna**

2011



## **Abstract**

Landslide dams, typically comprise unconsolidated and poorly sorted material, are viable to rapid failure which may result significant and sudden flood risk in the downstream area. Hence serious natural hazard may occur so that likely peak flow rate should be assessed rapidly so as to enable preparation of adequate mitigation strategies. Most of the landslide dams break down due to the over flow of the lake water due to a gentle and gradual erosion rather than by abrupt overflow. It may also fail by sudden sliding or progressive failure. In depth knowledge of the failure mechanisms of the landslide dam and measured data are still being lacked. Numerical models from international literature allow to roughly computing the hydrograph resulting from the dam failure, however not giving any indications regarding the whole dam stability.

Rainfall-induced slope failures are generally caused by increased pore pressures and seepage forces during periods of intense rainfall. During a rainfall event, a wetting front goes deeper into the slope, resulting in a gradual increase of the water content and a decrease of the negative pore-water pressure. This negative pore-water pressure is referred to as matric suction when referenced to the pore air pressure that contributes towards the stability of unsaturated soil slopes. The loss of suction causes a decrease in shear strength of the soil on the potential failure surface and finally triggers the failure. Since the shape of such failure surfaces and the seepage flow process within a slope are 3D (Three-dimensional) in nature, numerical assessment of 2D (Two-dimensional) soil slope stability is insufficient.

Using the information obtained from the natural slopes it is difficult to explain slope failure mechanisms because it is impossible to know the exact failure site, the time of failure, and soil conditions at failure. Experiments using slope models with simple conditions are one useful approach to study the process of slope failure. Experimental study for rainfall induced slope failure was carried out by preparing a sandy soil model slope inside a rectangular sloped flume so as to measure moisture profiles, air pressure head profiles, surface water forefront propagation, downstream seepage out flow and three dimensional failure surface within the body of the model slope. Profile probes consisting four sensors were used to measure the temporal variation of moisture content and pressure transducers were used to measure the temporal variation of air pressure at different locations inside the body of the model slope. Measuring scales were placed in vertical position on the top surface of the model slope in its central longitudinal section for measuring the surface water forefront propagation. Downstream seepage outflow was measured by collecting outflow seepage water in a measuring cylinder.

Red colored sediment strips and red colored cotton threads were placed respectively at the side wall faces and inside the body, normal to the flume bed, so as to measure the failure surface after sliding. Digital video cameras were used for capturing the surface water forefront propagation, initiation of slope failure process and movement of the failure mass.

In the experiment, the artificial rainfall provided by the simulators was not uniform due to the power fluctuation in the water pump, losses in water supply pipes, temperature variation, etc. Rainfall intensity over the flume was measured at different locations so as to provide the similar rainfall intensity and distribution pattern in numerical simulation. It is difficult to observe the three dimensional view of the failure surface in rectangular flume shape. So, the rectangular shape of the flume was modified to V-shape in its bottom having cross slope of  $20^\circ$ . The experiments were carried out on  $23^\circ$  and  $28^\circ$  flume slope.

Throughout much of the world, slopes exist in residual soil deposits. Such soils are often unsaturated, and the conventional approach which assumes only water phase flow in seepage analysis is inadequate. A numerical model to analyze the influence of air phase in seepage flow process within the soil domain is also important. No attempt has been yet made to analyze the seepage flow within the soil slope for its stability analysis by considering air flow within the soil. In this study 3D Conventional water-phase (one-phase) as well as water-air two-phase seepage flow numerical simulation models was developed individually for calculation of pore water pressure and moisture content required for the stability analysis of the landslide dam and slope.

It is necessary to identify either there is surface runoff produced or not in a soil slope during a rainfall event while analyzing the seepage and stability of such slopes. Runoff produced by rainfall may result erosion/deposition process on the surface of the slope. The depth of runoff has vital role in the seepage process within the soil domain so that 2D surface flow and erosion/deposition model was used to compute the surface water head of the runoff produced by the rainfall and erosion/deposition on the surface of the model slope, by the finite difference form of the governing equations.

Limit equilibrium method of slices is widely used for slope stability analysis due to its simplicity and applicability. It usually involves two steps; one for the calculation of the factor of safety and the other for locating the most critical slip surface which yields the minimal factor of safety. In most of the studies Janbu's simplified method that satisfies only the force equilibrium,

has been used in the slope stability analysis. However, it is necessary to satisfy all the conditions of equilibrium to get the more accurate result. So this study utilizes Janbu's simplified method as well as extended Spencer method by incorporating it into an effective minimization procedure based on dynamic programming by which the minimal factor of safety and the corresponding critical non circular slip surface were determined simultaneously. Numerical simulation results and experimental measurements are satisfactorily in agreement in terms of moisture movement, seepage outflow rate, surface water forefront propagation, predicted critical slip surfaces and time of failure of the considered slope.

Investigation of sudden sliding of landslide dam was carried out in 2D and 3D. In 2D study constant water head and steady water discharge was provided in the upstream reservoir; where as in 3D only steady water discharge was provided in the reservoir. 2D and 3D conventional water-phase as well as water-air two-phase seepage flow numerical simulation models were developed individually for seepage calculation inside the body of landslide dam. Seepage flow model was then combined with respective 2D and 3D transient slope stability model to predict the failure of dam due to sudden sliding. Janbu's simplified method as well as Spencer/extended Spencer method was used to locate the critical slip surface of a general slope of the dam. Numerical simulation results and experimental measurements are quite close in terms of moisture movement, predicted critical slip surfaces and time of failure of the dam.

In overall, simulation results obtained by two-phase seepage flow model and Spencer/extended Spencer method are comparatively in good agreement with the experimentally observed results than that of conventional seepage flow model and Janbu's simplified method.

**Key Words:** *rainfall, seepage analysis, variably saturated soil, two-phase flow, numerical modeling, slope stability, model slope, failure surface*



# Acknowledgements

The completion of this thesis was made possible by the contributions, knowledge, kindness, and support of many individuals. First of all, I would like to express my deepest sense of gratitude to my supervisor, Professor Dr. Hajime Nakagawa, Disaster Prevention Research Institute (DPRI), Kyoto University, for his patient guidance, support, encouragement, and excellent advice throughout my study period.

I am deeply grateful to my thesis reviewers, Professor Dr. Masaharu Fujita and Associate professor Dr. Kenji Kawaike, DPRI, Kyoto University, for their valuable comments and suggestions to refine the thesis.

I wish to express my sincere gratitude to Dr. Yasuyuki Baba and Dr. Hao Zhang, for their guidance, suggestions during my study. I warmly thank Dr. Ripendra Awal and Dr. Badri Bhakta Shrestha for their valuable suggestions, discussions and friendly help in all aspects of my study.

I am indebted to my all colleagues of River Disaster Prevention System, DPRI, Kyoto University for their kind cooperation and unforgettable friendship. I am especially grateful to Dr. Dong-Kuen Lee, Mr. Hiroshi Teraguchi, Mr. Hideaki Mizutani, Mr. Amir Reza Mansoori, Mr. Yeonjung Kim, Mr. Seung Soo Lee, Mr. Takaharu Utsumi, Mr. Yasunori Nanbu, Mr. Yasutaka Saito, Mr. Toshimasa Mataga, Mr. Satoshi Kohda, Mr. Atsushi Shimizu, Mr. Sohshi Yoneda, Ms. Akiko Takao, Mr. Shiro Nakanishi, Mr. Taichi Tachikawa, Mr. Tomoyuki Ide, Mr. Masatoshi Ogura And Mr.Horoaki Kouge.

I would like to thank all the professors and friends in the Research Center for Fluvial and Costal Disaster, Disaster Prevention Research Institute of Kyoto University, who have made my academic experience rich and memorable. I would like to thank Mr. Seiji Fujihara, Mr. Kazuhiro Nishimura, Mr.Yoshinori Yoshida, Mrs. Natsuyo Sugimura and all the staffs in Ujigawa Open Laboratory, Disaster Prevention Research Institute of Kyoto University for their support in routine administrative process and experiment.

I am also greatly indebted to my M. Sc. thesis supervisor, Professor Dr. Narendra Man Shakya Institute of Engineering, Tribhuvan University, Nepal, for exposing me to academic research

activities and encouraged to come here in Japan.

With the greatest appreciation I wish to express my obligation to the Monbukagakusho (Ministry of Education, Culture, Sports, Science and Technology, Japan) for the financial support. The fund given to this research by Japan Society for the Promotion of Science (JSPS) Grant-in-Aid for Scientific Research (B) 22360197 (Hajime Nakagawa, Kyoto University) is sincerely acknowledged.

I take this opportunity to express my profound gratitude to my beloved parents, Nil Prasad Regmi and Menuka Regmi, my grandfather Udaya Nath Regmi and all family members for their encouragement and loving support. I feel indebted and dedicate this thesis to my wife Sushila Nepal and my son Aradhya Regmi.

# Table of Contents

<b>Abstract</b>	i
<b>Acknowledgements</b>	v
<b>1 Introduction</b>	
1.1 General	1
1.2 Objectives of the research	8
1.3 Literature review	8
1.3.1 Landslide dam	8
1.3.2 Rainfall induced slope failure	11
1.4 Outlines of the dissertation	14
<b>2 Experimental Studies on Slope Failure</b>	
2.1 Introduction	17
2.2 Experimental set-up and measurement apparatus	17
2.2.1 Laboratory flume	17
2.2.2 Multi-fold pF meter	19
2.2.3 Profile probe	21
2.2.4 Pressure transducer	22
2.2.5 Point gauge	23
2.3 Test procedures	24
2.4 Results and discussions	26
Summary	32
<b>3 Analysis of Rainfall Induced Slope Failure</b>	
3.1 Introduction	33
3.2 Seepage flow analysis	34
3.2.1 Seepage flow model	34
Governing equations	34
Solution approach	36
3.2.2 Surface flow and erosion/deposition model	38
Governing equations	38
Solution approach	41

3.2.3 Boundary conditions	44
3.2.4 Results and discussions	45
3.3 Slope stability analysis	65
3.3.1 Janbu's simplified method	66
3.3.2 Extended Spencer method	66
3.3.3 Dynamic programming search procedure	67
3.3.4 Results and discussions	71
Summary	85
<b>4 Analysis of Landslide Dam Failure</b>	
4.1 Introduction	87
4.2 Seepage flow model	88
4.2.1 Governing equations	88
Solution approach	89
4.2.2 Boundary conditions	89
4.3 Slope stability model	90
4.3.1 Janbu's simplified method	90
4.3.2 Spencer method	90
4.3.3 Dynamic programming search procedure	91
4.4 Results and discussions	93
Summary	107
<b>5 Conclusions and Recommendations</b>	
5.1 Conclusions	109
5.2 Recommendations for future researches	112
<b>References</b>	115
<b>List of Figures</b>	125
<b>List of Tables</b>	131
<b>Curriculum Vitae</b>	133
<b>Papers Based on the Thesis</b>	135

# Chapter 1

## Introduction

### 1.1 General

Landslide dams (i.e., the natural blockage of river channels by hill slope-derived mass movements, Costa and Schuster, 1988) are natural phenomena with great relevance on geomorphological conditions and on the safety of people. In areas placed upstream, respect to the river dammed section, waters blocked by the dam may provoke floods spreading for kilometers, causing damage to human activities and interrupting communication lines. Catastrophic outburst floods and/or debris flows can be triggered by a rapid dam failure with exceptional rates of sediment erosion and deposition along the downstream part of the valley.

Landslide dams commonly form in mountainous areas of high relief (Costa and Schuster, 1988), where there is sufficient input from both tectonic (earthquakes, hill slope gradients, relief) and climatic (precipitation, snowmelt) controls. About 90% of some 390 landslide dams examined worldwide were triggered by either rainstorms/snowmelts or earthquakes (Schuster, 1993), although other less common causes, such as volcanic (e.g., Umbal and Rodolfo, 1996; Melekestsev et al., 1999) or even anthropogenic activity (e.g., Asanza et al., 1992), have been documented. Typologically, 50% examined were triggered by earth slumps and slides; 25% by debris, mud and earth flows; 19% rock and debris avalanches; and 6% sensitive clay failures and rock and earth falls (Schuster, 1993). The spatial distribution of landslide dams are governed by four groups of factors as seismic intensity (peak acceleration, duration of strong shaking), high slope gradient and topography, lithology and weathering properties and soil moisture and groundwater content (Schuster et al., 1998).

Landslide dams fail by a variety of processes including overtopping, internal seepage erosion, overtopping by a landslide-generated wave, slope failure of upstream or downstream face, and the effects of human activity, usually an attempt to excavate a spillway over the debris dam. Many landslide dams fail shortly after their formation (Costa and Schuster, 1988). Based on 73 cases from the literature and the authors' experience 27% of the landslide dams failed less than

one day after formation, 41% failed within one week, 50% failed within ten days, 80% failed within six months and 85% failed within a year of formation. Schuster (1993, 1995) argued that about 55% of some 187 investigated examples worldwide had failed within one week of their formation, whereas 89% failed after one year.

Some landslide dams are known to be formed as high as the largest existing artificial dam. The highest known landslide dam of historic times is the Usoi Dam in modern Tajikistan created by a landslide triggered by an earthquake on February 18, 1911 (Risley et al., 2006). It dammed the Murghab River to the height of 500 to 700m to impound more than 60km Sarez Lake 500m deep. Among the most destructive landslide lake outburst floods in recorded history occurred in the Sichuan province of China on 10 June 1786 when the dam on the Dadu River burst, causing a flood that extended 1400km downstream and killed 100,000 people (Schuster and Wieczorek, 2002). In October 1999, 120m high Mount Adams landslide dam was formed in the gorge of the Poerua River New Zealand by falling down about 15 million cubic metres of rock debris from Mount Adams (Davies, 2002). The dam was failed 6 days later, releasing 3 to 4 million cubic metres of water. The Tangjiashan landslide dam, located in the upstream section of the Jian River was the largest and most dangerous landslide dam created by 2008 Wenchuan earthquake (Xu et al., 2009). It was located in the extremely rugged terrain of Tangjiashan Mountain. The dam crest extended approximately 600 m across and 800 m along the valley (Figures 1.1 and 1.2). The dam height was varied from 82 to 124 m and its estimated volume from a rough calculation was  $2.04 \times 10^7 \text{ m}^3$ . In 2010 January 4, a massive landslides hit Hunza (Gilgit Baltistan), sliding two villages into the Hunza river, destroying 26 homes and killing 20 people (Ev-K2-CNR, 2010). This resulted in the blockage of the river and the Karakorum highway creating the Hunza landslide dam (Figures 1.3 and 1.4). The estimated volume of the sliding mass was 30 million  $\text{m}^3$ .

Landslides are denoted by the movement of a mass of rock, debris or earth down a slope (Cruden, 1991). Slope failure is a phenomenon in which a slope moves almost instantaneously due to weakened self retain ability of the earth from rainfall, a rise of underground water level or other similar events. Many individuals living in residential areas would fail to escape from this event, thus resulting in a higher rate of fatalities. Heavy storms rainfall has caused many landslides and slope failures especially in the mountainous area of the world. Slope failure and landslides are common geologic hazards and posed serious threats and globally cause billions of



Figure 1.1 Helicopter view of the artificial spillway in the Tangjiashan landslide dam (*Source: Xu et al., 2009*)



Figure 1.2 Impounded water flowing through the artificial spillway, taken at 11:00 (Beijing time) 10 June 2008 when the discharge reached its maximum (*Source: Liu.,2008*)



Figure 1.3 Hunza landslide dam in Pakistan (*Image courtesy: NASA EO-1team*)



Figure 1.4 View of the lake from the upper side of the Hunza landslide dam (*Source: Ev-K2-CNR*)

dollars in damage and thousands of deaths and injuries each year so that studies on slope stability and slope failure under rainfall are being increasing attention of these days. Landslide or slope failure under heavy rainfall condition is mainly caused by the rise in ground water level, and the increase in pore-water pressure or the decrease in matrix suction of unsaturated soil that resulting decrease in shear strength of soil, which possibility leads to the occurrences of slope failure. Therefore, the importance is the study of saturated unsaturated soil behaviors in evaluation of slope stability under heavy rainfall condition.

Krishnabhir-Kurintar sector of Prithvi highway in Nepal was suffered from frequent slope failure problems every year in the past decade of 2007 (Figures 1.5 and 1.6). This sector is a part of two hundred kilometers long Prithvi highway of Nepal, which connects Kathmandu, the capital with the tourist city, Pokhara. There are many steep slopes all around the Yokohama city in Japan. Many people, buildings, and city infrastructures are on the hilltop, hillside, and bottom of hills and more than 2000 slope failure disasters happened in past (Fang et al., 2003). Some slope failure pictures of different areas of Japan is shown in Figures 1.7 to 1.9.



Figure 1.5 Slope failure in Krishnabhir in 2000 (*Photo Courtesy:* <http://www.nepalitimes.com>)



Figure 1.6 Krishnabhir in 2006, after the bio-engineered slope stabilization (*Photo Courtesy:* <http://www.nepalitimes.com>)



Figure 1.7 Slope failure due to torrential rainfall of the Bai-u front (Minamata City, Kumamoto Prefecture, July 1997) (*Photo Courtesy: MLIT, Japan*)



Figure 1.8 Slope failure due to torrential rainfall of the Bai-u front (Hanakura Area, Kagoshima City, Kagoshima Prefecture August 6, 1993) (*Photo Courtesy: MLIT, Japan*)



Figure 1.9 Slope failure in Uenoyama Area in Kozushima Village (July 2000, Kozushima Village, Tokyo) (*Photo Courtesy: MLIT, Japan*)

Landslides may be very small or very large, and some move slowly and cause damage gradually; whereas others move so rapidly that they can destroy property and take lives suddenly and unexpectedly. In many regions of the world rainfall is considered the most frequent landslide-triggering factor (Corominas, 2001). The frequency and magnitude of rainfall events, together with other factors such as lithology, morphology and land cover, influence the type of landslide (Van Ash et al., 1999; Crosta, 1998). Generally, deep-seated landslides are often triggered by moderate intensity rainfall distributed over long periods whereas superficial landslides such as soil slips and debris flows are triggered by short duration, intense precipitation (Corominas, 2001). During intense rainfall events the variations in pore water pressures distributed within the soil are highly variable depending on the hydraulic conductivity, topography, degree of weathering, and fracturing of the soil. Pore water pressure increases may be directly related to rainfall infiltration and percolation or may be the result of the build-up of a perched or groundwater table (Terlien, 1998). The response of the material involved is largely dependent on its permeability. In high-permeability soils the build-up and dissipation of positive pore pressures during intense precipitation events could be very rapid (Johnson and Sitar, 1990). In these cases slope failures are caused by high intensity rainfall and antecedent rainfall has little influence on landslide occurrence (Corominas, 2001). On the contrary, in low-permeability soils slope failures are caused by long duration-moderate intensity rainfall events; in fact, the reduction in soil suction and the increase in pore water pressures due to antecedent rainfall, considered a necessary condition for landslide occurrence (Sanderson et al., 1996; Wieczorek, 1987).

Critical rainfall amounts that have triggered landslides can be estimated on the basis of a statistical analysis of landslide events and rainfall characteristics (e.g. Caine, 1980; Govi and Sorzana, 1980; Cannon and Ellen, 1985; Crozier, 1986; Kim et al., 1991; Terlien, 1996, 1998; Pasuto and Silvano, 1998; Glade et al., 2000; Sidle and Dhakal, 2002; Jakob and Weatherly, 2003; Ko Ko et al., 2004). When a statistical analysis is impossible due to the lack of data, the hydrological hillslope processes have to be investigated in order to explain the triggering mechanisms of the landslides (e.g. Anderson and Howes, 1985; Brooks and Richards, 1994; Crosta, 1998; Iverson, 2000; Crosta and Del Negro, 2003).

This study aims to predict the failure surface of a slope induced by a rainfall event as well as the landslide dam failure due to sudden sliding, by using combined seepage and slope stability analyses through numerical simulation model and results obtained by laboratory experiments.

In the numerical simulation, only conventional water phase as well as water-air two-phase flow within the soil domain has been considered for seepage flow analysis.

## **1.2 Objectives of the research**

The main objective of this research is development of a numerical model for the investigation of critical failure surface and time of failure of landslide dam as well as the slope due to a rainfall event. The partial objectives of the research are:

- To develop conventional water-phase flow model as well as the water-air two-phase flow model for seepage analysis.
- To develop surface water flow model combined with erosion/deposition model for the evaluation of rainfall produced surface flow.
- To develop slope stability model to investigate the factor of safety and the geometry of critical slip surface using Janbu's simplified method as well as Spencer/extended Spencer method.
- To validate the developed models based on results compared with experiments.

## **1.3 Literature review**

### **1.3.1 Landslide dam**

Landslide dams, typically comprise unconsolidated and poorly sorted material, are viable to rapid failure which may result significant and sudden flood risk in the downstream area. Hence serious natural hazard may occur so that likely peak flow rate should be assessed rapidly so as to enable preparation of adequate mitigation strategies (Davies et al., 2007). In the early stages, it is essential to estimate the flood discharge generated by overflow erosion when a landslide dam forms, which is known to be the most common pattern for a dam failure. It is also necessary to prepare emergency measures for reducing the flood discharge and to install a warning and evacuation system in the downstream residential areas (Morita et al., 2010).

Research on landslide dams is mostly descriptive and site-specific, partly reflecting the difficulty of acquiring accurate or representative geomorphometric data (Costa and Schuster, 1991; Korup, 2002). Consequently, most of the studies focused on assessing susceptibility of

landslide dams to failure (e.g. Butler et al., 1991; Hanisch, 2002) or geomorphic effects of past and likely future events (e.g. Bunza, 2000; Sarkar et al., 2000; Li et al., 2002), rather than explicit geomorphic hazard. The geomorphic hazard posed by landslide dams has remained largely unaddressed; however landslide inventories are increasingly available and utilized for regional-scale hazard assessment (cf. Guzzetti et al., 2002). Davies and Scott (1997) and Davies (2002) presented order-of-magnitude estimates for the probability of a major landslide dam-break flood in the Callery River gorge of South Westland, New Zealand, which is situated immediately upstream of the popular tourist destination of Franz Josef Glacier township.

Landslide dam failure has been frequently studied as an earthen dam failure despite of their differences in geometry, dimensions and material properties. Many researchers (e.g. Takahashi et al., 1994; Mizuyama et al., 2006; Davies et al., 2007; Satofuka et al., 2010) proposed numerical model to estimate the out flow hydrograph resulting from the overtopping failure of landslide dam. Some of them have investigated the erosion process associated with the overflow. However, Takahashi and Kuang (1988) derived a relationship for the shape and length of the landslide dam in a narrow channel with the width and the total volume of the landslide, and also developed a 1D numerical model to predict the hydrograph of debris flow in case of overtopping and sliding.

Takahashi and Nakagawa (1994) developed 2D model to evaluate flood/debris flow hydrograph due to failure of a natural dam by overtopping. As a function of the shear stress on the side wall, lateral erosion velocity was used to model channel enlargement during overtopping. Mizuyama et al. (2004) carried out flume experiments and computer simulation to investigate the erosion mechanism due to overflow. They proposed an empirical method to predict peak flood discharge when an outburst of a landslide dam occurs without any associate landslide. The Tonbi-kuzure landslide dam triggered by an earthquake in 1858 and subsequent debris flow were reproduced by a computer simulation, and downstream Toyama alluvial fan inundation was successfully simulated. Mizuyama (2006) also carried out flume experiments and used 1D two layer model of Takahama et al. (2000) which is applicable to immature debris flow and debris flow to predict outburst discharge. The simulated result indicated that the shape of the landslide dam and the inflow rate are the major parameters determining peak discharge.

Davies et al. (2007) estimated the peak outflow rates from the failure of the Poerua landslide dam in October 1999 from the field investigation, and compared with the results obtained from

physical laboratory modeling, empirical methods, and computer modeling. The laboratory modeling demonstrated the effect of dam batter slopes and valley bed slope on peak outflow; indicating the necessity of refinement for empirical or numerical estimates of peak outflow. Yan et al. (2009) carried out a series of flume experiments over erodible bed to enhance the understanding of landslide dam-break flooding that comprises a complete set of data resources for understanding the dam failure process and for testing mathematical river models as well. Horiuchi et al. (2010) conducted hydraulic model tests focusing on landslide dam erosion by overflow. Several hydraulic parameters, e.g. increased peak discharge of inflowing discharge, temporal changes of sediment-water mixture discharge, sediment grain size and spread of flow width and the control of flash floods by grid-type check dam, were analyzed using experimental data. Debris flow peak discharge obtained by several empirical formulas and preliminary numerical prediction models were compared with the data obtained by the experiment.

Morita et al. (2010) applied a one-dimensional model for river bed variation and flood runoff with two-layer model of Takahama et al. (2000) for immature debris flow and bank erosion model to Tangjiashan landslide dam formed due to the Wenchuan Earthquake in May 2008. Similarly, Satofuka et al. (2010) also applied same model to study Nonoo landslide dam formed by typhoon Nabi in September 2005 in Miyazaki prefecture of Japan, and Tangjiashan landslide dam of China formed in the Wenchuan earthquake in May 2008. The model successfully reproduced the collapse process and flood runoff of the Nonoo landslide dam and an actual runoff hydrograph of the Tangjiashan landslide dam. They also emphasized the need of improvement especially in calculation of side bank erosion model.

Very few numerical models are developed to analyze the stability of the landslide dam. Most of them are applicable for two dimensional analyses. Awal et al. (2008) have developed a model that can predict the failure time and failure mode either due to overtopping or due to sliding as well as the resulting water and sediment flow hydrographs. Awal et al. (2009) have investigated the sudden sliding failure of landslide dam in three dimensions. In the above mentioned studies Janbu's simplified method that satisfies only the force equilibrium, has been used in the slope stability analysis. However, it is necessary to satisfy all the conditions of equilibrium to get the more accurate result.

Conventional methods of seepage analysis assume that the soil is fully saturated. However, throughout much of the world, slopes exist in residual soil deposits. Such soils are often

unsaturated, and the conventional saturated approach to assessing these slopes is inadequate. In looking at the behaviour of unsaturated soils, some authors (e.g. Dakshanamurthy et al., 1984) incorporate airflow within the soil, and it is clear that this aspect can be significant to the overall behavior of the soil. Touma et al. (1986) have analyzed the effects of soil air flow on the process of water infiltration with variable boundary conditions. The air-phase transport in porous media received considerable interest for many applications and the multi-component multi-phase flow theory being developed quickly (e.g. Van Dijke et al., 1995; Oostrom et al., 1998; Kees et al., 2002; Laroche et al., 2005). Zhang et al. (2009) used a water-air two-phase flow model to simulate the water-air flow of the soil slope under stable situation and water level rise seepage situation and studied the effects of the pore fluid pressure and capillary pressure on slope stability. No attempt has been yet made to analyze the seepage flow of landslide dam by considering air flow within the soil. A numerical model to analyze the influence of air phase in the seepage flow within the landslide dam is also important.

### **1.3.2 Rainfall induced slope failure**

Rainfall induced slope failures are generally caused by increased pore pressures and seepage forces during periods of intense rainfall (Terzaghi, 1950; Sidle and Swanston, 1982; Sitar et al., 1992; Anderson and Sitar, 1995; Wang and Sassa, 2003). The effective stress in the soil will be decreased due to the increased pore pressure and thus reduces the soil shear strength, eventually resulting in slope failure (Brand, 1981; Brenner et al., 1985). In tropical areas, slope failures due to rainfall infiltration are quite usual. These slopes remain stable for a long time before the rainstorms (Brand, 1984; Toll, 2001). During the rainfall, a wetting front goes deeper into the slope, resulting in a gradual increase of the water content and a decrease of the negative pore-water pressure. This negative pore water pressure is referred to as matric suction when referenced to the pore air pressure that contributes towards the stability of unsaturated soil slopes. The loss of suction causes a decrease in shear strength of the soil on the potential failure surface and finally triggers the failure (Rahardjo et al., 1995; Ng and Shi, 1998). Since the rainfall infiltration alters the pore-water pressures only for shallow depths, these rainfall-induced landslides are usually shallow (Au, 1993; Tsaparas, 2002).

Prediction of landslide occurrence is not only for hazard management purpose but also a technique to evaluate how well the process is understood. The most common approach of forewarning of landslide is the recognition of its susceptibility from a spatial perspective

(Crozier, 1995). This generally involves an investigation of geotechnical or geomorphic factors for the purpose of ranking terrain units on their potential to produce landslides. However, Varnes (1984) stated that spatial susceptibility only partly represents the landslide hazard but the greatest challenge is to predict the landslide occurrence time. Landslide prediction methods must be improved by incorporating complicated factors such as subsurface geomorphology, multiphase landslide occurrence, and rainfall characteristics for clarification of landslide mechanisms and mitigation of landslide disasters (Tsutsumi and Fujita, 2008).

It is well known that the major factor influencing on the stability of unsaturated slopes is rainfall event, however there are ongoing debates on the effect of the antecedent rainfall. Based on review on landslides caused by rainfall in Brazil, Wolle and Hachichi (1989) claimed that intense rainfall itself does not influence on slope failure and the antecedent rainfall must be considered in the analysis as it increases the initial moisture of the soil. From 1950 to 1973 Lumb (1975) studied the slope failures in Hong Kong and concluded that the probability of slope failure was due to 15 days of antecedent rainfall. However, Brand (1984) showed that the antecedent rainfall is not a significant factor in slope failures as long as the major rainfall is of a high intensity. The controlling parameters for rainfall-induced landslides are the peak intensity and the 24-hour rainfall. Pitts (1985) also came to a similar conclusion that the antecedent rainfall was not important from his study for Singapore. However, Rahardjo et al. (1998), Toll (2001) and Rahardjo et al. (2001) concluded that antecedent rainfall plays a major role in rainfall induced landslides in Singapore. Toll (2001) believes that minor landslides may occur after significant amounts of antecedent rainfall. Chatterjea (1989) studied the effect of antecedent rainfall on slope failures in Singapore and concluded that a period of 5 days should be enough for analysis of rainfall-induced landslides.

In some cases of rainfall-induced landslides and slope failures, crushing of the soil grains takes place due to the sliding mass movement along the sliding surface, resulting in the liquefaction along this surface, which finally results in rapid movement and long run out distance (Sassa, 1996, 1998a,b). Hence, high pore pressure is a result of shearing along the sliding surface. Liquefaction triggered by static effects e.g., rainfall, snowmelt, etc., or by dynamic effects e.g., earthquakes, has been studied extensively (e.g., Terzaghi, 1956; Seed, 1966, 1979; Bishop, 1967, 1973; Castro, 1969; Casagrande, 1971; Castro and Poulos, 1977; Sassa, 1984, 1996, 1998a,b; Eckersley, 1985, 1986; Hird and Hassona, 1990; Ishihara et al., 1990; Ishihara, 1993).

The assessment of rainfall induced landslide has still been a research topic of wide concern for soil scientists (Tsai et al., 2008). There are two common approaches, empirical rainfall threshold concept and the physically based model. The empirical rainfall threshold concept is very simple but it provides a minimal amount of insight into the actually physical processes. Therefore, for more detail investigation of landslide occurrence, the physically based model needs to be used. The deterministic (e.g., Lumb, 1975; Pradel and Raad, 1993; Ng and Shi, 1998; Gasmol et al., 2000), probabilistic (Suzuki and Matsuo, 1988), and statistical (Okata et al., 1994; Sugiyama et al., 1995; Finlay et al., 1997) analyses have been utilized to connect landslides and slope failures with the rainfall intensity, duration, and antecedent rainfall.

Some hydro-geologists, soil scientists, and geotechnical researchers have been studied the physical process of the infiltration of rainfall into ground and its seepage through the unsaturated saturated soils. Some equations and numerical models have been derived and developed, and they have been comprehensively evaluated by Ng and Shi (1998). Several serious limitations impose restrictions on the use of the equations and models because they do usually not consider sloping ground conditions, down-slope flows, rainfall intensity, and most importantly, the dependence of soil permeability on moisture content. Ng and Shi (1998) and Gasmol et al. (2000) used some numerical analyses to assess the failure mechanism of slopes under rainfall.

To assess shallow landslide induced by land use and hydrological conditions, various physically based models coupling the infinite slope stability analysis with the hydrological modeling were developed assuming steady or quasi steady water table and groundwater flows parallel to hill slope (Montgomery and Dietrich, 1994; Wu and Sidle, 1995; Borga et al., 1998). With approximation of Richards' equation (1931) valid for hydrological modeling in nearly saturated soil, Iverson (2000) further developed a flexible modeling framework of shallow landslide. Baum et al. (2002) proposed an extension version of Iverson's model to consider variable rainfall intensity into account for hill slope with finite depth. Tsai and Yang (2006) modified Iverson's model by amending the boundary condition at the top of the hill slope to consider more general infiltration process instead of constant infiltration capacity. The physically based model with the hydrological modeling in nearly saturated soil (Iverson, 2000; Baum et al., 2002; Tsai and Ynag, 2006) was commonly used for the assessment of shallow landslides triggered by rainfall due to its simplicity (Crosta and Frattini, 2003; Keim and Skaugset, 2003; Frattini et al.,

2004; Lan et al., 2005; D'Odorico et al., 2005; Tsai, 2007). Tsai et al. (2008) developed a physically based model not only by using the complete Richards' equation with the effect of slope angle, but also by adopting the extended Mohr-Coulomb failure criterion (Fredlund et al., 1978) to describe the unsaturated shear strength.

Sassa (1972, 1974) carried out a series of flume tests and concluded that the changes in rigidity of sand and upper yield strain within a slope are essential to the analysis of slope stability. Fukuzono (1987) conducted experiment to examine the conditions leading up to slope failure using nearly actual scale slope models providing heavy rainfall. Crozier (1999) tested a rainfall-based landslide-triggering model developed from previous landslide episodes in Wellington City, New Zealand, which referred to as the Antecedent Water Status Model, to provide a potentially useful level of prediction of landslide occurrence by providing a 24 hour forecast. Sharma (2006) carried out experimental and numerical studies to investigate effects of slope angle on the moisture movement on unsaturated soil and further on the slope stability, and also analyzed the difference in failure pattern and moisture movement in single and two layers of soil with different hydraulic conductivities. Tsustumi and Fujita (2008) investigated several landslide sites and used physical experiment and numerical simulation with the combination of rainwater infiltration for the analysis of slope stability. Mukhlisin and Taha (2009) developed numerical model to estimate the extent of rainwater infiltration into an unsaturated slope, the formation of a saturated zone, and the change in slope stability. Then, the model was used to analyze the effects of soil thickness on the occurrence of slope failure.

The above discussed numerical studies are applicable only for two dimensional analyses; however failure of slopes occurs in three dimensions. There is not only water phase but also air phase in soil slopes. Both the pore air and water will have influence on the seepage flow, but all the above mentioned studies have neglected the air flow on seepage analysis. Therefore, numerical study in three dimensions is necessary for seepage analysis and slope stability analysis with considering the effects of air phase in the seepage.

## **1.4 Outlines of the dissertation**

This research concerns the development of numerical models for the evaluation of critical failure surface of a slope due to a rainfall event and sudden sliding failure of landslide dam.

Chapter 1 presents backgrounds of the work, objectives of the study and a brief review of previous literatures.

Chapter 2 presents the experimental studies in laboratory and also describes the basic principle and methods of measurement of some of the major apparatus used are described.

Chapter 3 presents three dimensional seepage flow and slope stability analysis models with two dimensional surface water flow model combined with erosion/deposition model for the prediction of critical failure surface of a slope due to a rainfall event. The proposed models are verified with different experimental results.

Chapter 4 presents two and three dimensional seepage flow and slope stability analysis models for the prediction of critical failure surface of a landslide dam. The proposed models are verified with different experimental results.

Chapter 5 summarises the conclusions based on the present study and recommendations for the future researches.



## **Chapter 2**

### **Experimental Studies on Slope failure**

#### **2.1 Introduction**

Using the information obtained from the natural slopes it is difficult to explain slope failure mechanisms because it is impossible to know the exact failure site, the time of failure, and soil conditions at failure. Experiments using slope models with simple conditions are one useful approach to study the process of slope failure (Fukuzono, 1987). In order to investigate the failure mechanism, many researchers carried out experimental studies in their field of interests.

Fukuzono (1987) conducted experiment to investigate the conditions leading up to slope failure using nearly actual-scale slope models providing heavy rainfall. Moriwaki (2004) carried out a full-scale landslide experiment to clarify the failure process of a landslide triggered by rainfall. Tohari (2007) observed failure initiation process failure modes, and changes in soil moisture content during failure initiation conducting series of rainfall experiments on rainfall-induced slope failures.

In this study, a sandy soil model slope was prepared inside a rectangular sloped flume so as to measure moisture profiles, air pressure head profiles, surface water forefront propagation, downstream seepage out flow and 3D failure surface within the body of the model slope. This section also describes the basic principle and methods of measurement of some of the major apparatus used in the experiment.

#### **2.2 Experimental set-up and measurement apparatus**

##### **2.2.1 Laboratory flume**

A 3m long, 80cm wide and 70cm deep rectangular flume, with adjustable longitudinal slope was used for the experiment. The flume sidewalls were made of aquarium glass. For capturing the initiation of slope failure process and movement of the failure mass, three digital video cameras (VCs) were used. Two cameras were placed in the sides and one was placed in the front of the

flume. The experiments were carried out on  $23^\circ$  and  $28^\circ$  flume slope. The schematic diagram of the flume, including instrumentation and data acquisition system is shown in Figure 2.1.

It is difficult to observe the three dimensional view of the failure surface in rectangular flume shape. So, the rectangular shape of the flume was modified using 292.5 cm long and 3cm thick wooden plates for making V-shape having cross slope of  $20^\circ$ . The model slope was prepared on the rigid bed of flume by placing silica sand S6. A small space was allowed in the upstream for providing runoff input so as to develop water table in the bottom layer of the model slope which is essential for slope failure phenomenon. The downstream end of the flume was closed with a filter mat supported by a wooden plate for retaining the soil and providing downstream free flow condition. The downstream seepage out flow was collected in a measuring cylinder through a metal container. Profile probes (PRs) consisting four sensors (SRs) were used to measure the temporal variation of moisture content and pressure transducers (PTs) were used to measure the temporal variation of air pressure at different locations inside the body of the model slope. Red colored sediment strips and red colored cotton threads were placed respectively at the side wall faces and inside the body, normal to the flume bed, so as to measure the failure surface after sliding. Scales for measuring surface water forefront propagation were placed in vertical position on the top surface of the model slope in its central longitudinal section (Figures 2.9, 2.10 and 2.11).

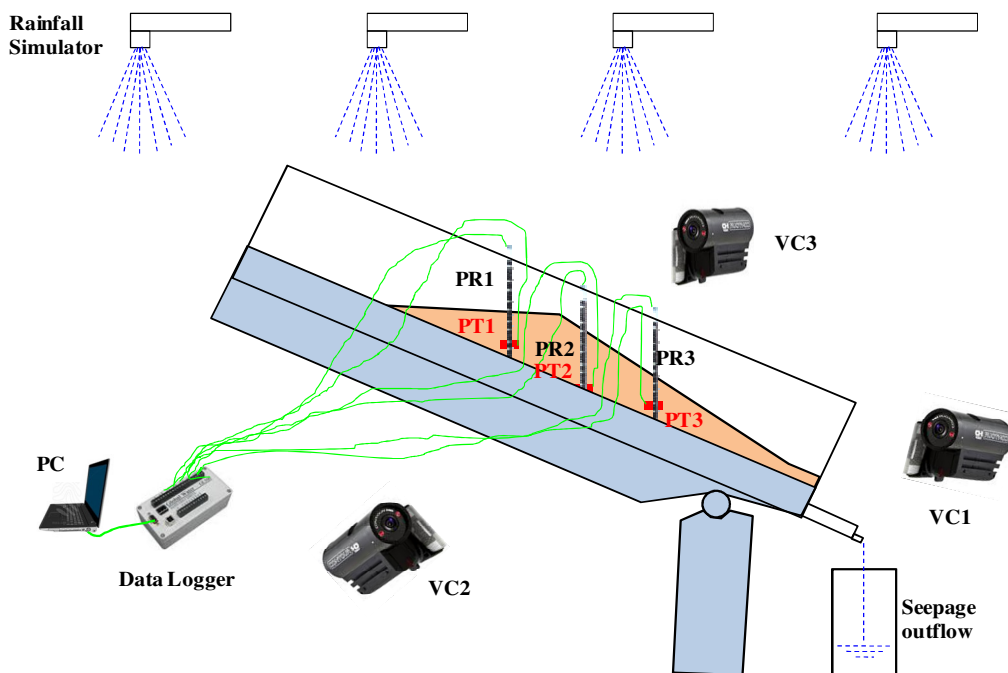


Figure 2.1 Experimental setup

## 2.2.2 Multi-fold pF meter

DIK-3423 Multi-Fold pF Meter (Figure 2.2) was used for measuring the moisture retention curve of a soil sample. It can set up to 24 pieces of sampling tubes in the sample chamber. Any optional pF value can be set with the automatic pressure controller. This controller can set an accurate and stable pressure without taking the influence of atmospheric pressure. A specified pressure is applied to a soil sample and the weight of the soil at equilibrium is measured to determine the volumetric water content corresponding to the matrix potential; this procedure is repeated at various pressures to construct a moisture retention curve for the soil sample. For each magnitude of the air pressure applied, the moisture content of the soil sample is determined by calculating the difference between the weight of the measured soil sample and that of the same soil sample in a dry state. The determined moisture content corresponds to the applied air pressure, hence, the moisture potential at the time of measurement, thus providing a moisture content corresponding to a given pF value.

The sediment used in the study was silica sand. Figure 2.3 shows  $\theta_w - h_w$  relationship curve for the sediment. The grain size distribution of the sediment is shown in Figure 2.4. van Genuchten parameters (including  $\theta_r$ ) were estimated by non-linear regression analysis of soil moisture retention data obtained by pF meter experiments for the considered sediment which is presented in Table 2.1.



DIK-3421-11 Sample chamber



DIK-9221 Automatic pressure

Figure 2.2 Multi-fold pF meter (Source: Daiki Rika Kogyo Co., Ltd.)

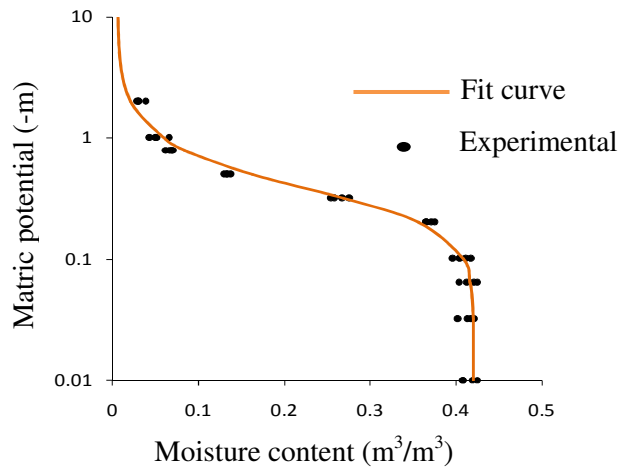


Figure 2.3  $\theta_w-h_w$  relationship curve for silica sand S6

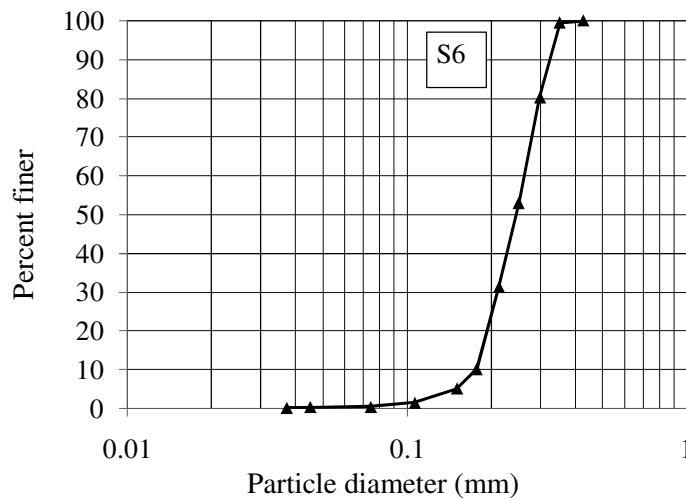


Figure 2.4 Grain size distribution of the sediment

Table 2.1 Some parameter values of the sediment considered

Sediment type	S6
Saturated moisture content, $\theta_s$	0.42
Residual moisture content, $\theta_r$	0.004
van Genuchten parameter, $\alpha$	3.227
van Genuchten parameter, $\eta$	2.7
Saturated hydraulic conductivity, $K_s$ (cm/sec)	0.02153
Specific gravity, $G_s$	2.63
Mean grain size, $D_{50}$ (mm)	0.24
Angle of repose, $\phi$	$34^\circ$
Porosity, $n$	0.42
Compression index, CI	1.08

### 2.2.3 Profile probe

The Profile Probe (PR) measures soil moisture content at different depths within the soil profile. It consists of a 25mm diameter sealed polycarbonate rod with electronic sensors (seen as pairs of stainless steel rings) arranged at fixed intervals along its length. The profile probe type PR2 (Figure 2.5) consist of four sensors in 10cm spacing. When taking a reading, the probe is inserted into an access tube. The access tubes are specially constructed thin-wall tubes, which maximize the penetration of the electromagnetic field into the surrounding soil. The output from each sensor is a simple analogue dc voltage (out-put 0.0~1.0 V). These outputs are easily converted into soil moisture using the supplied general soil calibrations or the probe can be calibrated for specific soils. It works within the accuracy of  $\pm 4\%$  and can be installed easily with minimal soil disturbance. Figure 2.6 shows a typical calibration curve for a specific soil of a calibrated probe.

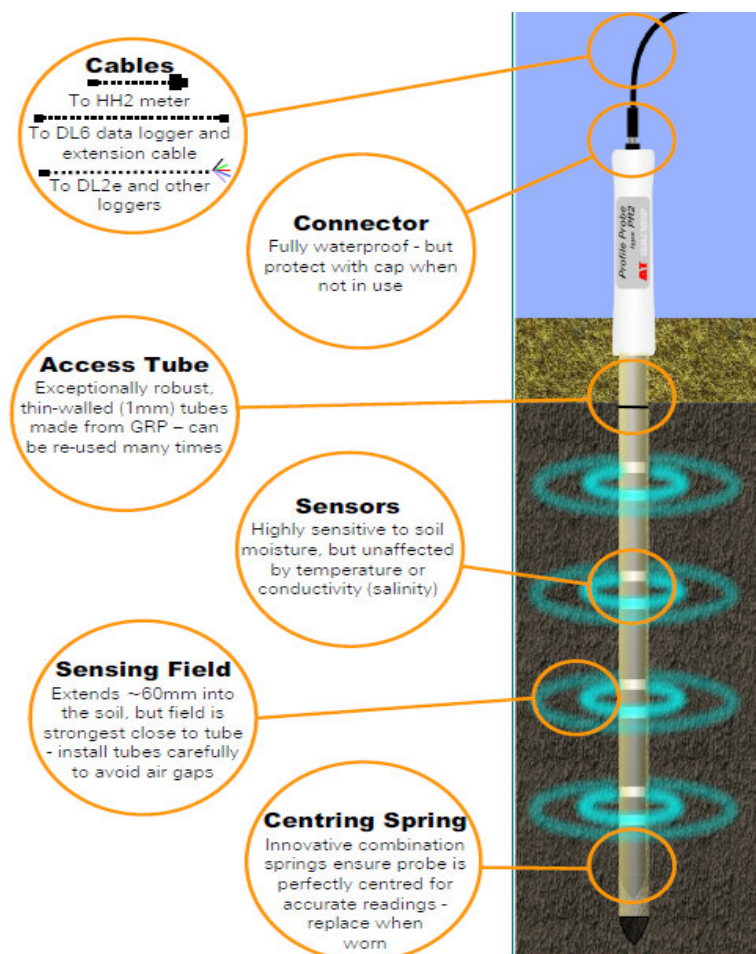


Figure 2.5 Profile probe type PR2 (Source: Delta-T Devices Ltd., 2004a)

Each probe can be used both for portable readings from many access tubes and for installation within one access tube for long-term monitoring. When power is applied to the Profile Probe, it creates a 100MHz signal similar to FM radio. The signal is applied to pairs of stainless steel rings which transmit an electromagnetic field extending about 600mm into the soil. The field passes easily through the access tube walls, but less easily through any air gaps. It has been designed to make its use with data loggers straightforward. It is particularly simple to use with the DL6 data logger as they have been designed to work together.

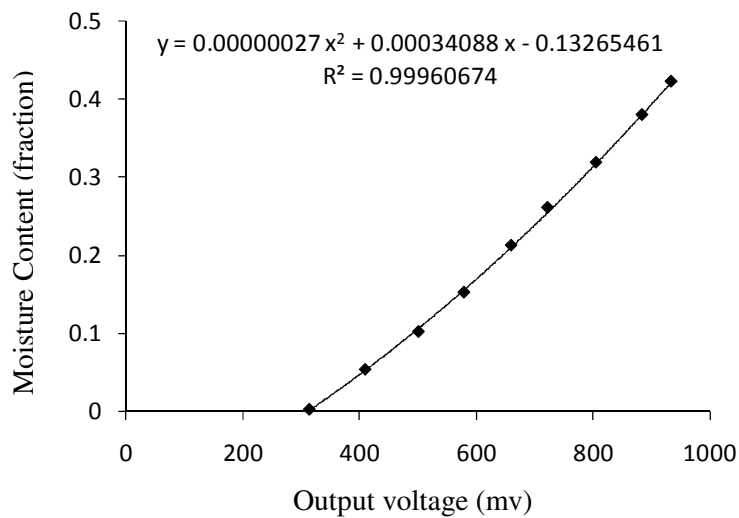


Figure 2.6 Typical calibration curve for a sensor of profile probe PR2

## 2.2.4 Pressure transducer



Figure 2.7 Pressure transducers

The pressure transducer (PT) with amplifier PA-850-102R-NGF (Figure 2.7), Copal electronics product, was used in the experiment to measure air pressure profile inside the model slope. It has high corrosion resistance and drip-proof construction having pressure port attachment made of SUS 316L (Copal Electronics, 2007). It provides both a switch output (hysteresis adjustable)

and an analog output. It measures the pressure exerted by the fluid which is in contact with its stainless steel diaphragm. The available pressure measurements are absolute (0~100 kpa) and compound (-100~100 kpa).

### 2.2.5 Point gauge

The point gauge (Figure 2.8);capable to measure the location of air-water surface boundaries, slowly changing water levels in flumes and hydraulic models and mechanical deformation; was used to measure the location of failure surface after the failure of model slope during laboratory experiment.

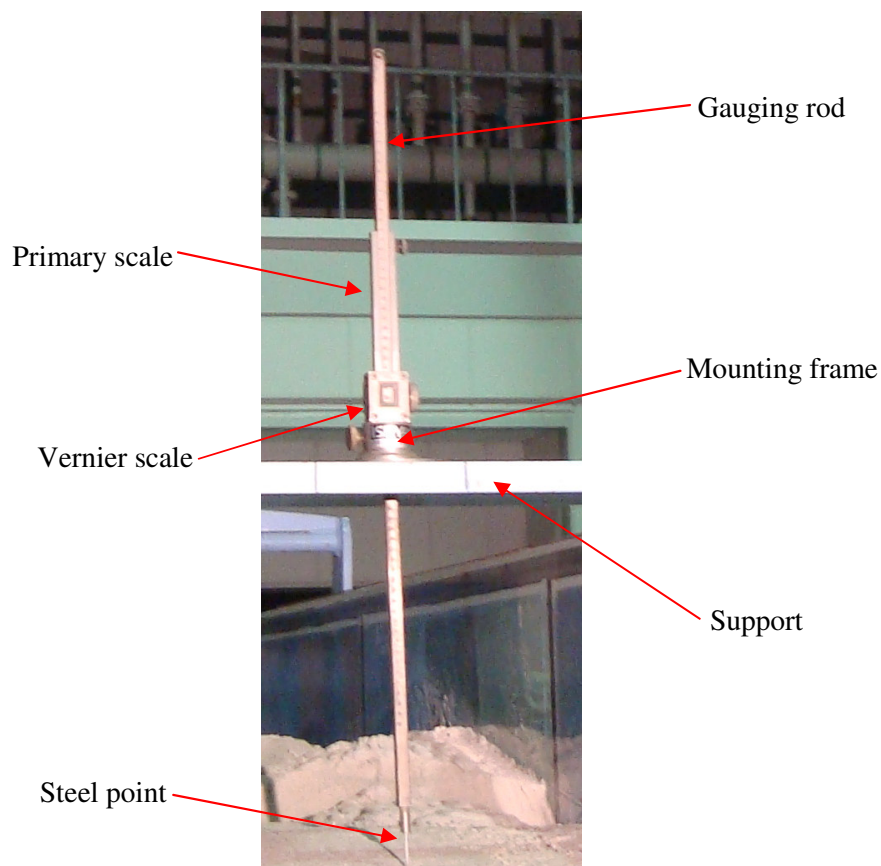


Figure 2.8 Point gauge

A mounting frame is clamped to a suitable support structure and a gauging rod is free to slide up and down. A stainless steel point is attached to the bottom end of the rod and is used to locate the failure surface. Gauging carried out by means of a primary scale attached to the mounting frame and a vernier scale attached to the rod. The scales are in edge contact. The rod is held in a

screwed collar for fine adjustment and can be released for large, rapid changes of position. Zero can be reset by a locking screw positioned on the vernier scale. It works within the accuracy of  $\pm 0.1\text{mm}$ .

### 2.3 Test Procedures

The model slope was prepared by placing sediment on the flume and compacted in every 5cm thickness (approximately) using timber plate. The flume was in inclined position during preparation for moisture profile and air pressure head profile measurements, whereas it was in horizontal position during preparation for observing the slope failure process and movement of the failure mass. The profile probes (PRs) and air pressure transducers (PTs) are positioned in their proper location during the preparation of the model slope. Shape and size of the model slope with the arrangement of PRs sensors (SRs), PTs and scales for measuring surface water forefront propagation are schematically shown in Figures 2.9 and 2.10.

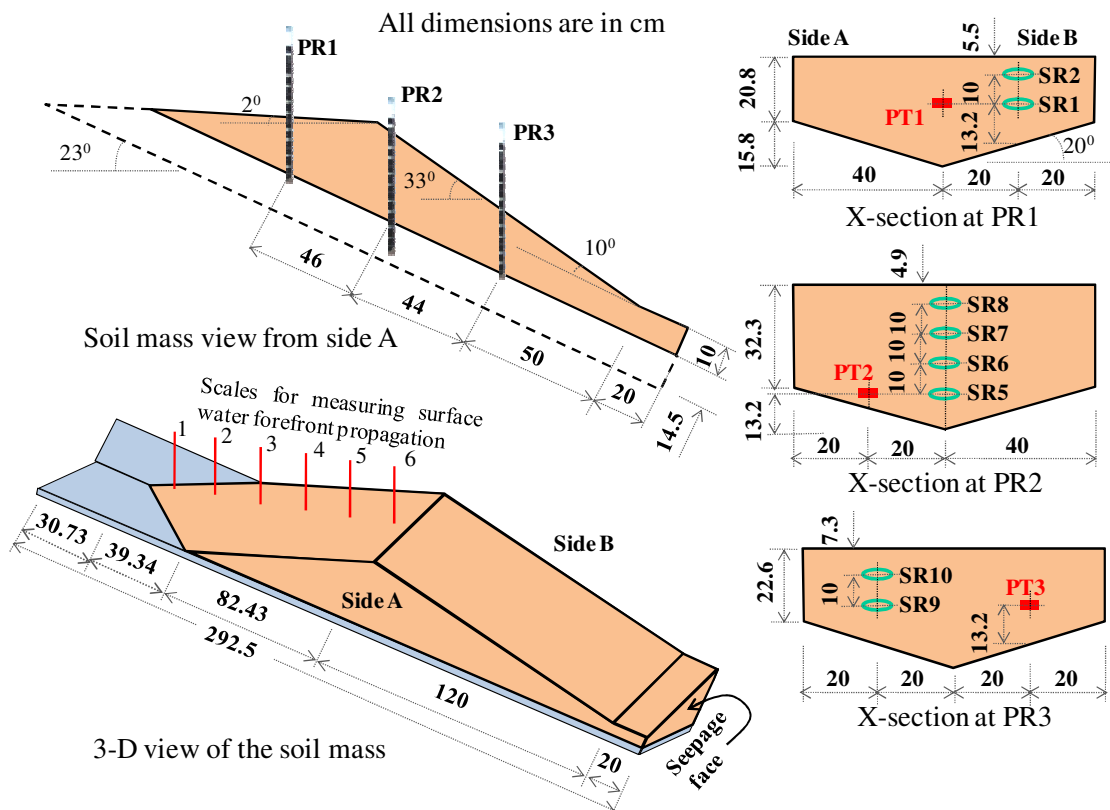


Figure 2.9 Model slope with the arrangement of SRs, PTs and surface water forefront measurement scales (Flume slope  $23^\circ$ )

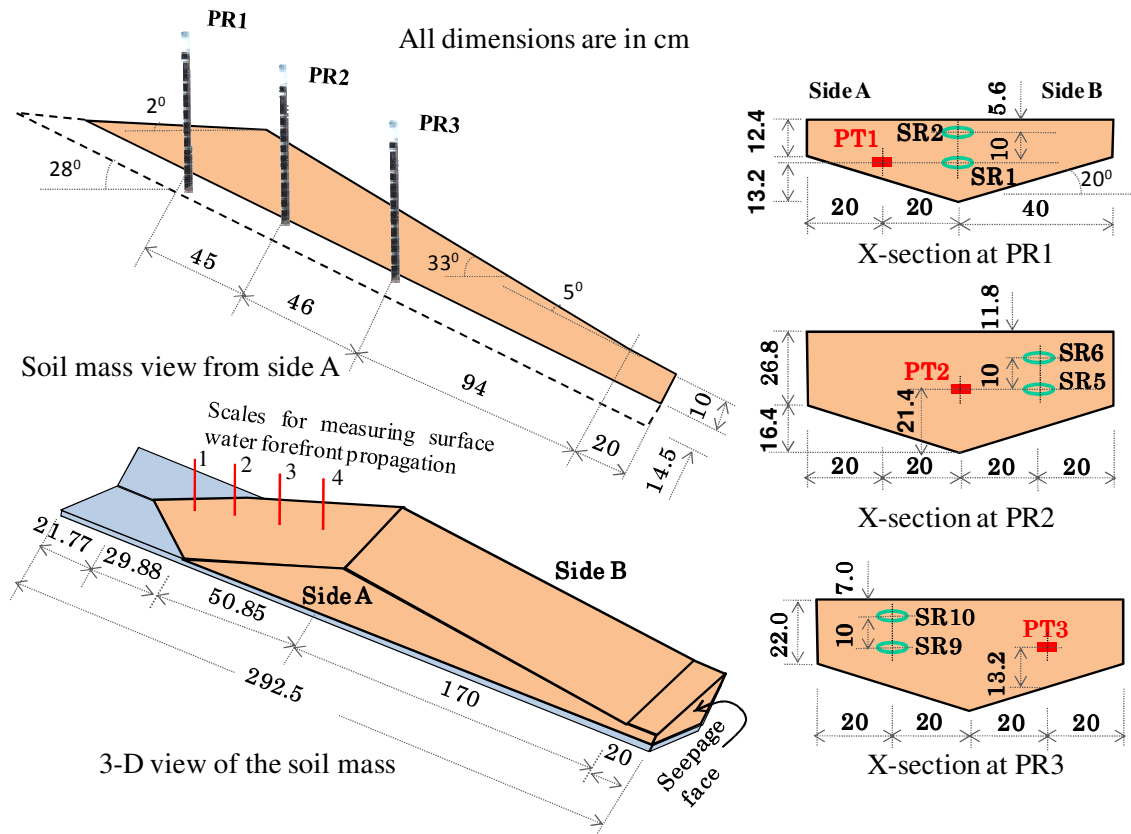


Figure 2.10 Model slope with the arrangement of SRs, PTs and surface water forefront measurement scales (Flume slope 28°)

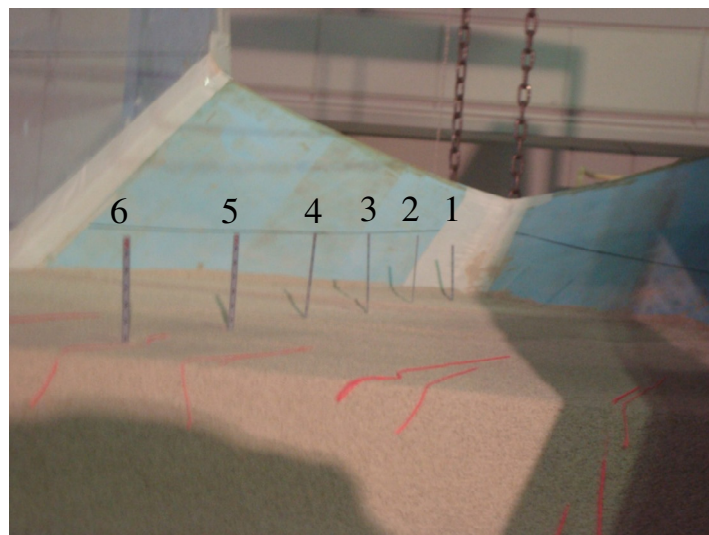


Figure 2.11 Picture showing the position of measuring scales for surface water forefront propagation (23° flume slope)

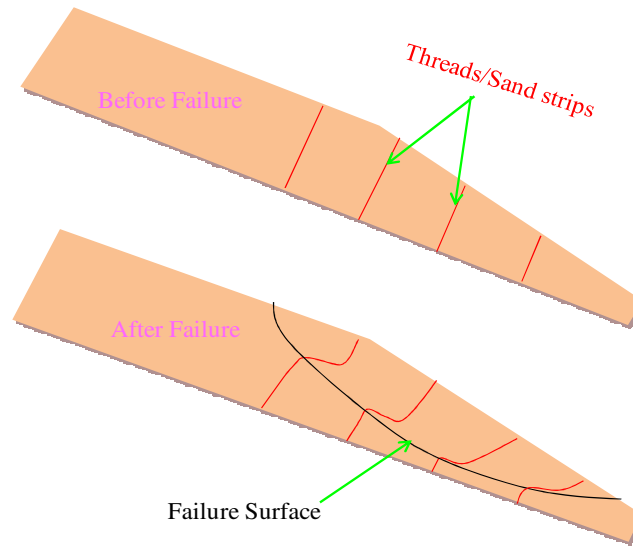


Figure 2.12 Typical sketches showing the alignment of threads/sand strips before and after the failure of slope in a particular L-section

Figure 2.11 presents the picture that shows the position of measuring scales for surface water forefront propagation incase of  $23^\circ$  flume slope. Distance of surface water forefront propagation measuring scales from downstream face is presented in Table 2.2. To measure the movement of slope mass, red colored sediment strips and cotton threads were used. Sediment strips were placed at the face of the flume and threads were attached firmly in the bottom wall before preparation of the dam body. Figure 2.12 presents the typical sketches showing alignment of sand strips/threads before and after the failure of slope in a particular L-section.

## 2.4 Results and discussions

The experiments were carried out by preparing a sandy soil model slope at  $23^\circ$  and  $28^\circ$  flume slope so as to measure moisture profiles, air pressure head profiles, surface water forefront propagation, downstream seepage out flow and three dimensional failure surface within the body of the model slope. Average rainfall over the flume during experiment was 105.03mm/hr. In the experiment, the artificial rainfall provided by the simulators was not uniform. Also the measured rainfall values at same location were different in different measurements. Such kind of unreliability in rainfall intensity was due to the power fluctuation in the water pump, losses in water supply pipes, temperature variation, etc. Five experiments were conducted for measuring

rainfall intensity for the same supply condition of water in different seasons throughout a year and average value of these measurements was assumed as the supply rainfall in the experiments and simulations. Figure 2.13 presents a contour map showing rainfall distribution over the flume. Figures 2.14 and 2.15 present the experimental water content profiles at different sensors (SRs). In each sensor, moisture increase rate due to the wetting front contributed only by the rainfall intensity above it is comparatively slow before reaching the sharp wetting front through later inflow from upstream surface runoff. In case of sensors 1 and 5 (Figure 2.14) and sensor 1

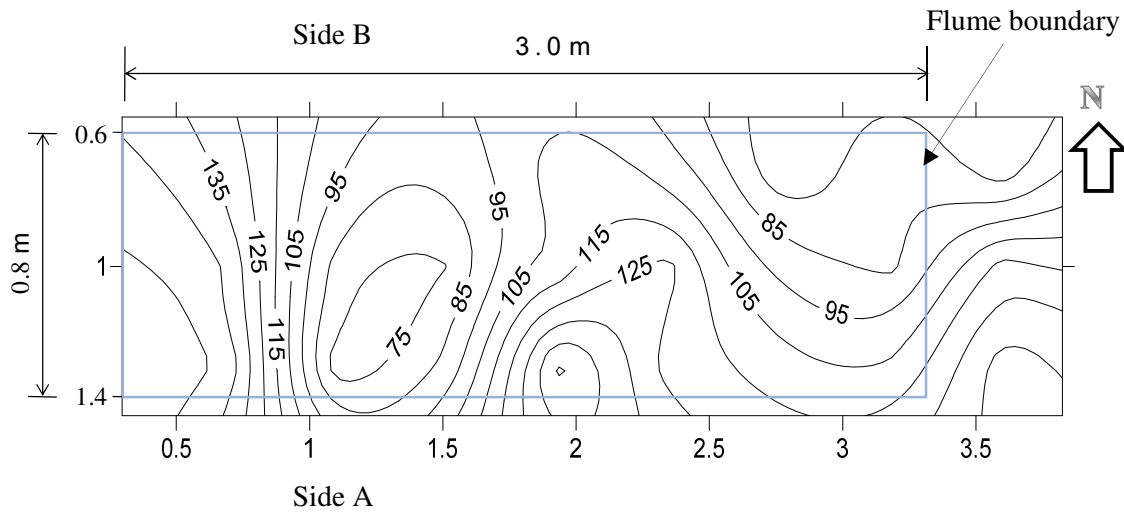


Figure 2.13 Distribution of rainfall intensity (in mm/hr) over the flume

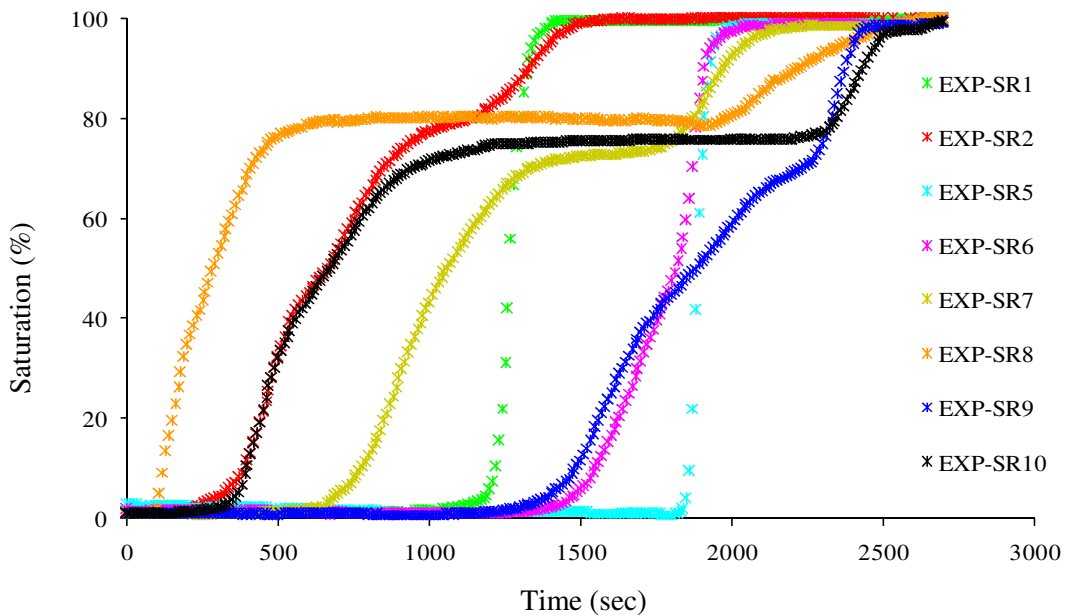


Figure 2.14 Water content profiles observed in experiment (23° flume slope)

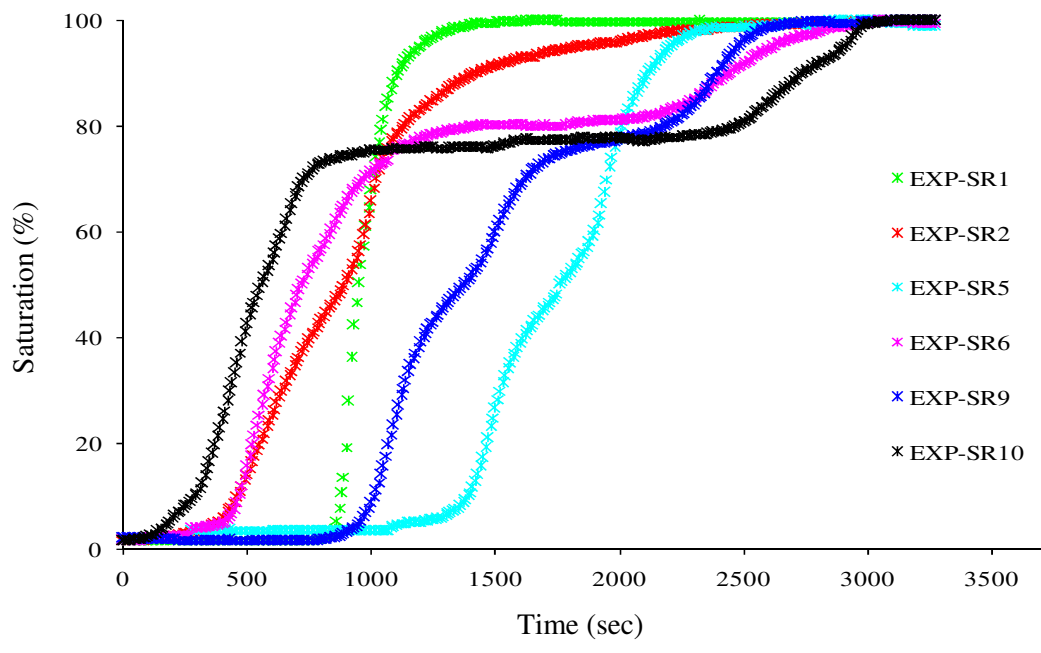


Figure 2.15 Water content profiles observed in experiment (28° flume slope)

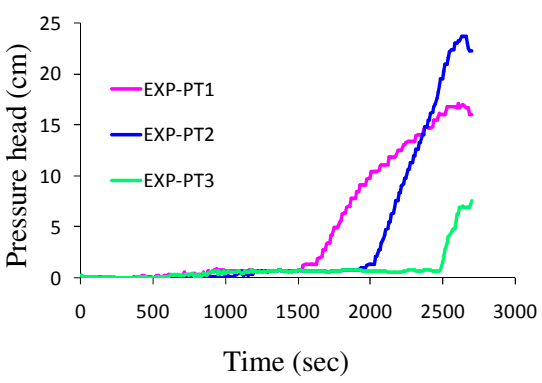


Figure 2.16 Air pressure head profiles observed in experiment (23° flume slope)

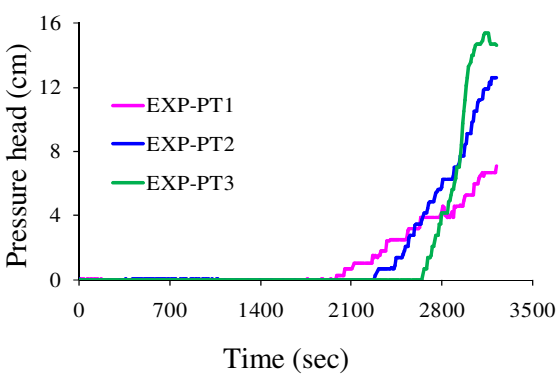


Figure 2.17 Air pressure head profiles observed in experiment (28° flume slope)

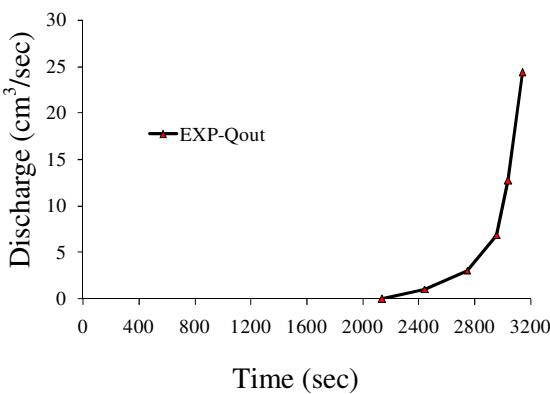


Figure 2.18 Seepage Outflow observed in experiment (23° flume slope)

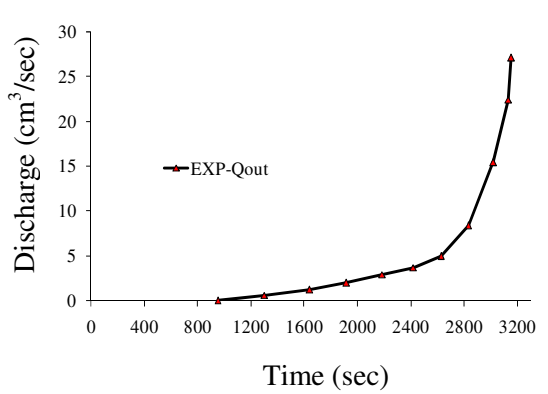


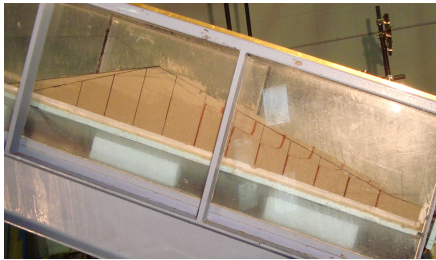
Figure 2.19 Seepage outflow observed in experiment (28° flume slope)

(Figure 2.15), sharp wetting front through lateral inflow reached prior to the wetting front through rainfall intensity above it so that sudden raise of moisture from its initial value was observed. Figures 2.16 and 2.17 present the experimental air pressure head profiles at different pressure transducers (PTs). Table 2.2 presents the time at which the surface water forefront

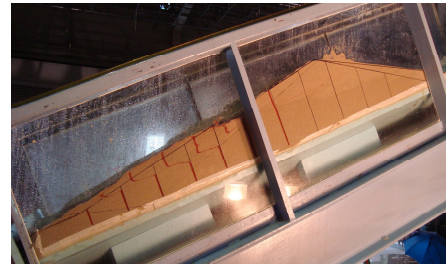
Table 2.2 Surface water forefront propagated time to measuring scales

23° flume slope			28° flume slope		
Scale	Distance Parallel to flume slope (m)	Water forefront reached time (sec)	Scale	Distance Parallel to flume slope (m)	Water forefront reached time (sec)
1	2.5	35	1	2.6	102
2	2.3	77	2	2.45	497
3	2.1	276	3	2.3	2153
4	1.9	761	4	2.15	3184
5	1.7	1369			
6	1.5	1983			

Side A view



Side B view

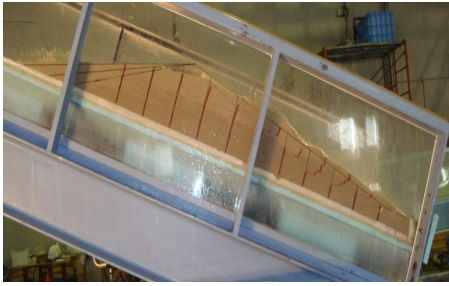


Front view



Figure 2.20 Observed slope sliding (23° flume slope - Experiment D)

Side A view



Side B view



Front view



Figure 2.21 Observed slope sliding ( $23^\circ$  flume slope - Experiment E)

Side A view



Side B view



Front view

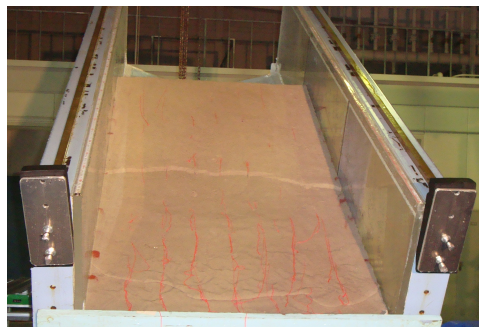


Figure 2.22 Observed slope sliding ( $28^\circ$  flume slope)

propagated to the measuring scales in experiments.

Experimentally observed seepage outflow from downstream seepage face was shown in Figures 2.18 and 2.19. Figures 2.20, 2.21 and 2.22 show the observed sliding of slope in different experiments. Since the trend of observed rainfall intensity was larger towards side A than B (Figure 2.13), the concentration of observed sliding slope was also towards side A rather than B (Figures 2.20, 2.21 and 2.22). Figure 2.23 presents the alignment of failure plane in a particular L-section within the body of a model slope.

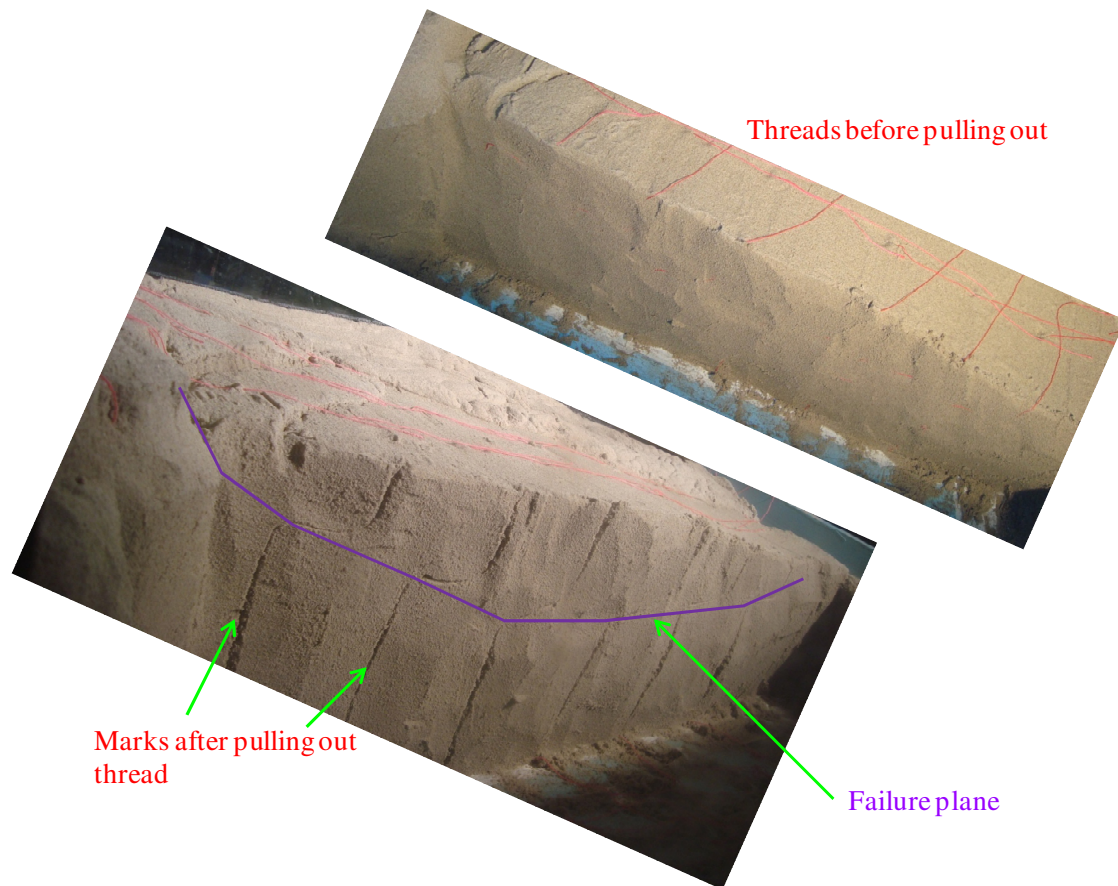


Figure 2.23 Alignment of failure plane in a particular L-section within the body of a model slope

## **Summary**

Experimental study was carried out by preparing a sandy soil model slope inside a rectangular sloped flume so as to measure moisture profiles, air pressure head profiles, surface water forefront propagation, downstream seepage out flow and three dimensional failure surface within the body of the model slope. The flume slope was set up at angles  $23^\circ$  and  $28^\circ$ . Profile probes consisting four sensors were used to measure the temporal variation of moisture content and pressure transducers were used to measure the temporal variation of air pressure at different locations inside the body of the model slope. Measuring scales were placed in vertical position on the top surface of the model slope in its central longitudinal section for measuring the surface water forefront propagation. Downstream seepage outflow was measured by collecting outflow seepage water in a measuring cylinder. Digital video cameras were used for capturing the surface water forefront propagation, initiation of slope failure process and movement of the failure mass.

## **Chapter 3**

### **Analysis of Rainfall Induced Slope Failure**

#### **3.1 Introduction**

Slope failures in residual soils are common in many tropical countries particularly during periods of intense rainfall. The location of the groundwater table in these slopes may be in deep below the ground surface and the pore-water pressures in the soil above the groundwater table are negative to atmospheric conditions. This negative pore-water pressure, referred to as matric suction when referenced to the pore-air pressure that contributes towards the stability of unsaturated soil slopes (Fredlund and Rahardjo, 1993; Rahardjo et al., 1995; Griffiths and Lu, 2005). Under the influence of rainfall infiltration, water seepage can cause a gradual loss of matric suction in an unsaturated soil slope. As the hydraulic properties of the soil with respect to matric suction are often highly nonlinear, rapid changes in pore-water pressure have a significant effect on the soil strength, and therefore on the stability of the slope.

Modeling rainwater infiltration in slopes is vital to the analysis of slope failure induced by heavy rainfall. The stability coefficient of the soil slope will decrease under the action of seepage force due to rainwater infiltration. In unsaturated soil slope there is not only water phase but also air phase so that both the pore water and pore air will have the influence on seepage flow. Most of the previous studies have considered only the water flow but neglected air flow. However, to fully and accurately model unsaturated soil, both the water and air phases should be treated separately, with pressure and flow of both the phases tacked within the model.

Numerical models have been used previously by Gasmol et al. (2000), Cho and Lee (2001), Tsaparas et al. (2002), and Wilkinson et al. (2002) to study the effect on slope stability of rainwater infiltration into unsaturated soils. In this study, analysis of slope failure due to a rainfall event was carried out in 3D. The stability of the considered slope was investigated using pore water pressure and moisture content calculated by only a conventional water-phase seepage flow model as well as the water-air two-phase seepage flow model. Janbu's simplified method as well as extended Spencer method was incorporated into dynamic programming to locate the

critical slip surface of a general slope. Simulation results were compared with the experimental results obtained so as to evaluate the capability of the model.

## 3.2 Seepage flow analysis

Rainfall intensity and the surface water head of the runoff produced by the provided artificial rainfall through the rainfall simulator above the flume was the input for the seepage flow inside the model slope. Seepage flow analysis was carried out using only a conventional water-phase seepage flow model as well as the water-air two-phase seepage flow model coupled with surface flow and erosion/deposition model. Surface flow and erosion/deposition model was used to compute the surface water head of the runoff produced by the rainfall and erosion and deposition depths on the surface.

### 3.2.1 Seepage flow model

#### Governing equations

Following pressure based Richards' equation valid for variably saturated soil was used in conventional 3D seepage flow model for calculating the change in pore water pressure inside the model slope (Awal et al., 2009).

$$\left( C + S_w S_s \right) \frac{\partial h_w}{\partial t} = \frac{\partial}{\partial x} \left( K_x \frac{\partial h_w}{\partial x} \right) + \frac{\partial}{\partial y} \left( K_y \frac{\partial h_w}{\partial y} \right) + \frac{\partial}{\partial z} \left( K_z \left( \frac{\partial h_w}{\partial z} + 1 \right) \right) \quad (3.1)$$

where,  $h_w$  is the water pressure head;  $K_x$ ,  $K_y$  and  $K_z$  are the hydraulic conductivity in  $x$ ,  $y$  and  $z$  direction respectively;  $C = \partial \theta_w / \partial h_w$  is the specific moisture capacity,  $\theta_w$  is the soil volumetric water content;  $S_w$  is the saturation ratio  $= \theta_w / n$ ;  $S_s$  is the specific storage;  $t$  is the time;  $x$  and  $y$  are the horizontal spatial coordinates; and  $z$  is the vertical spatial coordinate taken as positive upwards.  $S_s$  depends on compressibility of solid matrix and fluid, so it approaches zero in the unsaturated and unconfined porous medium.

In order to solve the equation (3.1) following constitutive relationships proposed by van Genuchten (1980) are used for establishing relationship of moisture content and water pressure head ( $\theta_w-h$ ), and unsaturated hydraulic conductivity and moisture content ( $K-\theta_w$ ):

$$S_e = [1 + (\alpha h_w)^n]^{-m} \quad (3.2)$$

$$S_e = \frac{\theta_w - \theta_r}{\theta_s - \theta_r} \quad (3.3)$$

$$C = \frac{(n - \theta_r) \eta m \alpha |\alpha h_w|^{\eta-1}}{\left(1 + |\alpha h_w|^\eta\right)^{m+1}} \quad (3.4)$$

$$K = K_s S_e^{0.5} [1 - (1 - S_e^{1/m})^m]^2 \quad (3.5)$$

where,  $S_e$  is the effective saturation;  $\alpha$  and  $\eta$  are empirical parameters;  $\theta_s$  and  $\theta_r$  are saturated and residual moisture content respectively;  $n$  is the porosity of soil;  $K_s$  is the saturated hydraulic conductivity; and  $m=1-1/\eta$ .

For 3D water-air two-phase seepage flow analysis, following equations are derived for the simultaneous flow of water and air based on the 1D flow equations derived by Touma, and Vauclin (1986), in which hysteresis and dynamic effects as well as air diffusion into the water are neglected.

Water-phase equation

$$C \left( \frac{\partial h_a}{\partial t} - \frac{\partial h_w}{\partial t} \right) = \frac{\partial}{\partial x} \left( K_{wx} \frac{\partial h_w}{\partial x} \right) + \frac{\partial}{\partial y} \left( K_{wy} \frac{\partial h_w}{\partial y} \right) + \frac{\partial}{\partial z} \left( K_{wz} \left( \frac{\partial h_w}{\partial z} + 1 \right) \right) \quad (3.6)$$

Air-phase equation

$$\left( (n - \theta_w) \frac{\rho_{oa}}{h_o} - \rho_a C \right) \frac{\partial h_a}{\partial t} + \rho_a C \frac{\partial h_w}{\partial t} = \frac{\partial}{\partial x} \left( \rho_a K_{ax} \frac{\partial h_a}{\partial x} \right) + \frac{\partial}{\partial y} \left( \rho_a K_{ay} \frac{\partial h_a}{\partial y} \right) + \frac{\partial}{\partial z} \left( \rho_a K_{az} \left( \frac{\partial h_a}{\partial z} + \frac{\rho_a}{\rho_{ow}} \right) \right) \quad (3.7)$$

where,  $h_a$  is the air pressure head;  $h_o$  is the atmospheric pressure expressed in terms of water column height;  $C = \partial\theta/\partial h_c$  is capillary capacity;  $h_c = h_a - h_w$  is capillary head;  $\rho_a$  is density of air;  $\rho_{oa}$  is density of air at the atmospheric pressure;  $\rho_{ow}$  is density of water at the atmospheric pressure;  $K_{wx}$ ,  $K_{wy}$  and  $K_{wz}$  are the hydraulic conductivity in  $x$ ,  $y$  and  $z$  directions respectively; and  $K_{ax}$ ,  $K_{ay}$  and  $K_{az}$  are the air conductivity in  $x$ ,  $y$  and  $z$  directions respectively.

In order to solve the equations (3.6) and (3.7) following constitutive relationships are used.

van Genuchten (1980) proposes following relationships:

$$S_e = [1 + (\alpha h_c)^\eta]^{-m} \quad (3.8)$$

$$S_e = \frac{\theta_w - \theta_r}{\theta_s - \theta_r} \quad (3.9)$$

$$C = -\frac{(n-\theta_r) \eta m \alpha (\alpha h_c)^\eta}{(1+(\alpha h_c)^\eta)^{m+1}} \quad (3.10)$$

Chen et al. (1989) used following relationships as VGM (van Genuchten and Mualem) model:

$$K_w = K_{ws} S_e^{0.5} [1 - (1 - S_e^{1/m})^m]^2 \quad (3.11)$$

$$K_a = K_{as} (1 - S_e)^{0.5} [1 - S_e^{1/m}]^{2m} \quad (3.12)$$

where,  $K_{ws}$  is the saturated hydraulic conductivity;  $K_{as}=K_{ws} (\mu_w/\mu_a)$  is the saturated air conductivity; and  $\mu_w$  and  $\mu_a$  are dynamic viscosity of water and air respectively.  $\mu_w = 1.002 \times 10^{-2}$   $NS/m^2$  and  $\mu_a = 1.83 \times 10^{-5}$   $NS/m^2$  at 20°C.

## Solution approach

Numbers of methods are available for the numerical solution. In several 1D variably saturated flow studies, finite difference schemes have been widely used (e.g. Day and Luthin, 1956; Freeze, 1969; Kirkby, 1978; Dam and Feddes 2000; Vasconcellos and Amorim, 2001). However, fewer researchers have used finite differences to solve variably saturated flow problems in higher dimensions. In this study, the equations 3.1, 3.6 and 3.7 are solved by line successive over relaxation (LSOR) scheme used by Freeze (1971a, 1971b, 1978) by an implicit iterative finite difference scheme.

The finite difference form of Equation 3.1 is as follows:

$$\begin{aligned} C \left( \frac{h_{w\ i,j,k}^t - h_{w\ i,j,k}^{t-1}}{\Delta t} \right) = & \\ \frac{1}{\Delta x} \left[ K1 \left( \frac{h_{w\ i+1,j,k}^t + h_{w\ i+1,j,k}^{t-1} - h_{w\ i,j,k}^t - h_{w\ i,j,k}^{t-1}}{2\Delta x} \right) - K2 \left( \frac{h_{w\ i,j,k}^t + h_{w\ i,j,k}^{t-1} - h_{w\ i-1,j,k}^t - h_{w\ i-1,j,k}^{t-1}}{2\Delta x} \right) \right] + & \\ \frac{1}{\Delta y} \left[ K3 \left( \frac{h_{w\ i,j+1,k}^t + h_{w\ i,j+1,k}^{t-1} - h_{w\ i,j,k}^t - h_{w\ i,j,k}^{t-1}}{2\Delta y} \right) - K4 \left( \frac{h_{w\ i,j,k}^t + h_{w\ i,j,k}^{t-1} - h_{w\ i,j-1,k}^t - h_{w\ i,j-1,k}^{t-1}}{2\Delta y} \right) \right] + & \\ \frac{1}{\Delta z} \left[ K5 \left( \frac{h_{w\ i,j,k+1}^t + h_{w\ i,j,k+1}^{t-1} - h_{w\ i,j,k}^t - h_{w\ i,j,k}^{t-1}}{2\Delta z} + 1 \right) - K6 \left( \frac{h_{w\ i,j,k}^t + h_{w\ i,j,k}^{t-1} - h_{w\ i,j,k-1}^t - h_{w\ i,j,k-1}^{t-1}}{2\Delta z} + 1 \right) \right] & \end{aligned} \quad (3.13)$$

For vertical LSOR, the terms can be grouped as

$$-A_k h_{w\ i,j,k+1}^t + B_k h_{w\ i,j,k}^t - C_k h_{w\ i,j,k-1}^t = D_k \quad (3.14)$$

where,

$$A_k = \frac{K5}{2\Delta z^2} \quad (3.15)$$

$$B_k = \frac{C}{\Delta t} + \frac{K1}{2\Delta x^2} + \frac{K2}{2\Delta x^2} + \frac{K3}{2\Delta y^2} + \frac{K4}{2\Delta y^2} + \frac{K5}{2\Delta z^2} + \frac{K6}{2\Delta z^2} \quad (3.16)$$

$$C_k = \frac{K6}{2\Delta z^2} \quad (3.17)$$

$$D_k = \frac{C}{\Delta t} h_{w\ i,j,k}^{t-1} + K1 \left( \frac{h_{w\ i+1,j,k}^t + h_{w\ i+1,j,k}^{t-1} - h_{w\ i,j,k}^{t-1}}{2\Delta x^2} \right) - K2 \left( \frac{h_{w\ i,j,k}^{t-1} - h_{w\ i-1,j,k}^t - h_{w\ i-1,j,k}^{t-1}}{2\Delta x^2} \right) +$$

$$K3 \left( \frac{h_{w\ i,j+1,k}^t + h_{w\ i,j+1,k}^{t-1} - h_{w\ i,j,k}^{t-1}}{2\Delta y^2} \right) - K4 \left( \frac{h_{w\ i,j,k}^{t-1} - h_{w\ i,j-1,k}^t - h_{w\ i,j-1,k}^{t-1}}{2\Delta y^2} \right) +$$

$$K5 \left( \frac{h_{w\ i,j,k+1}^{t-1} - h_{w\ i,j,k}^{t-1}}{2\Delta z^2} + \frac{1}{\Delta z} \right) - K6 \left( \frac{h_{w\ i,j,k}^{t-1} - h_{w\ i,j,k-1}^{t-1}}{2\Delta z^2} + \frac{1}{\Delta z} \right) \quad (3.18)$$

The set of Equation 3.14 for a line scan, form a tri-diagonal matrix equation that can be solved by the well-known triangularization scheme embodied in the following recurrence relation.

$$\left. \begin{aligned} h_{w\ i,j,k}^t &= E_k h_{w\ i,j,k+1}^t + F_k & \text{for } k < M \\ h_{w\ i,j,k}^t &= F_k & \text{for } k = M \end{aligned} \right\} \quad (3.19)$$

where,

$$E_k = \frac{A_k}{B_k - C_k E_{k-1}} \quad \text{for } k > 1; \quad E_1 = \frac{A_1}{B_1} \quad (3.20)$$

$$F_k = \frac{D_k + C_k F_{k-1}}{B_k - C_k E_{k-1}} \quad \text{for } k > 1; \quad F_1 = \frac{D_1}{B_1} \quad (3.21)$$

The E and F coefficients are calculated from  $k=1$  to  $M$  using Equations 3.20 and 3.21 and the  $h_{w\ i,j,k}^t$  back calculated from  $k = M$  to  $1$  using Equation 3.19. At each iteration, it is necessary to predict a pressure head value  $h_{w\ (pred)i,j,k}$  at each node from which the current estimates of K and C can be calculated. For the first iteration of the first time step:

$$h_{w\ (pred)i,j,k}^t = h_{w\ i,j,k}^{t-1} \quad (3.22)$$

For the first iteration of later time step:

$$h_{w\ (pred)i,j,k}^t = (T^t + 1)h_{w\ i,j,k}^{t-1} - T^t h_{w\ i,j,k}^{t-2} \quad (3.23)$$

where,

$$T^t = \Delta t^t / 2\Delta t^{t-1}, \quad T^t = \frac{1}{2} \quad \text{for } \Delta t^t = \Delta t^{t-1} \quad (3.24)$$

For later iterations of all time steps:

$$h_{w (pred)i,j,k}^t = h_{w (pred)i,j,k}^{t,it-1} + \lambda(h_{wi,j,k}^{t,it-1} - h_{w (pred)i,j,k}^{t,it-1}), \quad 0 \leq \lambda \leq 1 \quad (3.25)$$

The values of  $K1$ ,  $K2$ ....., etc. and  $C$  in Equations 3.15 through 3.18 are calculated using the predicted value of  $h_w$ .

$$K1 = \frac{1}{2}(K_{i,j,k} + K_{i+1,j,k}) \quad (3.26)$$

$$K2 = \frac{1}{2}(K_{i,j,k} + K_{i-1,j,k}) \quad (3.27)$$

$$K3 = \frac{1}{2}(K_{i,j,k} + K_{i,j+1,k}) \quad (3.28)$$

$$K4 = \frac{1}{2}(K_{i,j,k} + K_{i,j-1,k}) \quad (3.29)$$

$$K5 = \frac{1}{2}(K_{i,j,k} + K_{i,j,k+1}) \quad (3.30)$$

$$K6 = \frac{1}{2}(K_{i,j,k} + K_{i,j,k-1}) \quad (3.31)$$

$$C = C_{i,j,k} \quad (3.32)$$

The iterations are repeated until the given tolerance is achieved. Although the implicit scheme is unconditionally stable, some difficulties due to the strong nonlinearity of the Richards' equation may occur. Which can be overcome by the adaptable time step, however in this model very small time step is used.

Similarly we can get the finite difference form of Equations 3.6 and 3.7.

### 3.2.2 Surface flow and erosion/deposition model

#### Governing equations

The mathematical model developed by Takahashi and Nakagawa (1994) was used to investigate the surface flow and erosion/deposition on the surface of the model slope. The depth-wise averaged two-dimensional momentum equations for the  $x$ -wise (down valley) and  $y$ -wise (lateral) directions are

$$\frac{\partial M}{\partial t} + \beta \frac{\partial(uM)}{\partial x} + \beta \frac{\partial(vM)}{\partial y} = gh \sin \theta_{bxo} - gh \cos \theta_{bxo} \frac{\partial(h + z_b)}{\partial x} - \frac{\tau_{bx}}{\rho_T} \quad (3.33)$$

and

$$\frac{\partial N}{\partial t} + \beta \frac{\partial(uN)}{\partial x} + \beta \frac{\partial(vN)}{\partial y} = gh \sin \theta_{b_{yo}} - gh \cos \theta_{b_{yo}} \frac{\partial(h+z_b)}{\partial y} - \frac{\tau_{by}}{\rho_T} \quad (3.34)$$

The continuity of the total volume is

$$\frac{\partial h}{\partial t} + \frac{\partial M}{\partial x} + \frac{\partial N}{\partial y} = i_b \{c_* + (1-c_*)s_b\} + R - I \quad (3.35)$$

The continuity equation of the particle fraction is

$$\frac{\partial(ch)}{\partial t} + \frac{\partial(cM)}{\partial x} + \frac{\partial(cN)}{\partial y} = i_b c_* \quad (3.36)$$

The equation for the change of bed surface elevation is

$$\frac{\partial z_b}{\partial t} = -i_b \quad (3.37)$$

where  $M (=uh)$  and  $N (=vh)$  are the flow discharge per unit width in  $x$  and  $y$  directions;  $u$  and  $v$  are depth averaged velocities in  $x$  and  $y$  directions;  $h$  is the water depth;  $g$  is the gravitational acceleration;  $\beta$  is the momentum correction factor;  $\rho_T$  is the mixture density;  $\tau_{bx}$  and  $\tau_{by}$  are the bottom shear stresses in  $x$  and  $y$  directions;  $R$  is the rainfall intensity;  $I$  is the infiltration rate;  $s_b$  is the degree of saturation in the bed;  $i_b$  is the rate of hydraulic erosion or deposition from the flowing water;  $c$  is the sediment concentration in the flow;  $c_*$  is the maximum sediment concentration in the bed; and  $z_b$  is the erosion or deposition thickness measured from the original bed elevation.

Takahashi (1991) categorized the flow as: a) stony debris flow ( $c \geq 0.4c_*$ ), b) immature debris flow ( $0.4c_* > c \geq 0.1c_*$ ) and c) turbulent flow ( $c < 0.1c_*$ ); based on sediment concentration in the flow and proposed different flow resistance equations for each types of flow.

For stony debris flow

$$\tau_{bx} = \frac{1}{8} \left( \frac{d_m}{h} \right)^2 \sigma \lambda^2 u \sqrt{u^2 + v^2} = \frac{\rho_T}{8} \left( \frac{d_m}{h} \right)^2 \frac{u \sqrt{u^2 + v^2}}{\{c + (1-c)\rho/\sigma\} \{(c_*/c)^{1/3} - 1\}^2} \quad (3.38)$$

$$\tau_{by} = \frac{1}{8} \left( \frac{d_m}{h} \right)^2 \sigma \lambda^2 v \sqrt{u^2 + v^2} = \frac{\rho_T}{8} \left( \frac{d_m}{h} \right)^2 \frac{v \sqrt{u^2 + v^2}}{\{c + (1-c)\rho/\sigma\} \{(c_*/c)^{1/3} - 1\}^2} \quad (3.39)$$

For immature debris flow

$$\tau_{bx} = \frac{\rho_T}{0.49} \left( \frac{d_m}{h} \right)^2 u \sqrt{u^2 + v^2} \quad (3.40)$$

$$\tau_{by} = \frac{\rho_T}{0.49} \left( \frac{d_m}{h} \right)^2 v \sqrt{u^2 + v^2} \quad (3.41)$$

For turbulent flow

$$\tau_{bx} = \frac{\rho g n^2 u \sqrt{u^2 + v^2}}{h^{1/3}} \quad (3.42)$$

$$\tau_{by} = \frac{\rho g n^2 v \sqrt{u^2 + v^2}}{h^{1/3}} \quad (3.43)$$

where,  $n$  is the Manning's roughness coefficient and  $d_m$  is the mean diameter of particles.

The erosion velocity for unsaturated bed given by Takahashi (1991) is as follows.

$$\frac{i_b}{\sqrt{gh}} = K_e \sin^{3/2} \theta_b \left\{ 1 - \frac{\sigma - \rho_T}{\rho_T} c \left( \frac{\tan \phi}{\tan \theta} - 1 \right) \right\}^{1/2} \cdot \left( \frac{\tan \phi}{\tan \theta} - 1 \right) (c_\infty - c) \frac{h}{d_m} \quad (3.44)$$

where,  $\phi$  is the internal friction angle of the bed,  $K_e$  is the parameter of erosion velocity and  $c_\infty$  is the equilibrium solids concentration defined by the following equations (Nakagawa et al., 2003).

For stony debris flow ( $\tan\theta > 0.138$ )

$$c_\infty = \frac{\rho \tan \theta}{(\sigma - \rho)(\tan \phi - \tan \theta)} \quad (3.45)$$

For immature debris flow ( $0.138 \geq \tan\theta > 0.03$ )

$$c_\infty = 6.7 \left\{ \frac{\rho \tan \theta}{(\sigma - \rho)(\tan \phi - \tan \theta)} \right\}^2 \quad (3.46)$$

For turbulent flow ( $0.03 \geq \tan\theta$ )

$$c_\infty = \frac{(1 + 5 \tan \theta) \tan \theta}{\sigma / \rho - 1} \left( 1 - \alpha_0^2 \frac{\tau_{*c}}{\tau_*} \right) \left( 1 - \alpha_0 \sqrt{\frac{\tau_{*c}}{\tau_*}} \right) \quad (3.47)$$

Where,  $\theta$  is water surface gradient, and

$$\alpha_0^2 = \frac{2\{0.425 - (\sigma / \rho) \tan \theta / (\sigma / \rho - 1)\}}{1 - (\sigma / \rho) \tan \theta / (\sigma / \rho - 1)} \quad (3.48)$$

$$\tau_{*c} = 0.04 \times 10^{1.72 \tan \theta} \quad (3.49)$$

$$\tau_* = \frac{h \tan \theta}{(\sigma / \rho - 1) d_m} \quad (3.50)$$

in which  $\tau_{*c}$  is the non-dimensional critical shear stress and  $\tau_*$  is the non-dimensional shear stress.

If the slope is steeper than about 9 degrees and  $c_{s\infty}$  by Equation 3.43 calculates the value less than  $c_\infty$

$$c_{s\infty} = 6.7c_\infty^2 \quad (3.51)$$

and for the slope on which  $c_{s\infty}$  by Equation 3.43 count less than 0.01,  $c_{s\infty}$  should be obtained by using appropriate bed load equation.

The deposition velocity given by Takahashi (1991) is as follows.

$$i_b = \delta_d \frac{c_\infty - c}{c_*} \sqrt{u^2 + v^2} \quad (3.52)$$

where,  $\delta_d$  is a constant.

### Solution approach

The finite difference form of the Equations 3.33 to 3.36 can be obtained by the solution methods developed by Nakagawa (1989) using Leap-Frog scheme. As shown in Figure 3.1, vector quantities such as  $M$ ,  $N$  and  $u$ ,  $v$  are defined in the middle of the cell and scalar quantities such as  $h$ ,  $c$  are defined in the center of the cell. In this method of solution, three-time-level variables are necessary, i.e.,  $n$ ,  $n+1$ , and  $n+2$  to get a value at  $t = (n+3)\Delta t$ . For example, scalar value  $h^{n+3}$  is obtained by using  $h^{n+1}$  and  $M^{n+2}$  and vector value  $M^{n+2}$  is obtained by using  $h^{n+1}$  and  $M^n$ , i.e., each time level of  $h$  and  $M$  is different. The scalar values such as  $h$ ,  $C$  and  $z_b$  are set in the middle of the cell and the vector value  $M$  is set on the grid. Figure 3.2 shows the hydraulic variables arrangement and their calculation methodology.

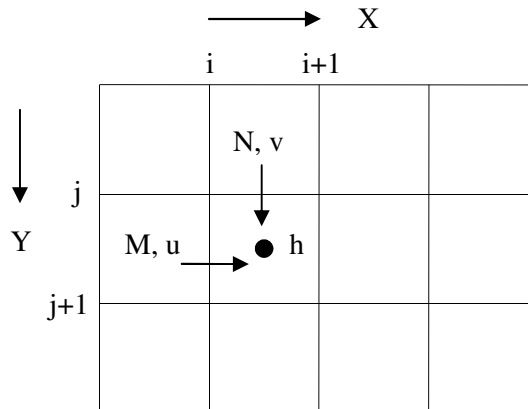


Figure 3.1 Hydraulic variables arrangement on meshes

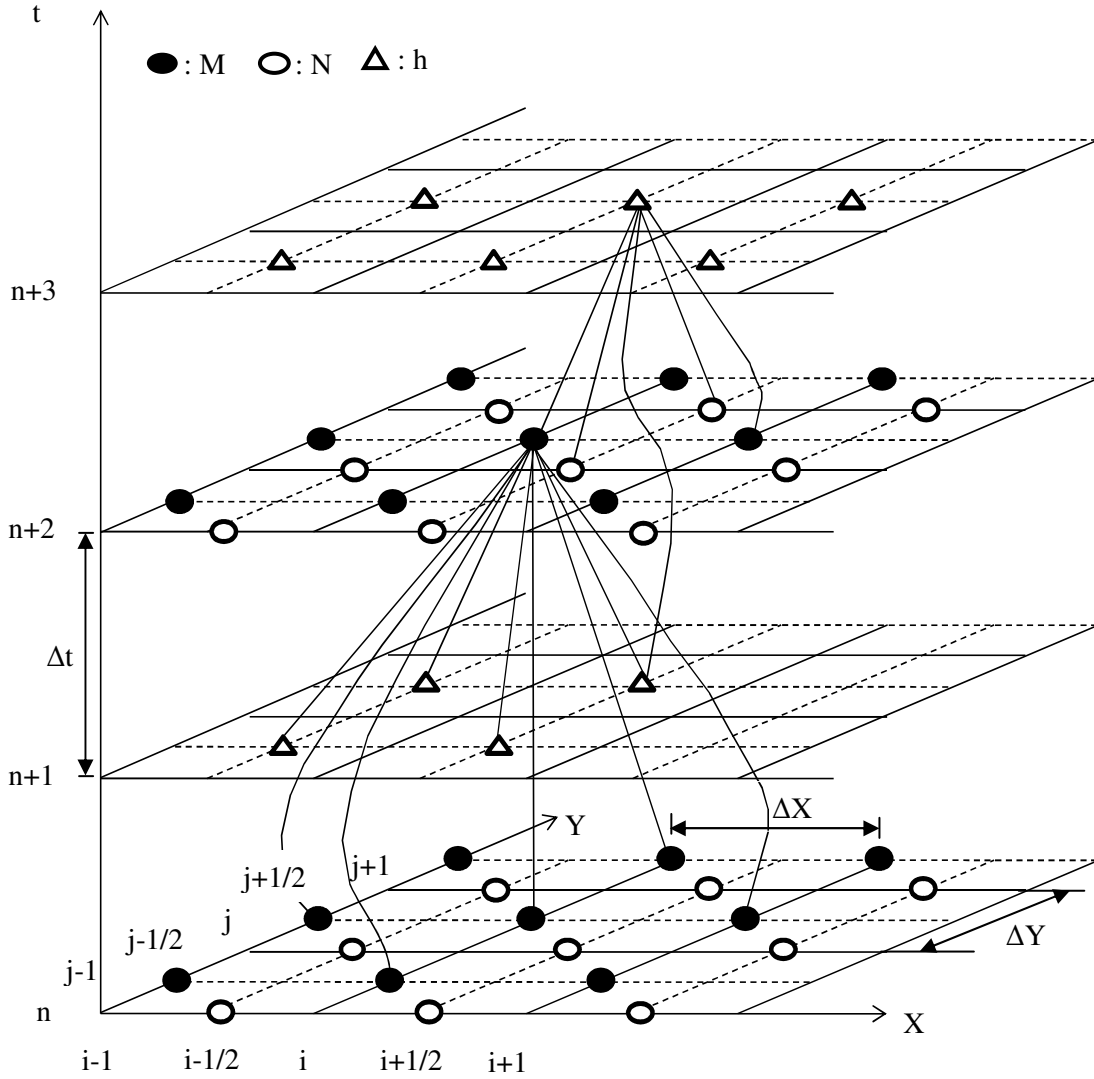


Figure 3.2 Hydraulic variables arrangement and calculation methodology

The expression of the Equation 3.25 in finite difference form of is as follows.

$$\frac{M_{i,j+1/2}^{n+2} - M_{i,j+1/2}^n}{2\Delta t} + \beta \begin{cases} \frac{u_{i,j+1/2}^n M_{i,j+1/2}^n - u_{i-1,j+1/2}^n M_{i-1,j+1/2}^n}{\Delta x} & : u_{i,j+1/2}^n \geq 0, u_{i-1,j+1/2}^n \geq 0 \\ \frac{u_{i,j+1/2}^n M_{i,j+1/2}^n - 0}{\Delta x} & : u_{i,j+1/2}^n \geq 0, u_{i-1,j+1/2}^n < 0 \\ \frac{u_{i+1,j+1/2}^n M_{i+1,j+1/2}^n - u_{i,j+1/2}^n M_{i,j+1/2}^n}{\Delta x} & : u_{i,j+1/2}^n < 0, u_{i-1,j+1/2}^n < 0 \\ \frac{0 - u_{i,j+1/2}^n M_{i,j+1/2}^n}{\Delta x} & : u_{i,j+1/2}^n < 0, u_{i+1,j+1/2}^n \geq 0 \end{cases}$$

$$\begin{aligned}
& + \beta \left\{ \begin{array}{l} \frac{\tilde{v}_{i,j+1/2}^n M_{i,j+1/2}^n - \tilde{v}_{i,j-1/2}^n M_{i,j-1/2}^n}{\Delta y} : \tilde{v}_{i,j+1/2}^n \geq 0, \tilde{v}_{i,j-1/2}^n \geq 0 \\ \frac{\tilde{v}_{i,j+1/2}^n M_{i,j+1/2}^n - 0}{\Delta y} : \tilde{v}_{i,j+1/2}^n \geq 0, \tilde{v}_{i,j-1/2}^n < 0 \\ \frac{\tilde{v}_{i,j+3/2}^n M_{i,j+3/2}^n - \tilde{v}_{i,j+1/2}^n M_{i,j+1/2}^n}{\Delta y} : \tilde{v}_{i,j+1/2}^n < 0, \tilde{v}_{i,j+3/2}^n < 0 \\ \frac{0 - \tilde{v}_{i,j+1/2}^n M_{i,j+1/2}^n}{\Delta y} : \tilde{v}_{i,j+1/2}^n < 0, \tilde{v}_{i,j+3/2}^n \geq 0 \end{array} \right. = g\bar{h} \sin \theta_{bx0} \\
& - g\bar{h} \cos \theta_{bx0} \frac{(h+z_b)_{i+1/2,j+1/2}^{n+1} - (h+z_b)_{i-1/2,j+1/2}^{n+1}}{\Delta x} - \frac{u_{i,j+1/2}}{\sqrt{(u_{i+1/2,j}^n)^2 + (v_{i+1/2,j}^n)^2}} \\
& \cdot \frac{f(\bar{C}_L)(\sigma - \rho)g\bar{h} \cos \theta_{xi+1/2,j+1/2}^{n+1} + \cos \theta_{xi-1/2,j+1/2}^{n+1} \tan \phi}{\bar{\rho}_T} \frac{2}{2} \\
& - \rho \cdot \frac{1}{\bar{\rho}_T} \frac{f_{bi+1/2,j+1/2}^{n+1} + f_{bi-1/2,j+1/2}^{n+1}}{2} u_{i,j+1/2} \sqrt{(u_{i+1/2,j}^n)^2 + (v_{i+1/2,j}^n)^2} + \frac{\tau_{sx}}{\bar{\rho}_T} \quad (3.53)
\end{aligned}$$

where,

$$u_{i,j+1/2}^n = \frac{2M_{i,j+1/2}^n}{h_{i-1/2,j+1/2}^{n+1} + h_{i+1/2,j+1/2}^{n+1}} ; v_{i+1/2,j}^n = \frac{2N_{i+1/2,j}^n}{h_{i+1/2,j-1/2}^{n+1} + h_{i+1/2,j+1/2}^{n+1}} \quad (3.54)$$

$$\tilde{v}_{i,j+1/2}^n = \frac{1}{4} (v_{i-1/2,j}^n + v_{i-1/2,j+1}^n + v_{i+1/2,j}^n + v_{i+1/2,j+1}^n) \quad (3.55)$$

$$\bar{h} = \frac{h_{i-1/2,j+1/2}^{n+1} + h_{i+1/2,j+1/2}^{n+1}}{2} \quad (3.56)$$

$$\bar{\rho}_T = (\sigma - \rho) \bar{c} + \rho \quad (3.57)$$

$$\bar{c} = \frac{c_{i-1/2,j+1/2}^{n+1} + c_{i+1/2,j+1/2}^{n+1}}{2} \quad (3.58)$$

Similarly, we can get the finite difference form of Equation 3.34. The finite difference form of Equations 3.35 and 3.36 are as follows.

$$\frac{h_{i+1/2,j+1/2}^{n+3} - h_{i+1/2,j+1/2}^{n+1}}{2\Delta t} + \frac{M_{i+1,j+1/2}^{n+2} - M_{i,j+1/2}^{n+2}}{2\Delta x} + \frac{N_{i+1/2,j+1}^{n+2} - N_{i+1/2,j}^{n+2}}{2\Delta y} = i_{bi+1/2,j+1/2}^{n+1} \quad (3.59)$$

$$\begin{aligned}
& \frac{(ch)_{i+1/2,j+1/2}^{n+3} - (ch)_{i+1/2,j+1/2}^{n+1} h_{i+1/2,j+1/2}^{n+1}}{2\Delta t} + \frac{Q_{xi+1,j+1/2}^{n+2} - Q_{xi,j+1/2}^{n+2}}{2\Delta x} \\
& + \frac{Q_{yi+1/2,j+1}^{n+2} - Q_{yi+1/2,j}^{n+2}}{2\Delta y} = i_{bi+1/2,j+1/2}^{n+1} C_* \quad (3.60)
\end{aligned}$$

where,

$$Q_{x\ i,j+1/2}^{n+2} = \begin{cases} M_{i,j+1/2}^{n+2} C_{i-1/2,j+1/2}^{n+1} ; & M_{i,j+1/2}^{n+2} \geq 0 \\ M_{i,j+1/2}^{n+2} C_{i+1/2,j+1/2}^{n+1} ; & M_{i,j+1/2}^{n+2} < 0 \end{cases} \quad (3.61)$$

$$Q_{x\ i+1,j+1/2}^{n+2} = \begin{cases} M_{i+1,j+1/2}^{n+2} C_{i-1/2,j+1/2}^{n+1} ; & M_{i+1,j+1/2}^{n+2} \geq 0 \\ M_{i+1,j+1/2}^{n+2} C_{i+1/2,j+1/2}^{n+1} ; & M_{i+1,j+1/2}^{n+2} < 0 \end{cases} \quad (3.62)$$

$$Q_{y\ i+1/2,j}^{n+2} = \begin{cases} N_{i+1/2,j}^{n+2} C_{i+1/2,j-1/2}^{n+1} ; & N_{i+1/2,j}^{n+2} \geq 0 \\ N_{i+1/2,j}^{n+2} C_{i+1/2,j+1/2}^{n+1} ; & N_{i+1/2,j}^{n+2} < 0 \end{cases} \quad (3.63)$$

$$Q_{y\ i+1/2,j+1}^{n+2} = \begin{cases} N_{i+1/2,j+1}^{n+2} C_{i+1/2,j-1/2}^{n+1} ; & N_{i+1/2,j+1}^{n+2} \geq 0 \\ N_{i+1/2,j+1}^{n+2} C_{i+1/2,j+1/2}^{n+1} ; & N_{i+1/2,j+1}^{n+2} < 0 \end{cases} \quad (3.64)$$

### 3.2.3 Boundary conditions

In seepage flow model, top surface boundary conditions are allowed as the constant head or the constant flux due to a rainfall event in the equation for water-phase. However, in equation for air phase no air flow at the surface or variable air pressure head is allowed. Downstream boundary condition is modeled as seepage face with zero pressure head; and upstream, left and right boundaries are considered as no flow boundaries for both water and air phase equations.

If rainfall rates are less than the maximum infiltration capacity of the soil surface and no overland flow, then ponding will not occur on the surface. Under such circumstances, all precipitation becomes infiltration and the flux boundary condition applies.

$$q_{win} = K_{wz} \left( \frac{\partial h_w}{\partial z} + 1 \right) = RI \quad (3.65)$$

$$h_{a(sur)} = 0 \quad (3.66)$$

If rainfall rates are more than the maximum infiltration capacity of the soil surface and/or overland flow occurs, then head boundary condition is applied.

$$h_{w(sur)} = h \quad (3.67)$$

$$h_{a(sur)} = h + h_{ae} \quad (3.68)$$

$$\text{If } h_{a(sur)} \geq h_{a(top)}, \quad q_{ain} = K_{az} \left( \frac{\partial h_a}{\partial z} + \frac{\rho_a}{\rho_{ow}} \right) = 0 \quad (3.69)$$

where,  $q_{win}$  and  $q_{ain}$  are the prescribed water and air flux in vertical direction respectively;  $h_{w(sur)}$  and  $h_{a(sur)}$  are surface water pressure head and air pressure head respectively;  $h_{a(top)}$  is the air pressure head at the top cell of the considered soil domain; and  $h_{ae}$  is the air entry head that can be determined by the following expression (Leong and Rahardjo, 1997).

$$h_{ae} = \frac{1}{\alpha} \left[ \frac{\eta - 1}{\eta(m + 1) - \eta + 1} \right]^{1/\eta} \quad (3.70)$$

For water surface flow and erosion/deposition model, downstream condition is modeled as outflow boundary, and upstream, left and right conditions are considered as no flow boundaries.

### 3.2.4 Results and discussions

Numerical simulation was carried out with time step of 0.01 second and space steps of 2.5cm in x (longitudinal), y (lateral) and z (vertical) directions. Both x and y directions were assumed horizontal. In surface water flow and erosion/deposition model, the time step of 0.005sec and space steps of 2.5cm in x (parallel to longitudinal axis of flume) and y (horizontal) directions respectively. To validate the model two experimental cases were considered. The experiments were carried out on 23° and 28° flume slope (Figures 2.9 and 2.10 in section 2.3).

Figures 3.3 and 3.4 show the simulated and experimental moisture content profiles at different SRs. Since the electromagnetic field of a sensor extends up to 60mm into the soil (section 2.2.3), the influence of SR8 and SR10 (23° flume slope case) and the influence of SR6 and SR10 (28° flume slope case) reaches up to the soil surface in the sloping face of the model slope (Figures 2.9 and 2.10 in section 2.3). So, in these sensors case moisture profiles in experiments and simulations are not matching well. However, in case of other sensors the profiles are in good agreement.

Essentially air becomes trapped in the voids by the infiltrating water from the surface, initially causing compression of the air phase, leading to a reduction in the rate of water infiltration. The air pressure will increase until it reaches a sufficient value for the air to escape by bubbling. Moisture profiles obtained considering two-phase flow was found a little bit delayed in comparison with that of one-phase flow (Figures 3.3 and 3.4). Comparison of air pressure head profiles at different PTs, obtained from simulation and experiments, are also in good agreement (Figures 3.5 and 3.6). Location of these transducers within the body of model slope is presented in Figures 2.9 and 2.10 in section 2.3.

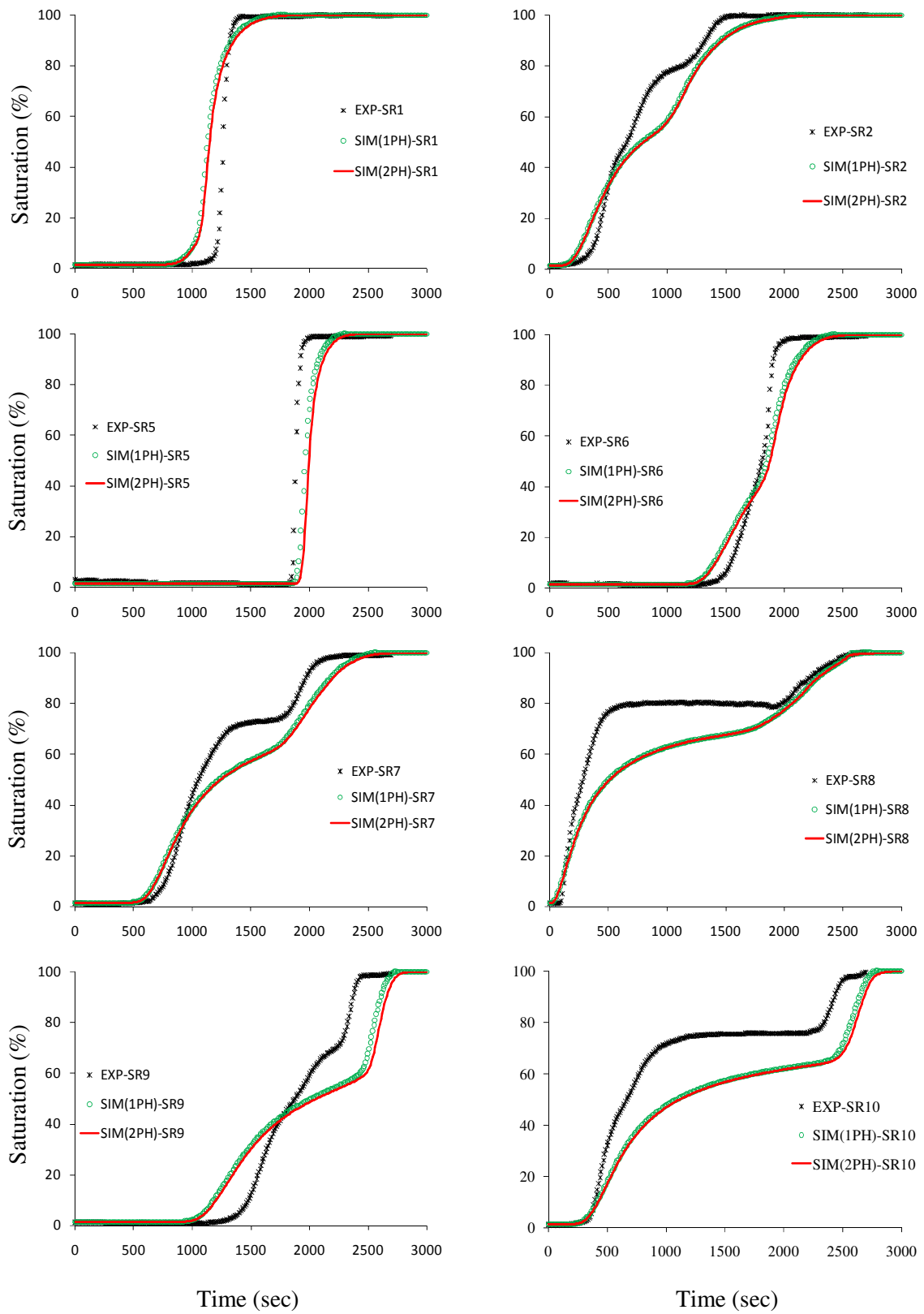


Figure 3.3 Simulated and experimental moisture content profiles (23° flume slope)

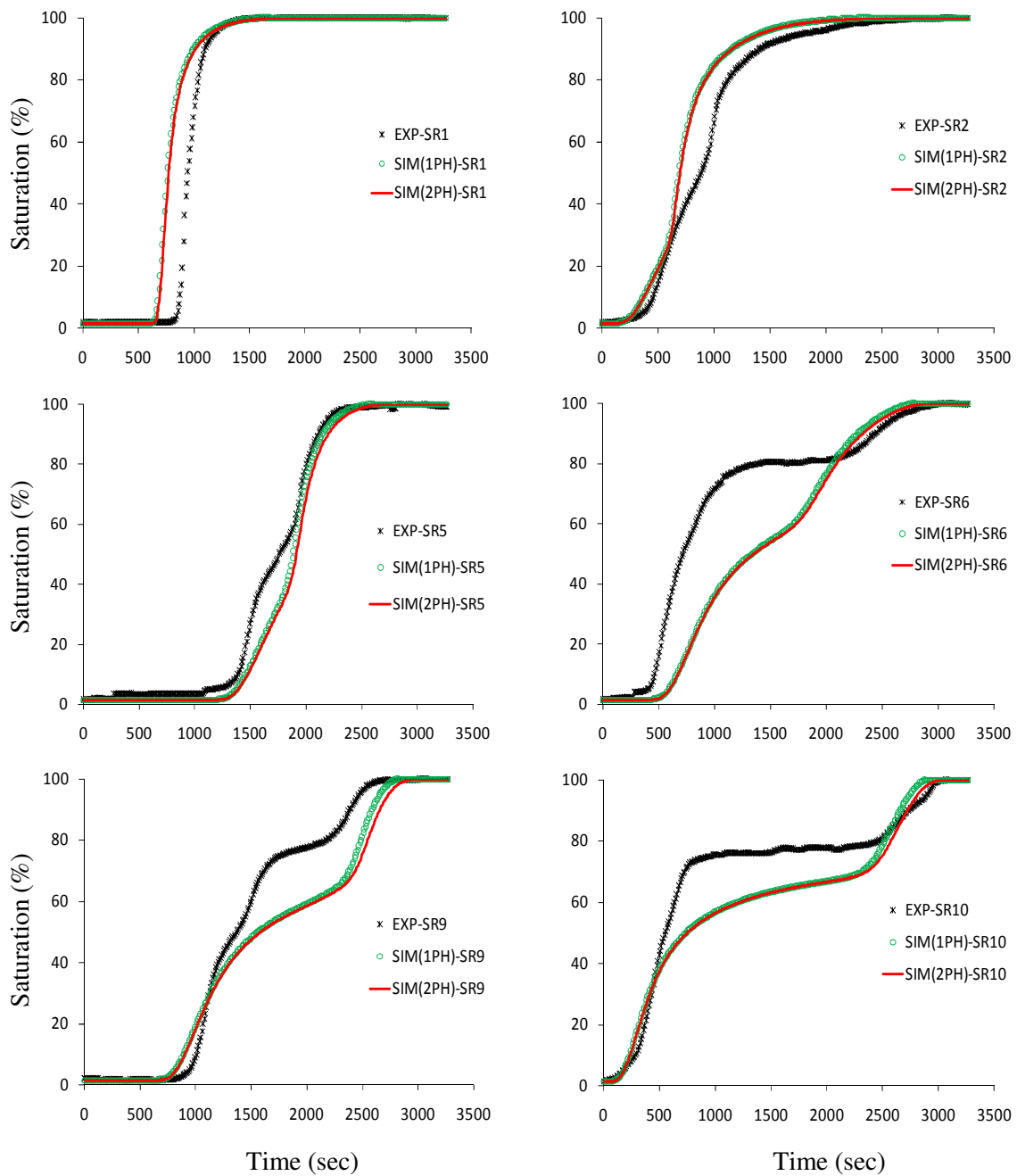


Figure 3.4 Simulated and experimental moisture content profiles (28° flume slope)

Figures 3.7 to 3.14 present contours of numerically calculated moisture at different time, within the body of model slope, at longitudinal section through centre line and cross-section through PR1, PR2 and PR3. These figures also compare the calculated moistures with experimentally observed moistures. Similarly, Figures 3.15 to 3.22 present contours of numerically calculated air pressure head at different time, within the body of model slope, at longitudinal section through centre line and cross-section through PT1, PT2 and PR3. These figures also compare

the calculated air pressure head with experimentally observed air pressure head. Figures 3.23 and 3.24 show the surface of the model slope and water surface front at 2,800 seconds at different cases. Erosion deposition condition of the soil surface is also observed in case of 23° flume slope. In experiment, erosion process observed in 23° flume case only, just few seconds before the failure of the slope model. Comparison of experimental and simulated surface water forefront propagation time to different measurement scales is presented in the Tables 3.1 and 3.2. Experimental and simulated seepage out flow from the downstream seepage face is shown in Figures 3.25 and 3.26. All the simulation results compared to experimental data are in good agreement.

The effect of unreliable rainfall supply is clearly observed in the comparison of experimental and simulation results. In 23° flume slope case, full saturation of moisture profiles in simulation is delayed than that of experiments in almost all the sensors (Figure 3.3). Air pressure head

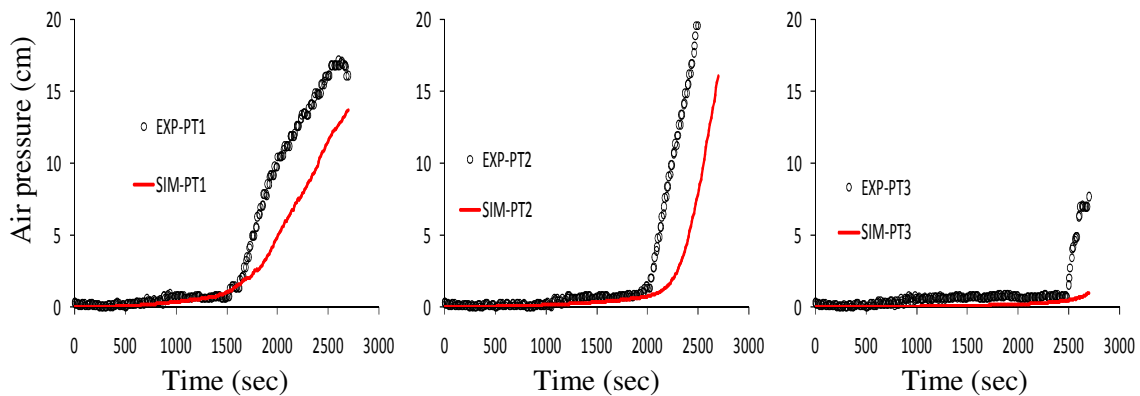


Figure 3.5 Simulated and experimental air pressure head profiles (23° flume slope)

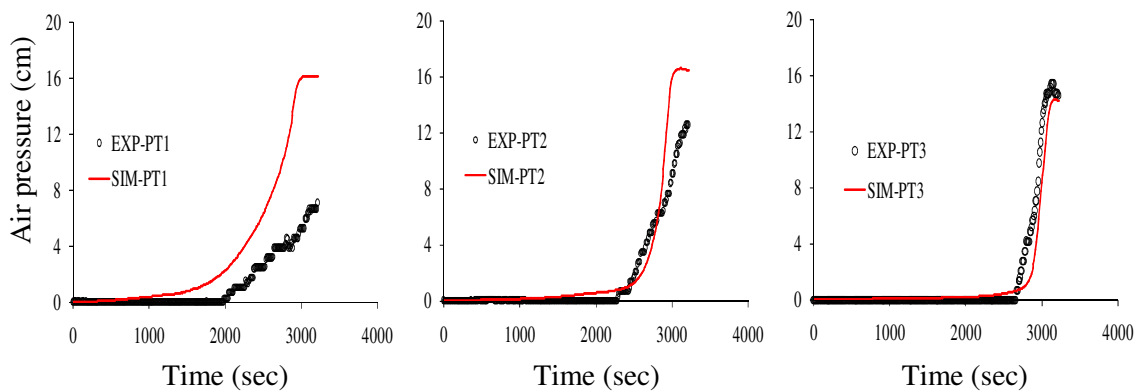


Figure 3.6 Simulated and experimental air pressure head profiles (28° flume slope)

profiles (Figure 3.5) and surface water forefront propagation (Table 3.1) is also delayed in simulation than experiment. These results are indication of higher rainfall intensity in experiment than the observed average values. In 28° flume slope case, full saturation of moisture profiles in simulation is earlier than that of experiments in almost all the sensors (Figure 3.3). Air pressure head profiles except in PT3 (Figure 3.5) and surface water forefront propagation (Table 3.1) is also faster in simulation than experiment. These results are indication of lesser rainfall intensity in experiment than the observed average values. Since PT3 is located close to downstream end of the model slope and surface water was not propagated up to this reach, simulation air pressure head profile in its position is only influenced by the localize rainfall intensity just above it. This localize rainfall intensity may be lesser in simulation than the actual value. The experiments for 23° flume slope were carried out in winter season where as the experiments for 28° flume slope were carried out in summer season. So rainfall intensity in former case was higher than the average rainfall value and in later case it was lesser than the average value.

Since the rainfall intensity was more intense towards side A than B (Figure 2.13 in section 2.4), the rate of infiltration also observed faster in side A than side B (Figures 3.8, 3.9, 3.10, 3.13 and 3.14). However, there is higher rainfall intensity in side B than side A in the PR1 section of 28° flume case so that the rate of infiltration also observed faster in side B than side A (Figure 3.12).

Due to the reduction in the rate of water infiltration by the influence of air phase, water surface forefront propagation in two-phase simulation should be faster than one-phase simulation. However in some stages of water surface forefront, the degree of saturation of the soil just below the forefront will be lesser due to the delay in lateral movement of seepage water from upstream. In such stages, infiltration rate from surface will be higher so that propagation rate may delay substantially. In case of the positions of measuring scale 2 of 23° flume slope case (Table 3.1), surface water propagated time is a little bit delay in two-phase than one-phase. In case of measuring scale 4 of 28° flume slope case (Table 3.2), surface water propagated time is same in two-phase and one-phase simulations. In other scales position surface water propagated time is faster in two-phase than one-phase.

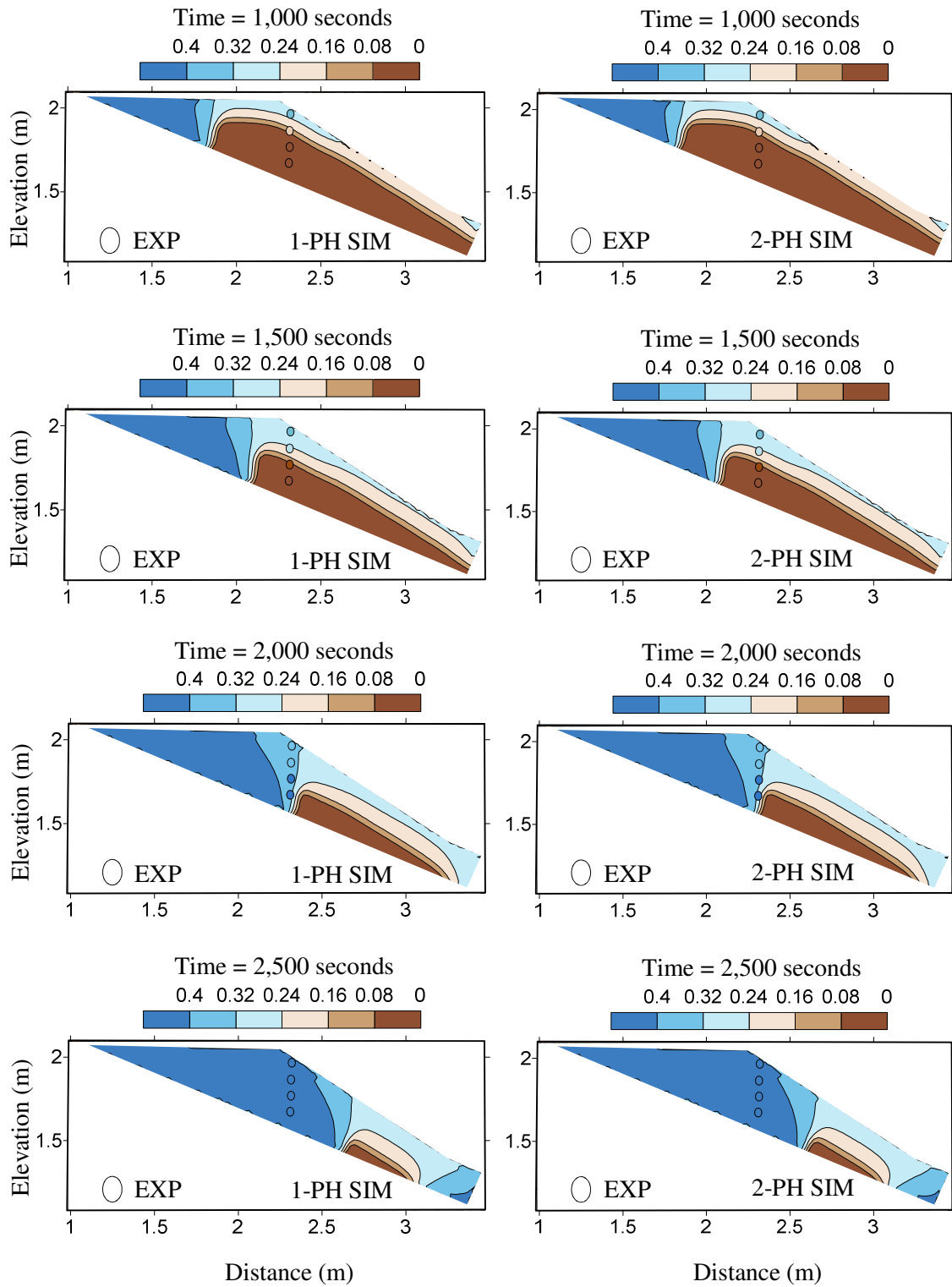


Figure 3.7 Moisture counter at longitudinal section through centre line (23° flume slope)

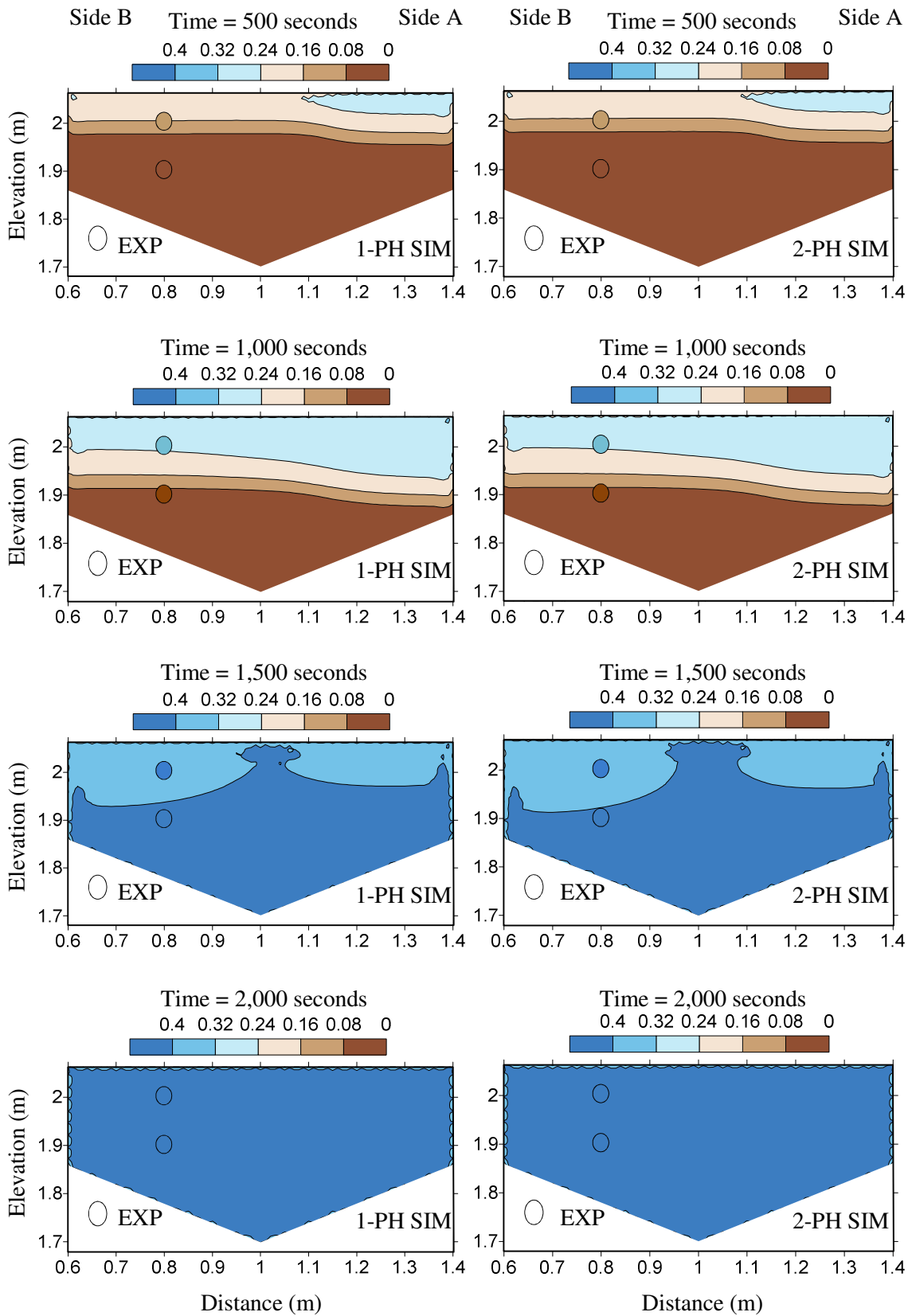


Figure 3.8 Moisture counter at cross section through PR1 (23° flume slope)

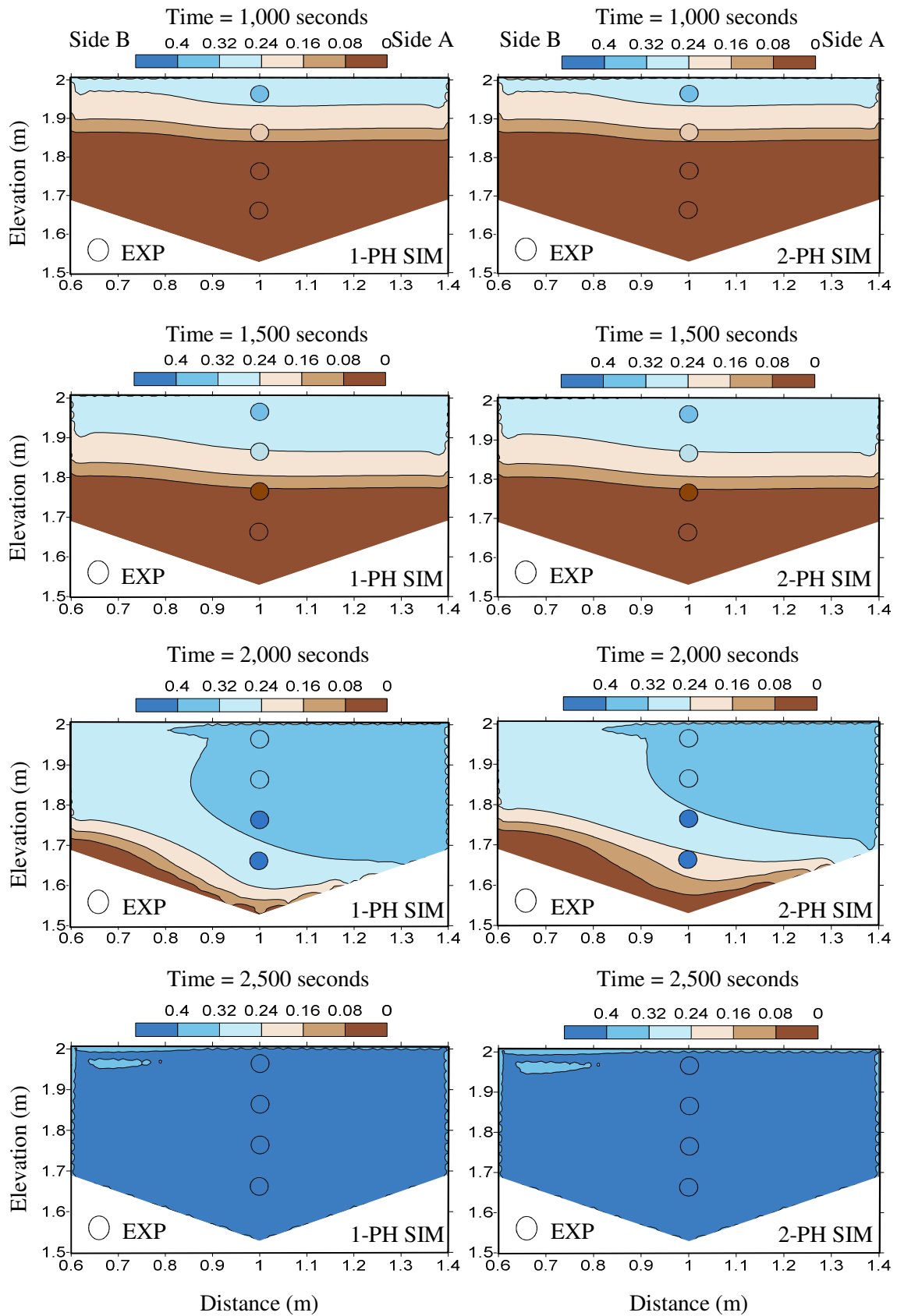


Figure 3.9 Moisture counter at cross section through PR2 (23° flume slope)

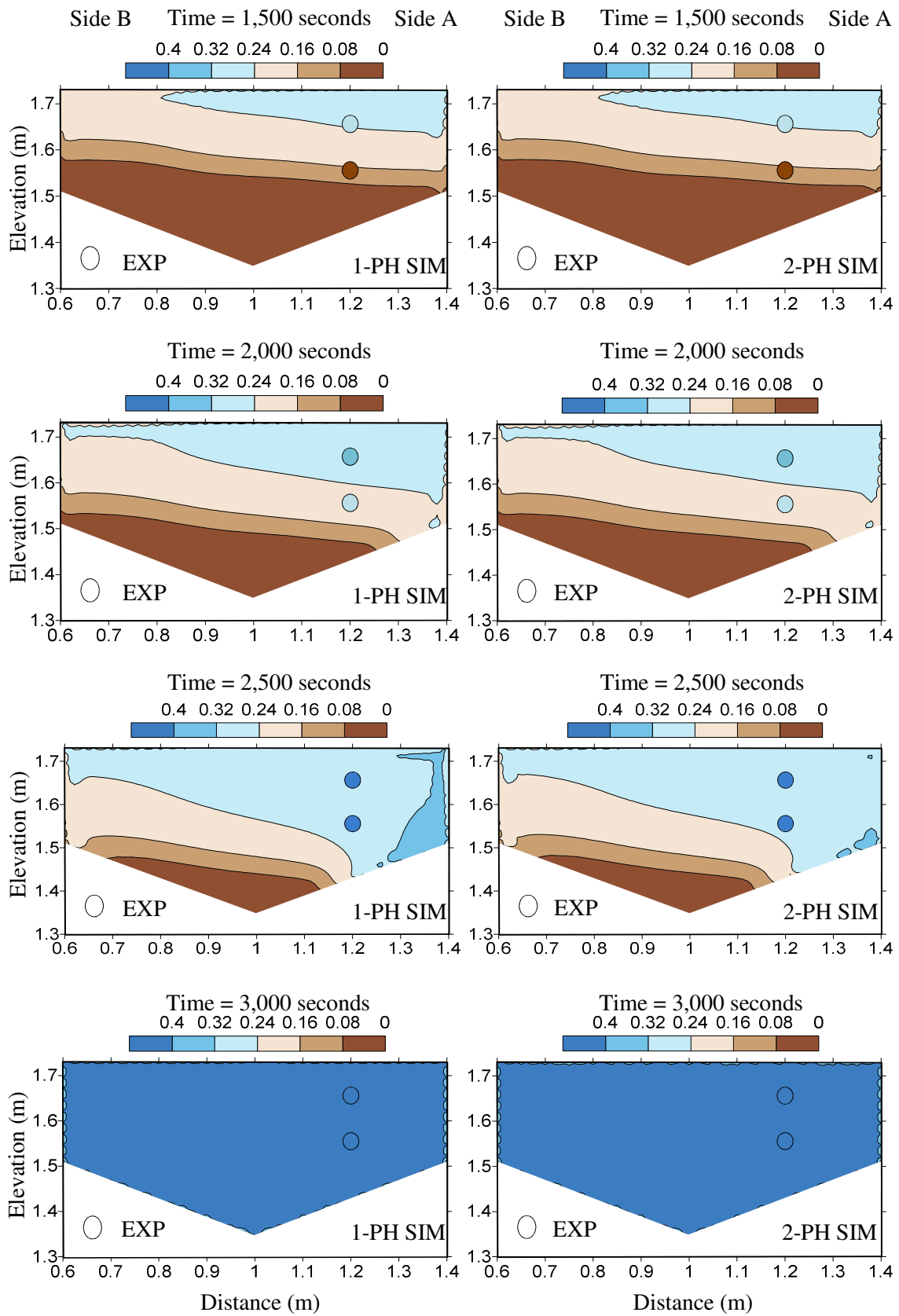


Figure 3.10 Moisture counter at cross section through PR3 (23° flume slope)

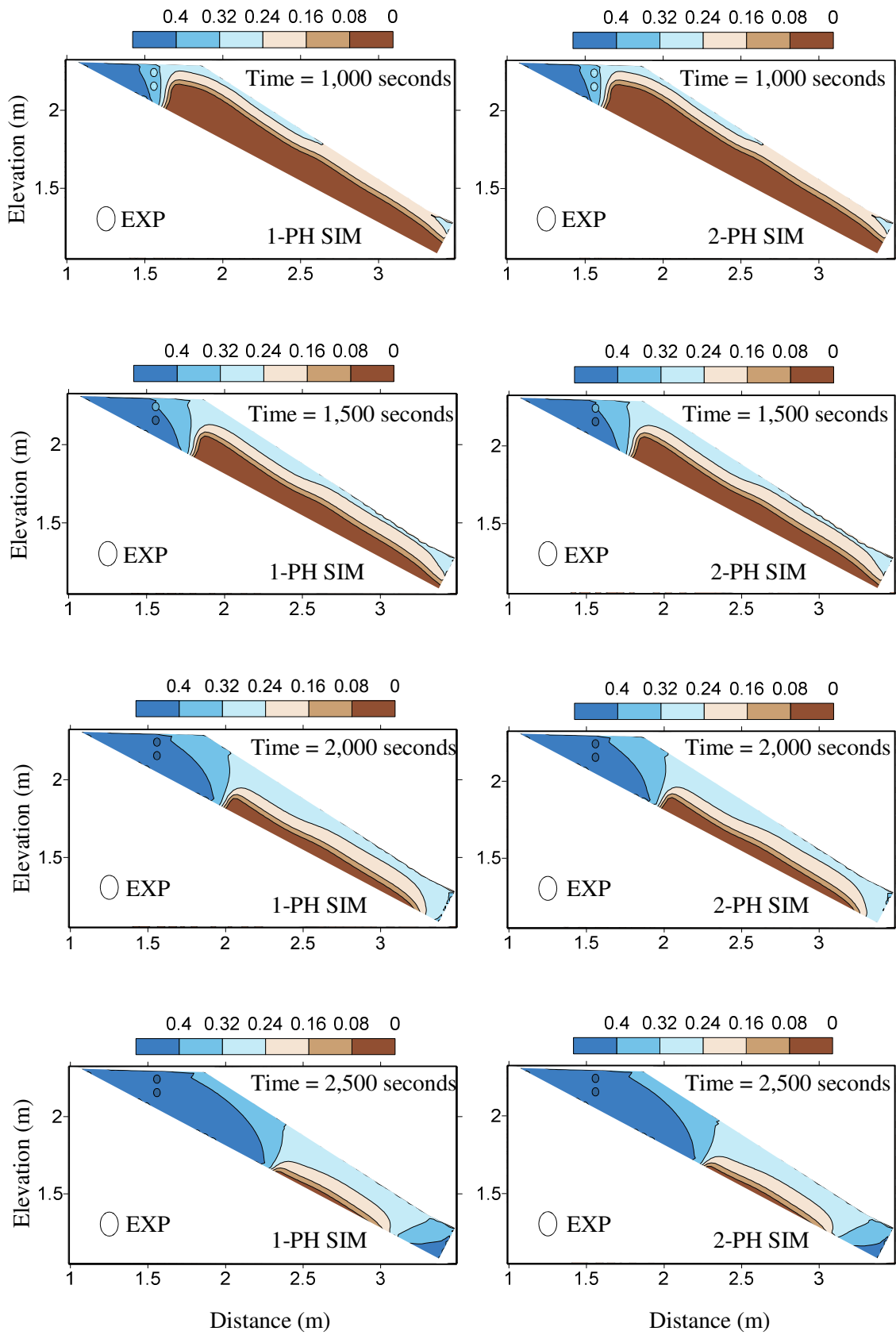


Figure 3.11 Moisture counter at longitudinal section through centre line ( $28^\circ$  flume slope)

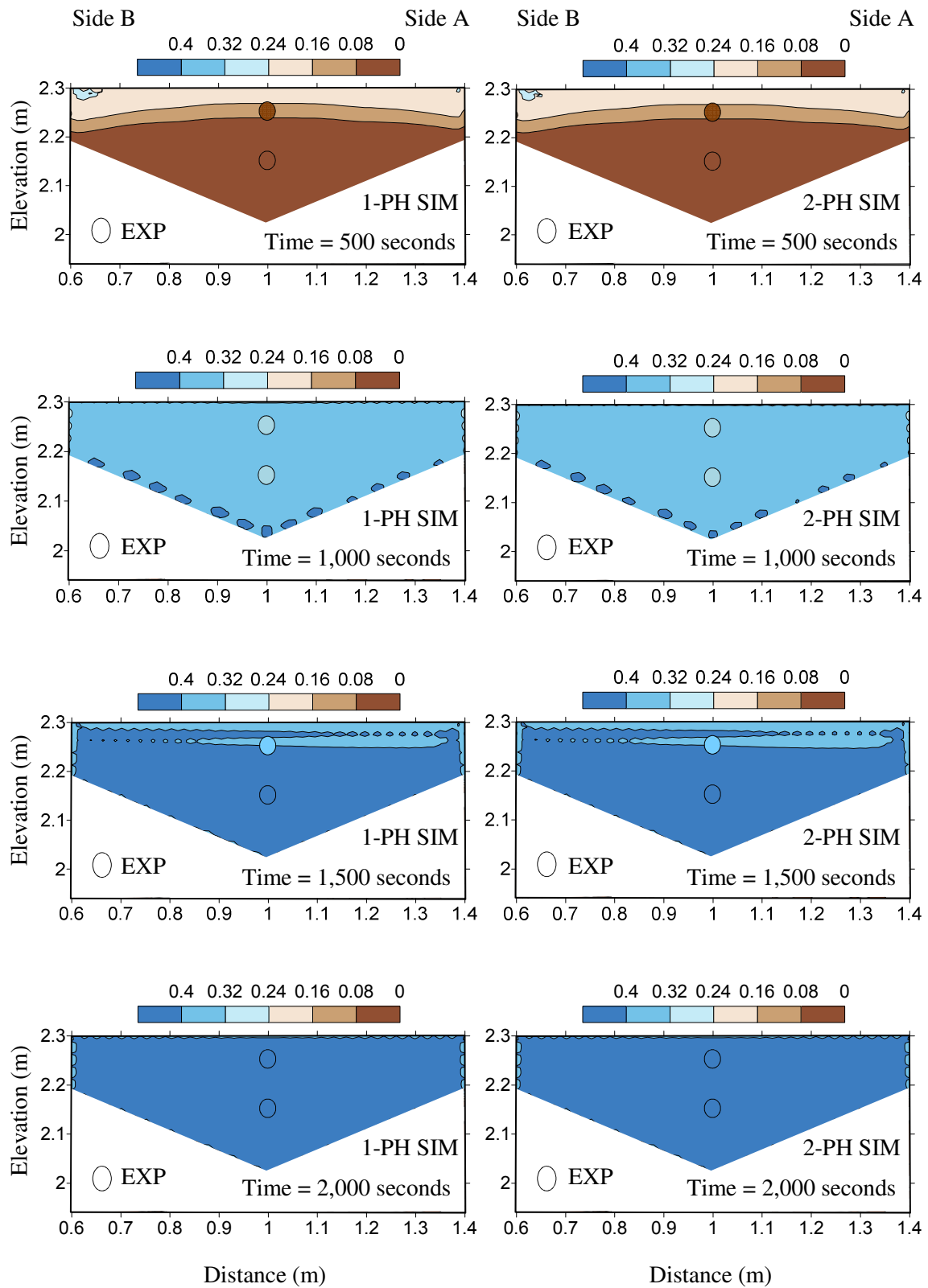


Figure 3.12 Moisture counter at cross section through PR1 (28° flume slope)

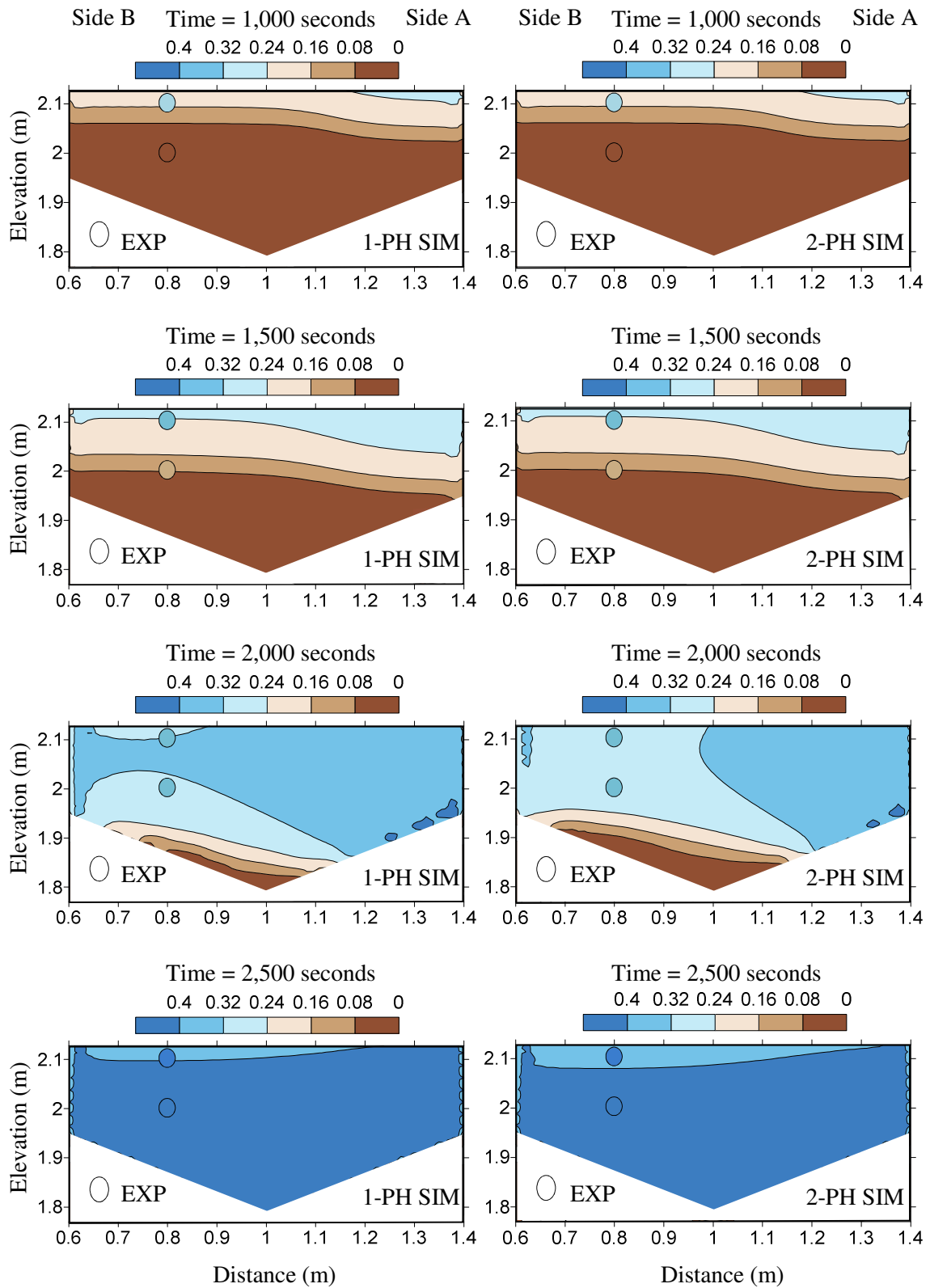


Figure 3.13 Moisture counter at cross section through PR2 (28° flume slope)

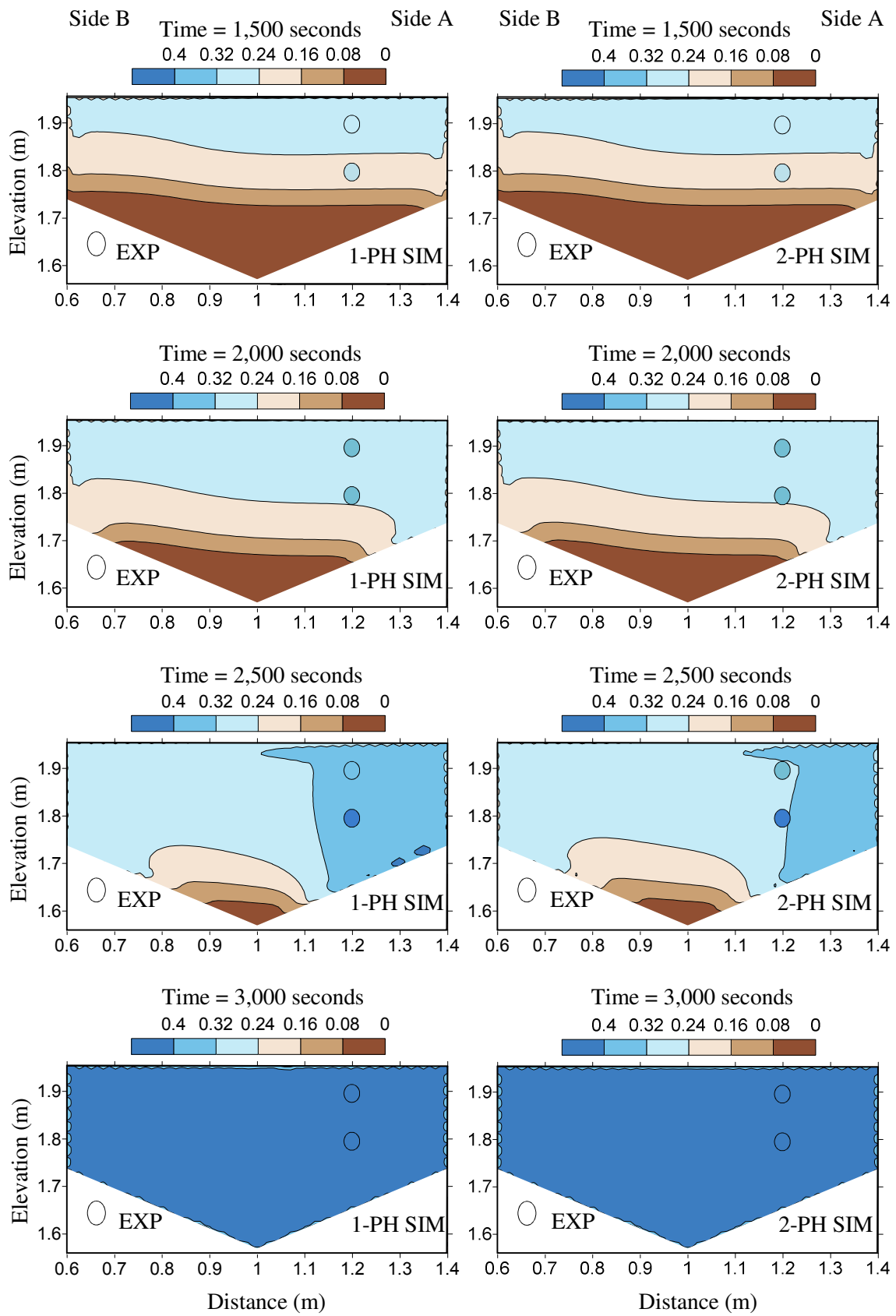


Figure 3.14 Moisture counter at cross section through PR3 (28° flume slope)

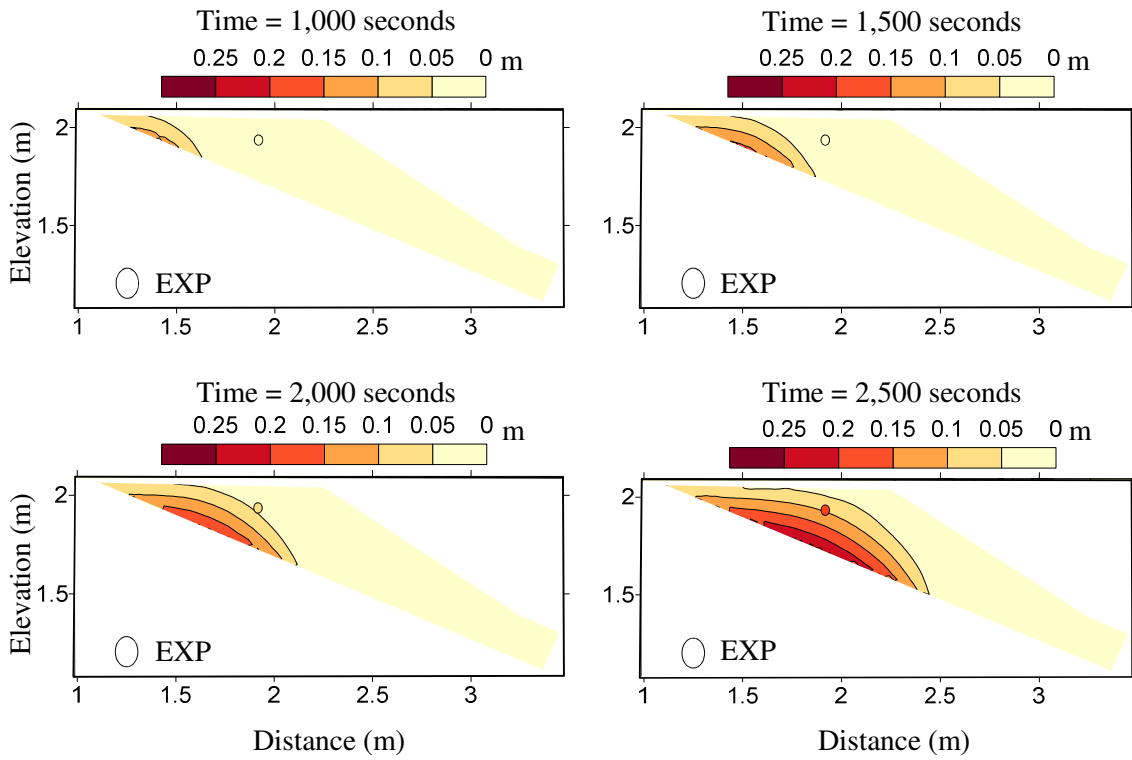


Figure 3.15 Air pressure head counter at longitudinal section through centre line (23° flume slope)

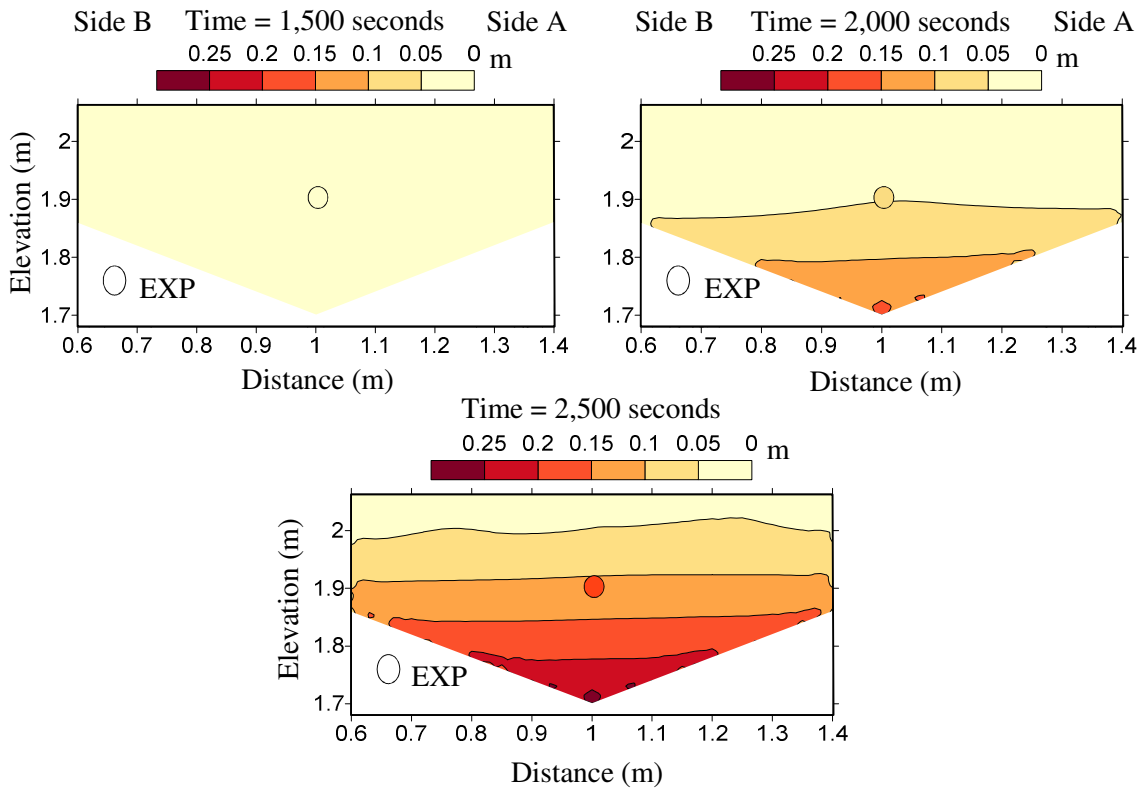


Figure 3.16 Air pressure head counter at cross section through PT1 (23° flume slope)

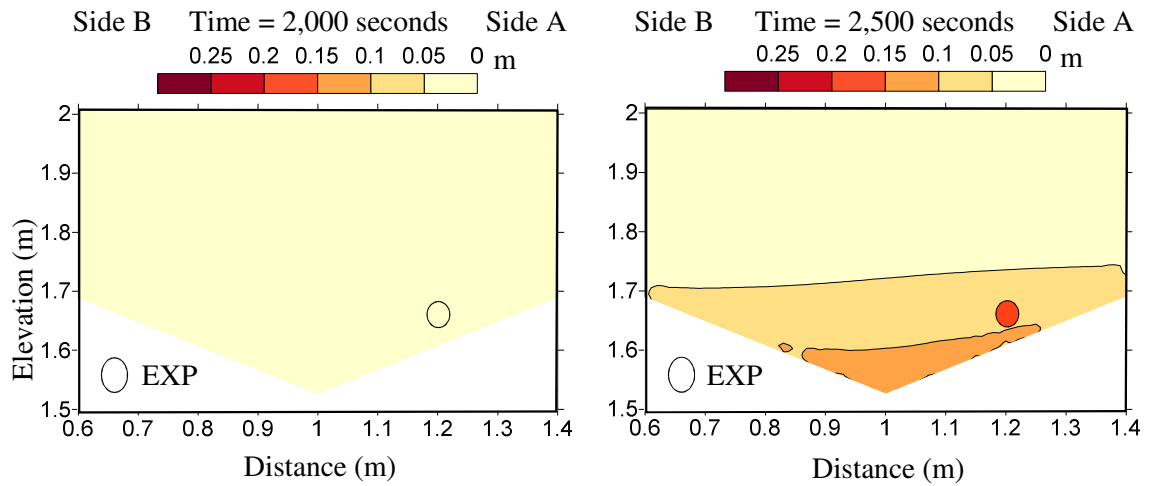


Figure 3.17 Air pressure head counter at cross section through PT2 (23° flume slope)

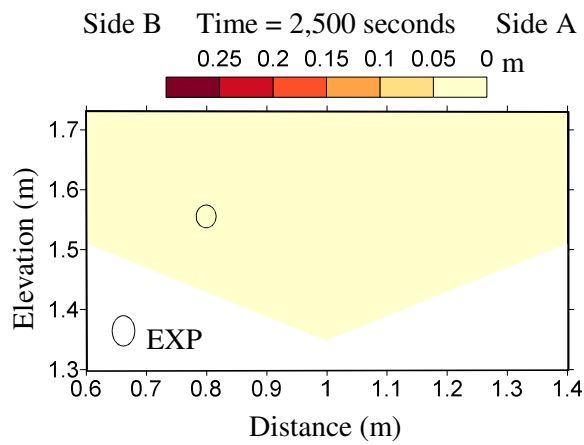


Figure 3.18 Air pressure head counter at cross section through PT3 (23° flume slope)

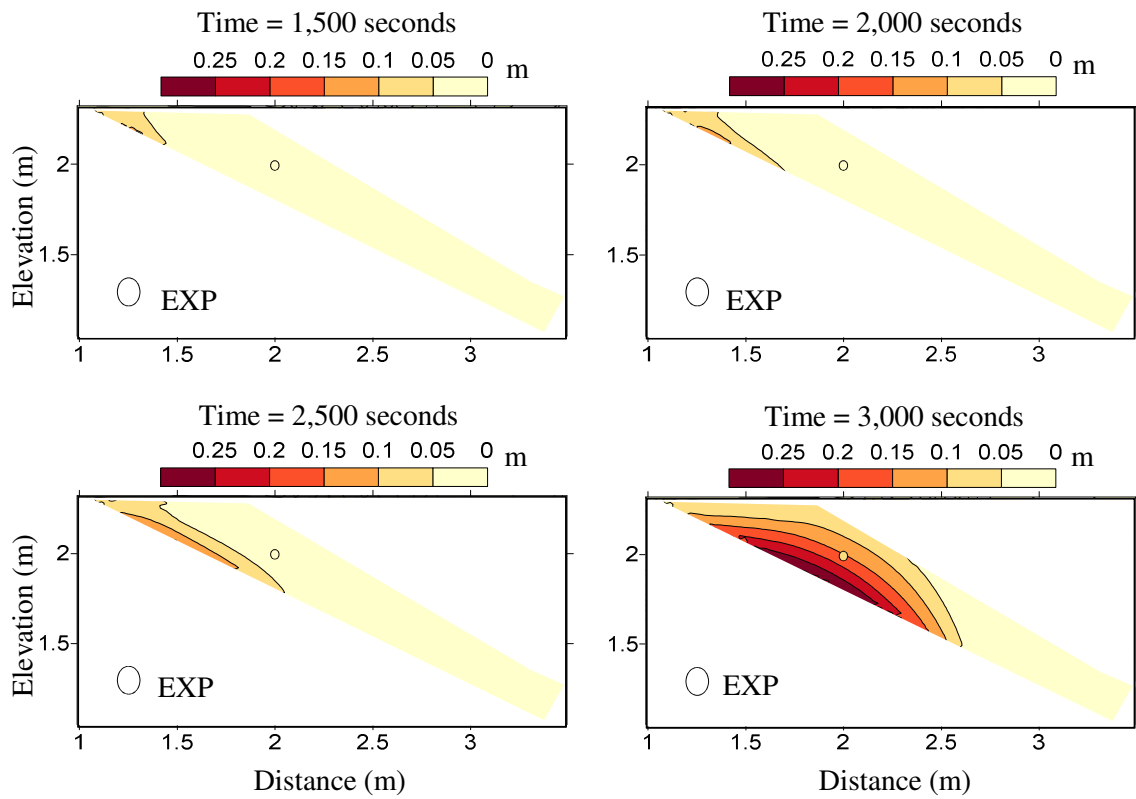


Figure 3.19 Air pressure head counter at longitudinal section through centre line ( $28^\circ$  flume slope)

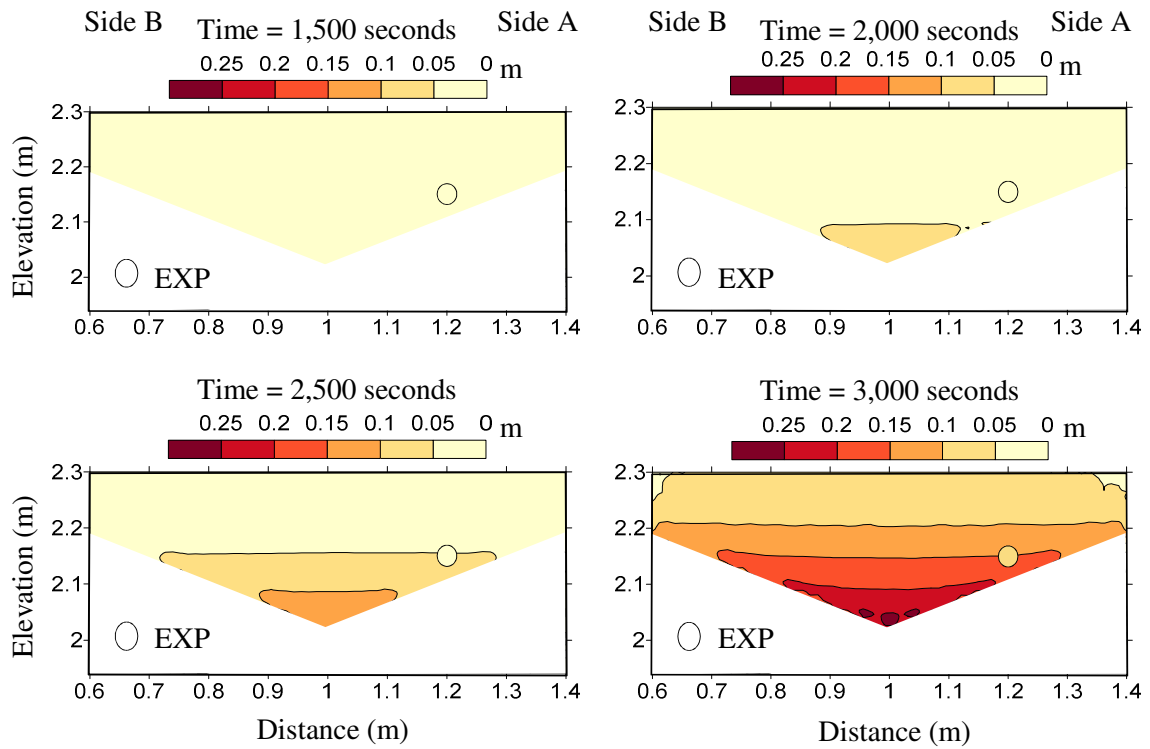


Figure 3.20 Air pressure head counter at cross section through PT1 ( $28^\circ$  flume slope)

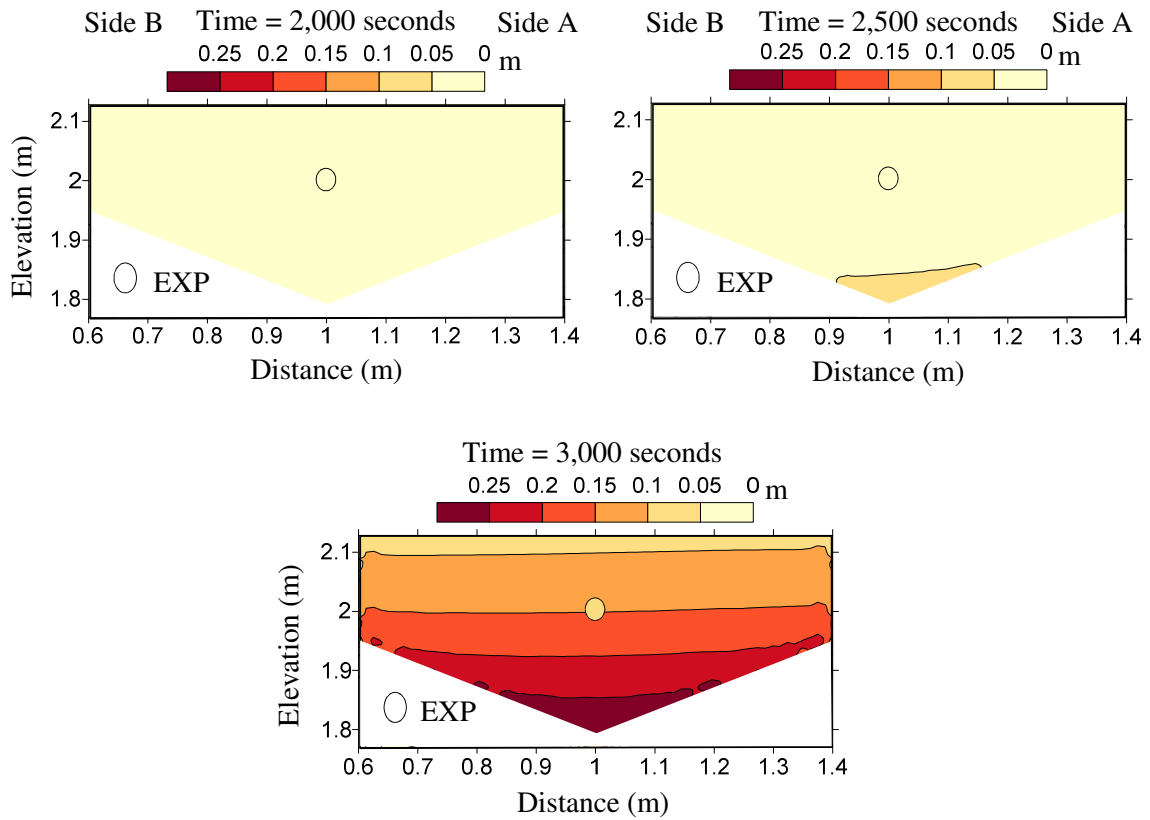


Figure 3.21 Air pressure head counter at cross section through PT2 (28° flume slope)

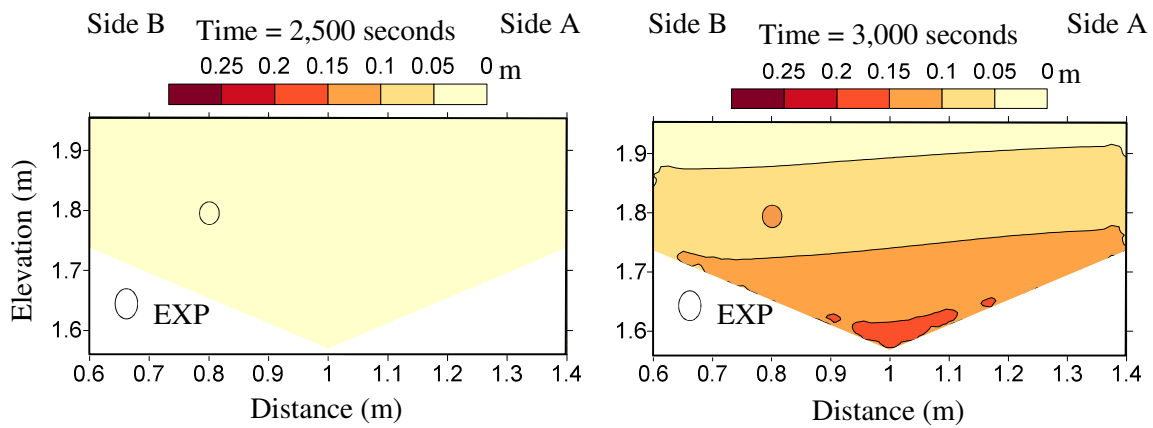


Figure 3.22 Air pressure head counter at cross section through PT3 (28° flume slope)

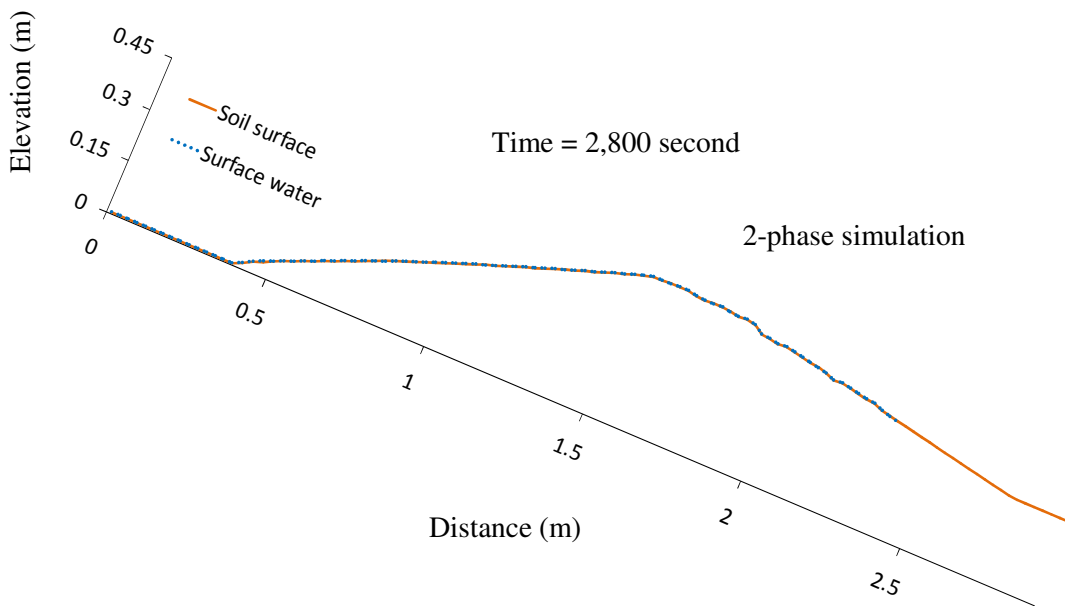
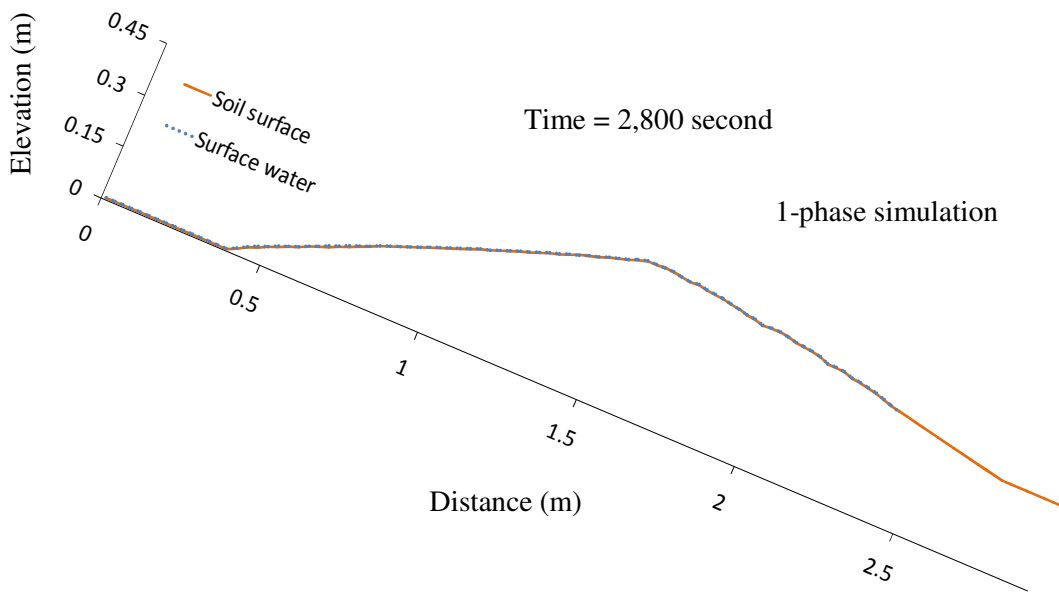


Figure 3.23 Surface water front on the soil surface at longitudinal section through centre line (23° flume slope)

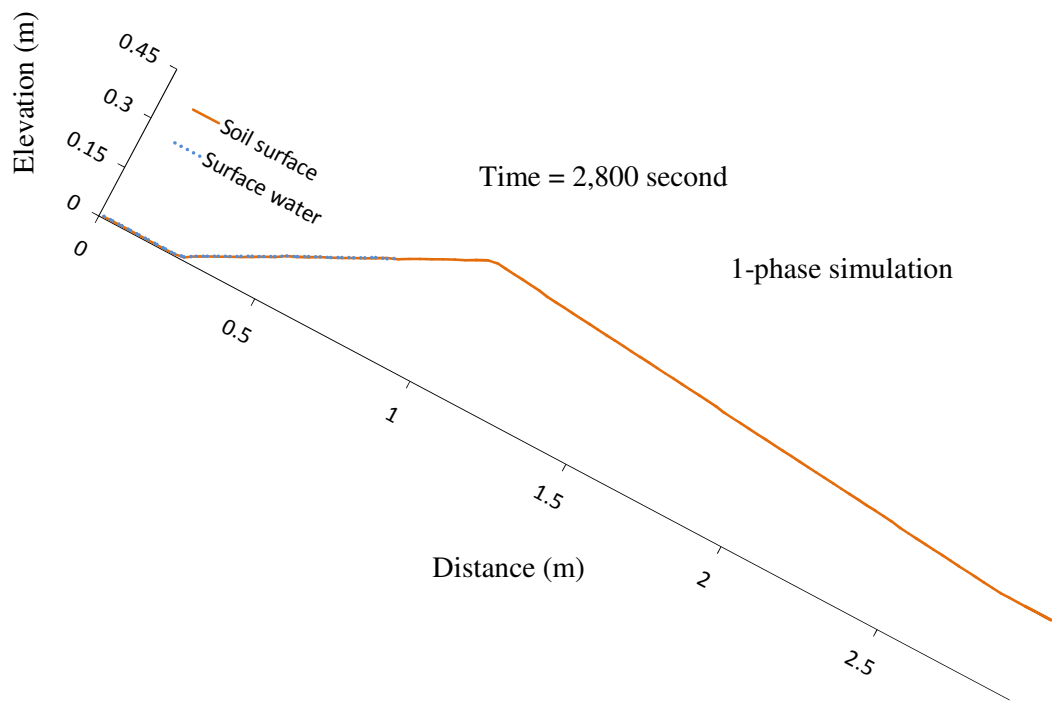
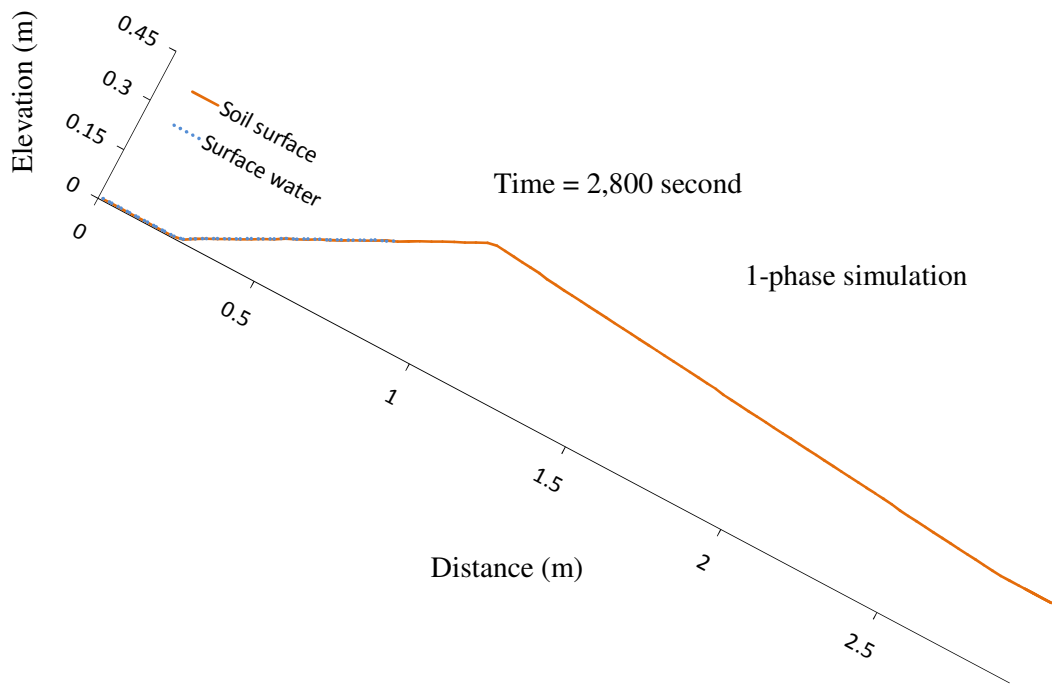


Figure 3.24 Surface water front on the soil surface at longitudinal section through centre line (28° flume slope)

Table 3.1 Surface water forefront propagated time to measuring scales (23° flume slope)

Scale	Distance from d/s face (m), parallel to flume slope	Water forefront reached time (sec)	Water forefront reached time (sec)	Water forefront reached time (sec)
		EXP	SIM-1PH	SIM-2PH
1	2.5	35	28	28
2	2.3	77	111	113
3	2.1	276	374	359
4	1.9	761	975	950
5	1.7	1369	1587	1548
6	1.5	1983	2192	2158

Table 3.2 Surface water forefront propagated time to measuring scales (28° flume slope)

Scale	Distance from d/s face (m), parallel to flume slope	Water forefront reached time (sec)	Water forefront reached time (sec)	Water forefront reached time (sec)
		EXP	SIM-1PH	SIM-2PH
1	2.6	102	94	92
2	2.45	497	436	422
3	2.3	2153	1832	1646
4	2.15	3184	2788	2788

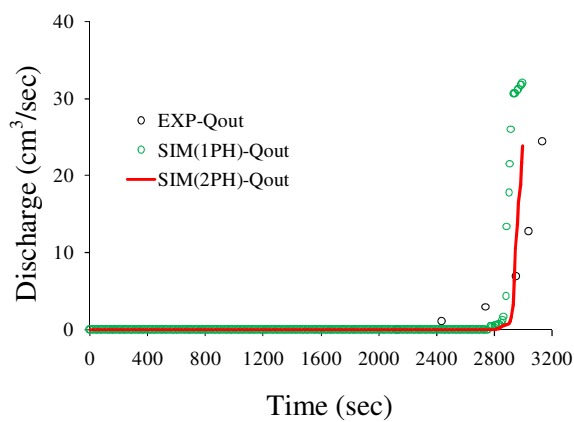


Figure 3.25 Seepage Outflow (23° flume slope)

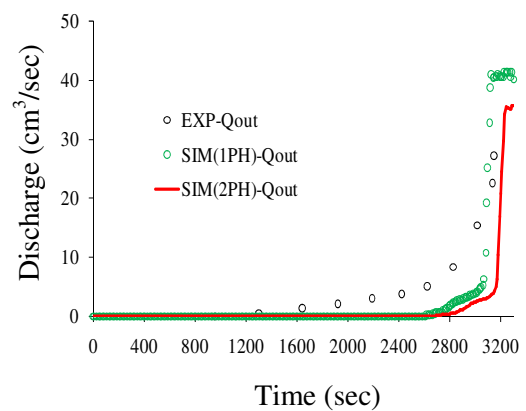
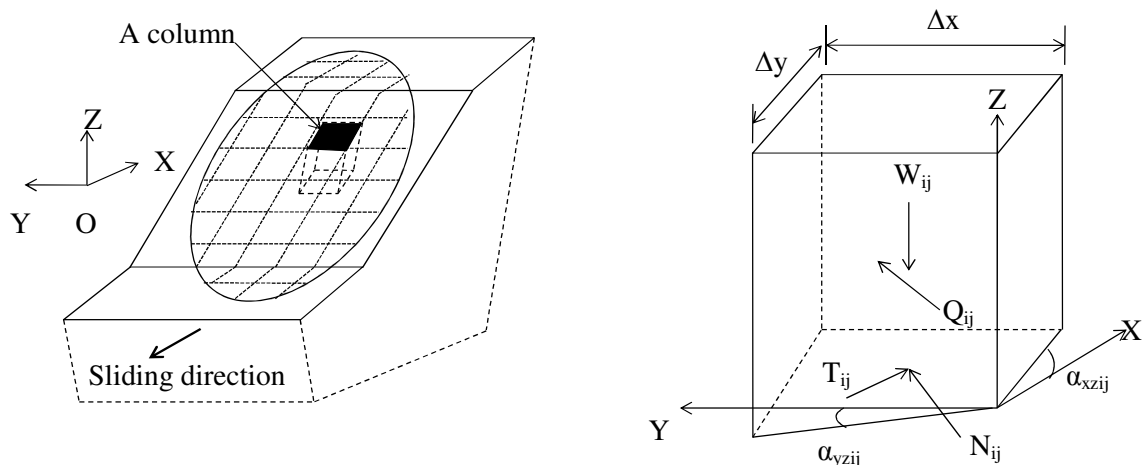


Figure 3.26 Seepage outflow (28° flume slope)

### 3.3 Slope stability analysis

The stability of a slope depends on its geometry, soil properties and the forces to which it is subjected to internally and externally. The numerous methods currently available for slope stability analysis provide a procedure for assigning a factor of safety to a given slip surface, but do not consider the problem of identifying the critical conditions. Limit equilibrium method of slices is widely used for slope stability analysis due to its simplicity and applicability. In the method of slices, the soil mass above the slip surface is divided into a number of vertical slices and the equilibrium of each of these slices is considered. The actual number of the slices depends on the slope geometry and soil profile. The limiting equilibrium consideration usually involves two steps; one for the calculation of the factor of safety and the other for locating the most critical slip surface which yields the minimal factor of safety. Methods by Bishop, Janbu, Spencer and Morgenstern and Price are now well known.

In this study Janbu's simplified method as well as extended Spencer method was incorporated into an effective minimization procedure based on dynamic programming by which the minimal factor of safety and the corresponding critical non circular slip surface were determined simultaneously. Janbu's simplified method only satisfies force equilibrium for the entire sliding mass and assumes resultant inter-slice forces horizontal where as extended Spencer method satisfies both the force and moment equilibrium and assumes resultant inter-slice forces are at some angle to the horizontal. Figure 3.27 shows the general slip surface and forces acting on a typical column.



(a) Sliding mass and vertically divided columns

(b) Forces acting on a the column ij

Figure 3.27 Three dimensional general slip surface and forces acting on a typical column

### 3.3.1 Janbu's simplified method

The factor of safety  $F_s$  for Janbu's simplified method is expressed by the following equation (Awal et al., 2009).

$$F_s = \frac{\sum_{i=1}^m \sum_{j=1}^n \left[ (c_e - u_{p_{ij}} \tan \phi) \Delta x \Delta y + (W_{ij} + P_{ij}) \tan \phi \right] / \left[ (1/J + \sin \alpha_{xzij} \tan \phi / F_s) \cos \alpha_{xzij} \right]}{\sum_{i=1}^m \sum_{j=1}^n (W_{ij} + P_{ij}) \tan \alpha_{xzij}} \quad (3.71)$$

where,  $\Delta x$  and  $\Delta y$  are discretized widths of the columns in  $x$  and  $y$  directions respectively;  $\alpha_{xz}$  and  $\alpha_{yz}$  are the inclination angles of the column base to the horizontal direction in the  $xz$  and  $yz$  planes respectively; and  $c_e$  and  $\phi$  are the Mohr-Coulomb strength parameters.  $J = (1 + \tan^2 \alpha_{xzij} + \tan^2 \alpha_{yzij})^{1/2}$ ;  $W_{ij} = \sum \theta_w(x, y, z, t) \gamma_w dx dy dz + \sum c_* \gamma_s dx dy dz$  (the weight of a column);  $P_{ij} = \sum \gamma_w h(x, y, t) dx dy$  (the vertical external force i.e., surface water weight, acting on the top of the column);  $u_{p_{ij}} = \text{Average} \sum \gamma_w h_w(x, y, z, t)$  (the pore water pressure at the base of the column) for  $h_w(x, y, z, t) > 0$ ;  $dx$ ,  $dy$  and  $dz$  are the size of cell used in seepage flow model,  $\gamma_w$  and  $\gamma_s$  are the unit weight of water and solids respectively,  $c_*$  is the volume concentration of the solids fraction in the body of slope model,  $\theta_w(x, y, z, t)$  and  $h_w(x, y, z, t)$  are the moisture content and pressure head in each cell and  $h(x, y, t)$  is the depth of surface water above the cell.

### 3.3.2 Extended Spencer method

Following equations of factor of safety for extended Spencer method have been used (Jiang and Yamagami, 2004).

$$F_f = \frac{\sum_{i=1}^m \sum_{j=1}^n \left[ (c_e - u_{p_{ij}} \tan \phi) \sec \alpha_{xzij} \Delta x \Delta y + (W_{ij} + P_{ij}) (\sec \alpha_{xzij} - \tan \delta \sin \alpha_{xzij}) \tan \phi \right] / m_\alpha + F_f \tan \delta \tan^2 \alpha_{xzij} / J}{\sum_{i=1}^m \sum_{j=1}^n (W_{ij} + P_{ij}) \tan \alpha_{xzij}} \quad (3.72)$$

$$F_m = \frac{\sum_{i=1}^m \sum_{j=1}^n D_{ij} \left[ (c_e - u_{p_{ij}} \tan \phi) \sec \alpha_{xzij} \Delta x \Delta y \sin(\theta_{ij} + \delta) / \cos \delta + (W_{ij} + P_{ij}) \right]}{\sum_{i=1}^m \sum_{j=1}^n (W_{ij} + P_{ij}) D_{ij} \cos \theta_{ij}} \left\{ \tan \phi \tan(\theta_{ij} + \alpha_{xzij}) + F_m \sec \alpha_{xzij} / J \right\} / m_\alpha \quad (3.73)$$

where,  $F_f$  and  $F_m$  are the factor of safety with respect to force equilibrium and moment equilibrium respectively;  $m_\alpha = (1 + \tan \delta \tan \alpha_{xzij}) / J + (\sin \alpha_{xzij} - \tan \delta \cos \alpha_{xzij}) \tan \phi / F$  with  $F = F_f$  for Equation 3.72 and  $F_m$  for Equation 3.73;  $\delta$  is the inclination of interslice forces to the horizontal;  $D_{ij}$  is the distance from the axis of rotation to the base centre of a column in  $xz$  plane; and  $\theta_{ij}$  is the angle between the horizontal direction and the  $D$  direction in the  $xz$  plane.

$F_f$  and  $F_m$  can separately be computed from the Equations 3.72 and 3.73 for several appropriately given values of  $\delta$ . Then, two curves showing the relationships of  $F_f - \delta$  and  $F_m - \delta$  can be plotted so that the intersection of these two curves leads to a required  $\delta_o$  value and corresponding factor of safety  $F_s$ , satisfying both force and moment equilibrium.

### 3.3.3 Dynamic programming search procedure

Dynamic programming (DP), developed by Richard Bellman in the early 1950s, is a numerical algorithm in mathematical programming for solving sequential multistage optimization problems. The major aspect of DP is to construct a recurrence relation based on principle of optimality. The optimal solution and the corresponding optimal trajectory can be evaluated by solving the recurrence relation. A search scheme for determination of critical 3D surface was developed by incorporating the Janbu's method (Equation 3.71) into dynamic programming (Yamagami and Jiang, 1997).

Equation 3.71 can be represented by the following expression.

$$F_s = \frac{\sum_{i=1}^m R_i}{\sum_{i=1}^m T_i} \quad (3.74)$$

where,

$$R_i = \sum_{j=1}^n \frac{(c - u_{ij} \tan \phi) \Delta x \Delta y + (W_{ij} + P_{ij}) \tan \phi}{\cos \alpha_{xzij} (1/J + \sin \alpha_{xzij} \tan \phi / F_s)} \quad (3.75)$$

$$T_i = \sum_{j=1}^n \tan \alpha_{xzij} (W_{ij} + P_{ij}) \quad (3.76)$$

In order to minimize the functional  $F_s$ , defined in Equation 3.74, the auxiliary functional  $G$  is defined as (Baker, 1980).

$$G = \sum_{i=1}^m [R_i - F_s T_i] = \sum_{i=1}^m DG_i \quad (3.77)$$

When applying dynamic programming, minimization of  $G$  is carried out over all admissible slip surfaces:

$$G_m = \min G = \min \sum_{i=1}^m DG_i \quad (3.78)$$

Application of dynamic programming to a particular problem requires a stage-state system (Baker, 1980). Figure 3.28 illustrates such a stage-state system for a 3D slope (Yamagami and Jiang, 1997). In the present case, 'stages' are vertical planes perpendicular to the sliding direction and a state in a stage is represented by a curve in the stage plane. One state curve for each stage is shown in Figure 3.29. However a large number of state curves in each stage plane are necessary to search for a smooth 3D critical slip surface. The state curves in each stage plane are produced by use of Random Number Generation techniques.

To obtain a sufficiently accurate solution for a general slope, a few hundred state curves usually need to be produced in each stage plane prior to the dynamic programming search. If a state curve  $k$  in a stage  $i$  and a state curve  $kk$  in the stage  $i+1$  are selected, as shown in Figure 3.28, the shaded concave segment sandwiched between these two state curves constitutes a part of a potential 3D slip surface. Referring to Figure 3.28, Figure 3.29 can be drawn in which the earth mass between the two adjacent stage planes  $i$  and  $i+1$  has been discretized into  $(n)$  vertical columns by two groups of  $(n+1)$  vertical dividing lines located respectively in stage  $i$  and stage  $i+1$ . Since the state curves  $k$  and  $kk$  were chosen from those produced by the random number generation technique, the location of the  $(n)$  columns are determined.

Consequently,  $R_i$  and  $T_i$  in Equation 3.77 can be calculated, and thus Equation 3.77 may be written as

$$G = \sum_{i=1}^m [R_i - F_s T_i] = \sum_{i=1}^m DG_i = \sum_{i=1}^m DG_i(k, kk) \quad (3.79)$$

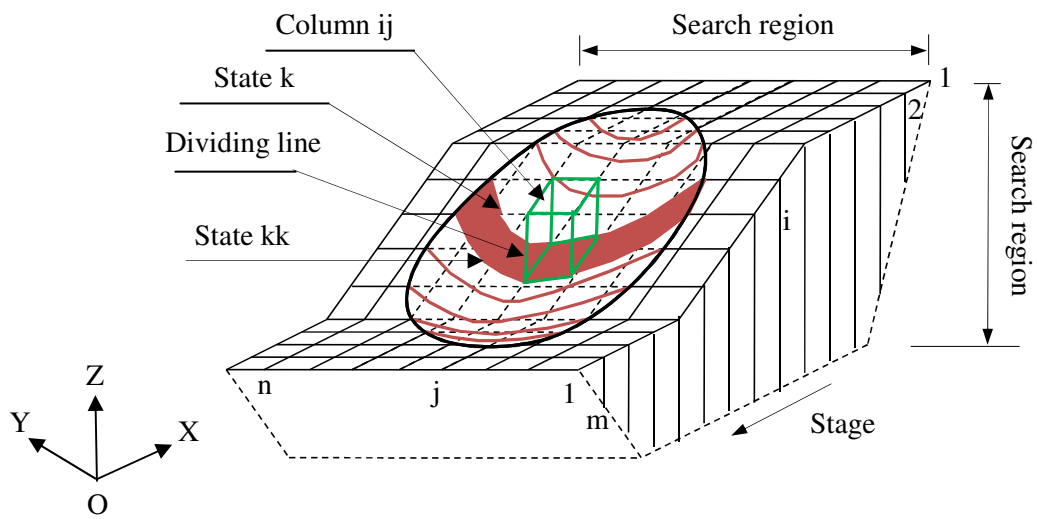


Figure 3.28 A stage-state system and dividing scheme for a 3D slope

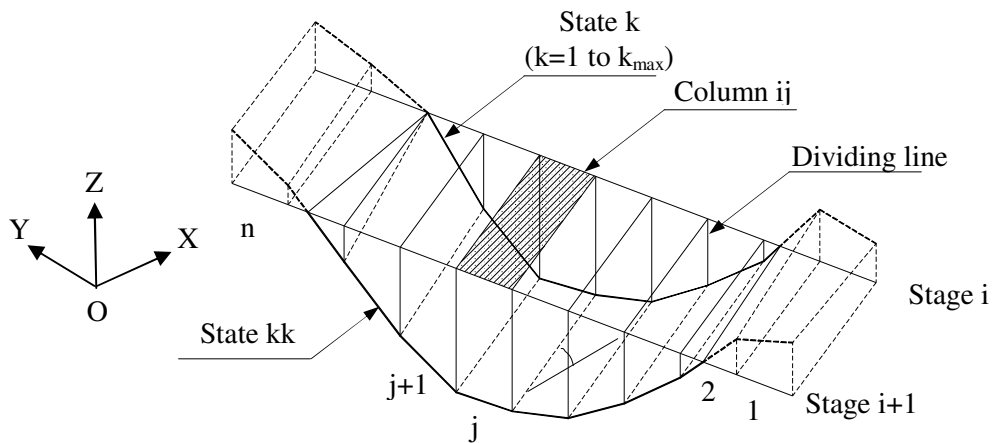


Figure 3.29 Columns between two adjacent stages  $i$  and  $i+1$

in which  $DG_i(k, kk) = R_i - F_s T_i$  is referred to as the return function in dynamic programming. The function  $DG_i(k, kk)$  represents a change in  $G$  between two state curves  $k$  and  $kk$  located in two adjacent stage planes  $i$  and  $i+1$ . If  $H_i(k)$ , optimal value function in dynamic programming, is the minimum value of  $G$  from stage 1 to the state curve  $k$  in stage  $i$  (Figure 3.28), then the minimum  $G$  value from stage 1 to state curve  $kk$  in stage  $i+1$  is given by Equation 3.80. According to Bellman's principle of optimality, Equation 3.80 is the recurrence relation in dynamic programming for the present situation.

$$H_{i+1}(kk) = \min [H_i(k) + DG_i(k, kk)], \quad i = 1 \sim m, k = 1 \sim S_{\max}, kk = 1 \sim S_{\max} \quad (3.80)$$

The boundary conditions are

$$H_1(k) = 0, \quad k = 1 \sim S_{\max} \quad (3.81)$$

$$G_m = \min G = \min [H_{n+1}(kk)], \quad kk = 1 \sim S_{\max} \quad (3.82)$$

Difference between the value of  $F_s$  calculated by Equation 3.74 after this procedure and initially assumed value of  $F_s$  should be within tolerance, therefore, iteration is required to obtain exact value of  $F_s$  along the slip surface.

The search scheme by Yamagami and Jiang (1997) can also be coupled with Equations 3.72 and 3.73 separately to determine minimum values for  $F_f$  and  $F_m$  and the computation procedure is as follows.

- i) Several appropriate values of  $\delta$  are specified first.
- ii) For each  $\delta$  value, the search scheme by Yamagami and Jiang (1997) is applied to Equation 3.72 to get minimum value for  $F_f$ .
- iii) By utilizing the above mentioned search scheme in Equation 3.73, minimum value for  $F_m$  can also be obtained using the assumed  $\delta$  values.
- iv) Two curves showing the relationships of  $F_f - \delta$  and  $F_m - \delta$  can be plotted so that the intersection of these two curves leads to a required value of  $\delta = \delta_0$ .
- v) Using the value  $\delta_0$  into equations 3.72 or 3.73 the critical slip surface and the corresponding factor of safety  $F_s$  can be obtained by performing the proposed search procedure again.

### 3.3.4 Results and discussions

Space steps of 10cm in horizontal x and y directions with time step of 10 second was used in slope stability model. Two experimental cases were considered out at flume slopes at 23° and 28° for the validation of model. In case of 23° flume slope two experiments were carried out. In experiment D the failure of the model slope was observed at 2,779 seconds and in experiment E at 2830 second. In case of 28° flume slope, the model slope was failed at 3286 seconds.

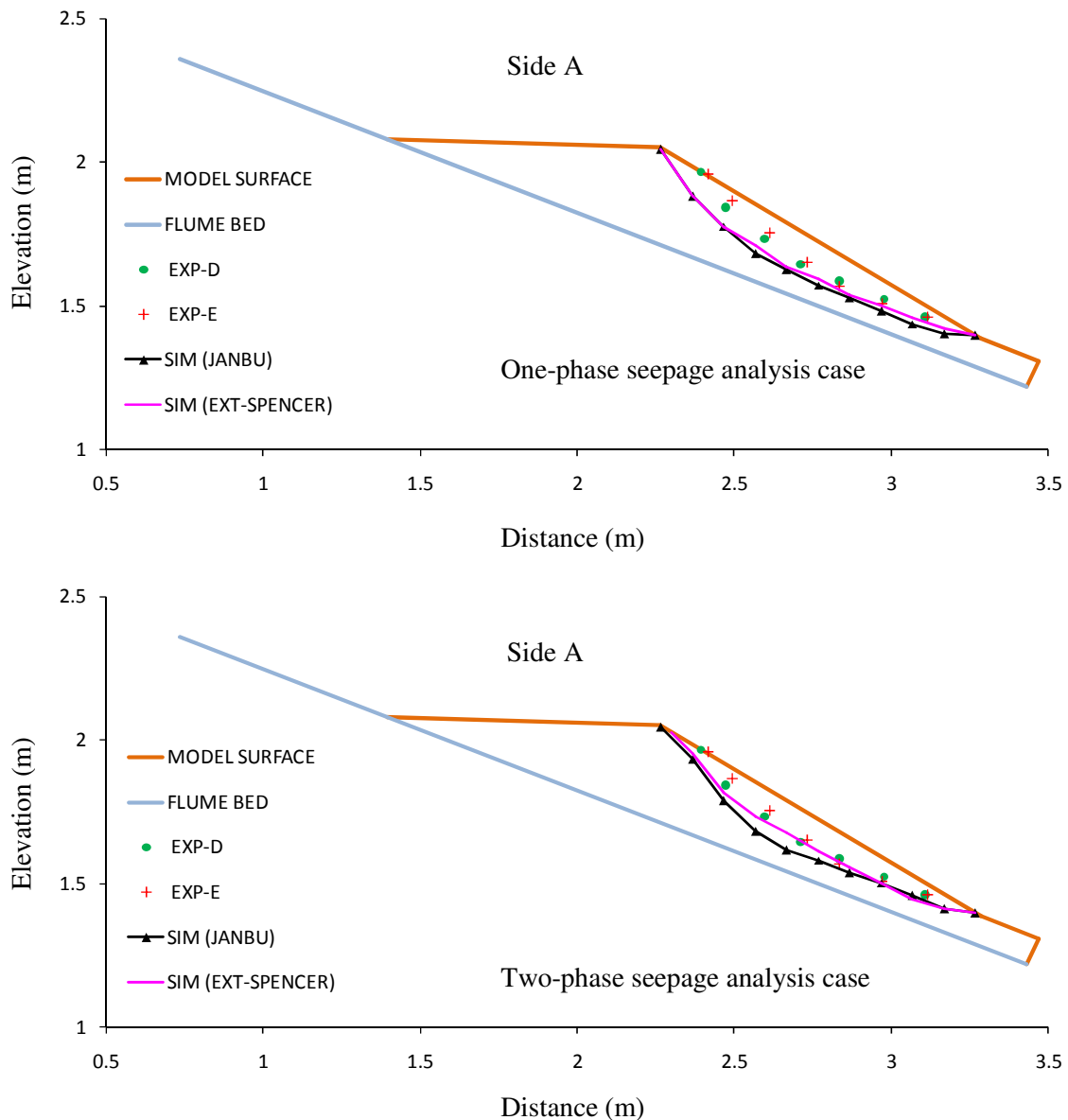


Figure 3.30 Comparison of longitudinal profiles of experimental and simulated failure surfaces in side A (23° flume slope)

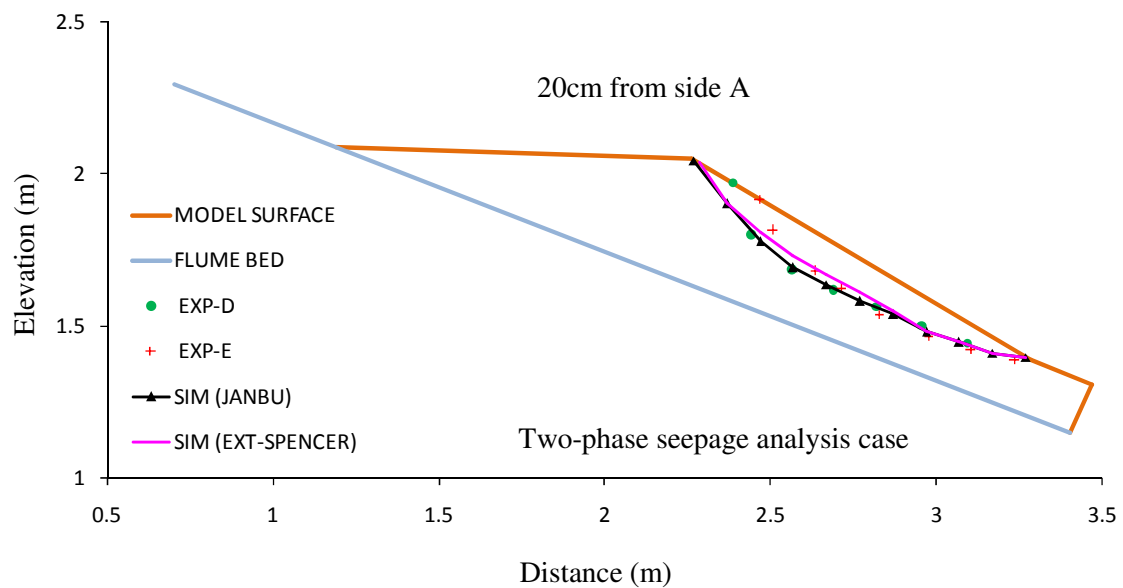
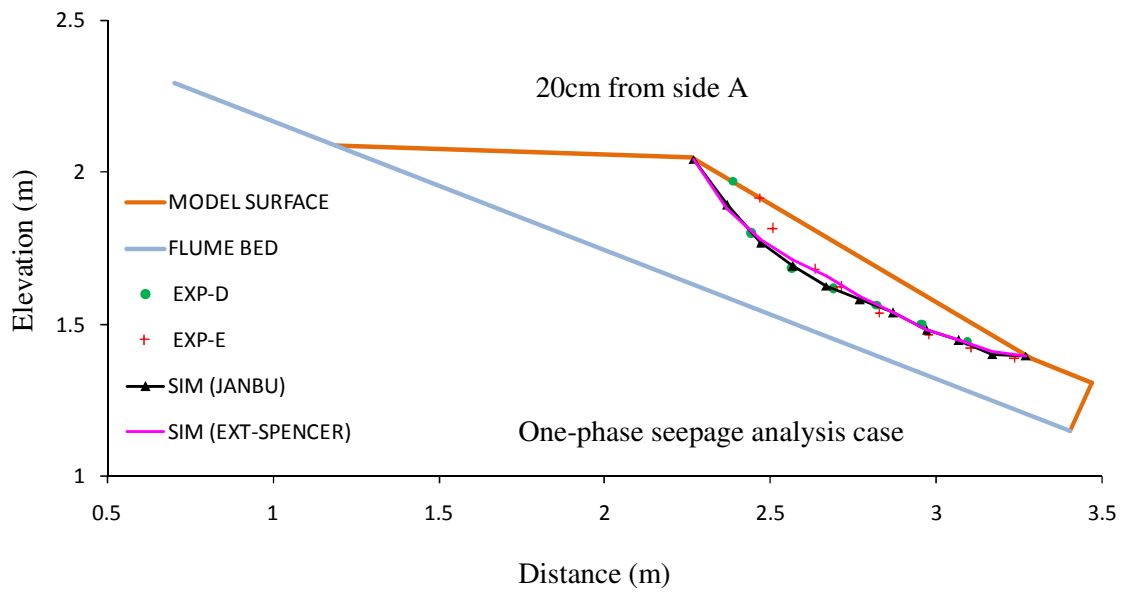


Figure 3.31 Comparison of longitudinal profiles of experimental and simulated failure surfaces at 20cm from side A ( $23^\circ$  flume slope)

The time of failure of the model slope and the corresponding factor of safety calculated by different methods in different cases is summarized in Table 3.3 and 3.4. Since there was higher rainfall intensity in experiment than the observed average values in  $23^\circ$  flume slope case and that of lesser rainfall intensity in  $28^\circ$  flume slope case, the failure time of model slope is found to be delayed in simulation than in experiment in case of  $23^\circ$  flume slope in average (Table 3.3).

Similarly, the failure time of model slope is found to be faster in simulation than in experiment in case of 28° flume slope (Table 3.4).

Since the rainfall intensity was more intense towards side A than B (Figure 2.13 in section 2.4), the concentration of observed sliding slope was also towards side A rather than B in experiments as well as simulations. Figures 3.30 to 3.39 show the comparison of longitudinal

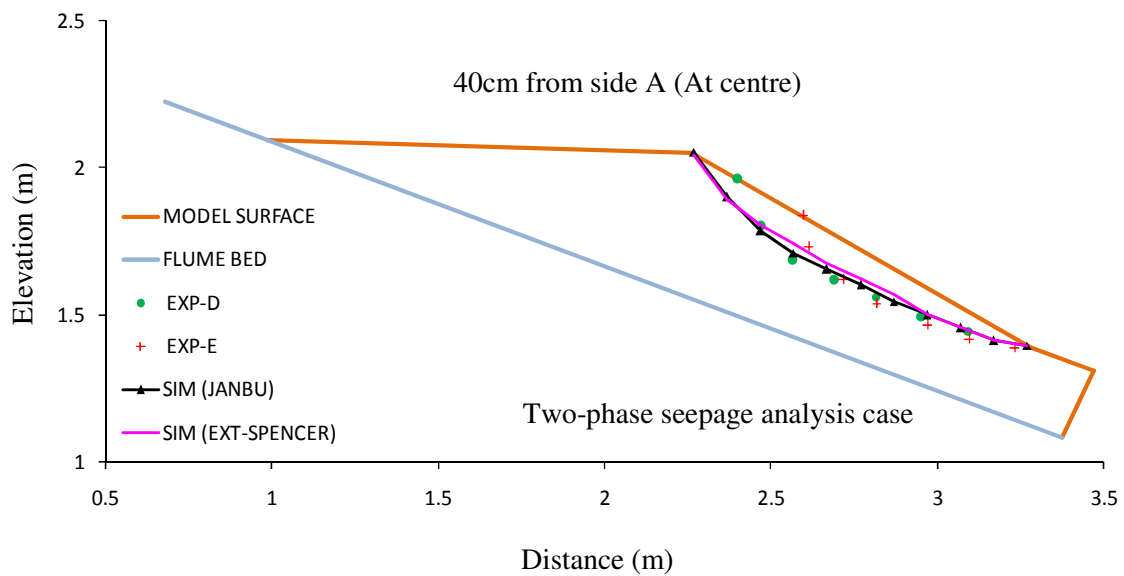
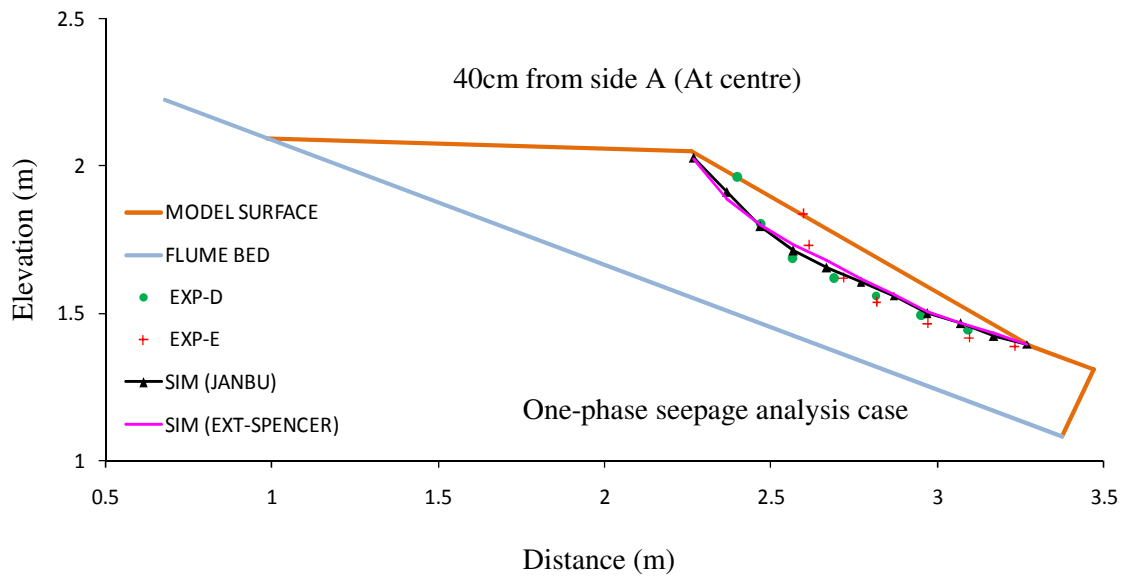


Figure 3.32 Comparison of longitudinal profiles of experimental and simulated failure surfaces at 40cm from side A (23° flume slope)

profiles of experimental and simulated failure surfaces. The comparison shows that the simulated and experimental failure surfaces as well as the corresponding time of failure are matching well. Figures 3.40 and 3.43 show the 3D view of the failure surface observed in experiments. 3D view of the failure surface calculated by Janbu's simplified method considering one-phase seepage analysis and extended Spencer method considering two-phase

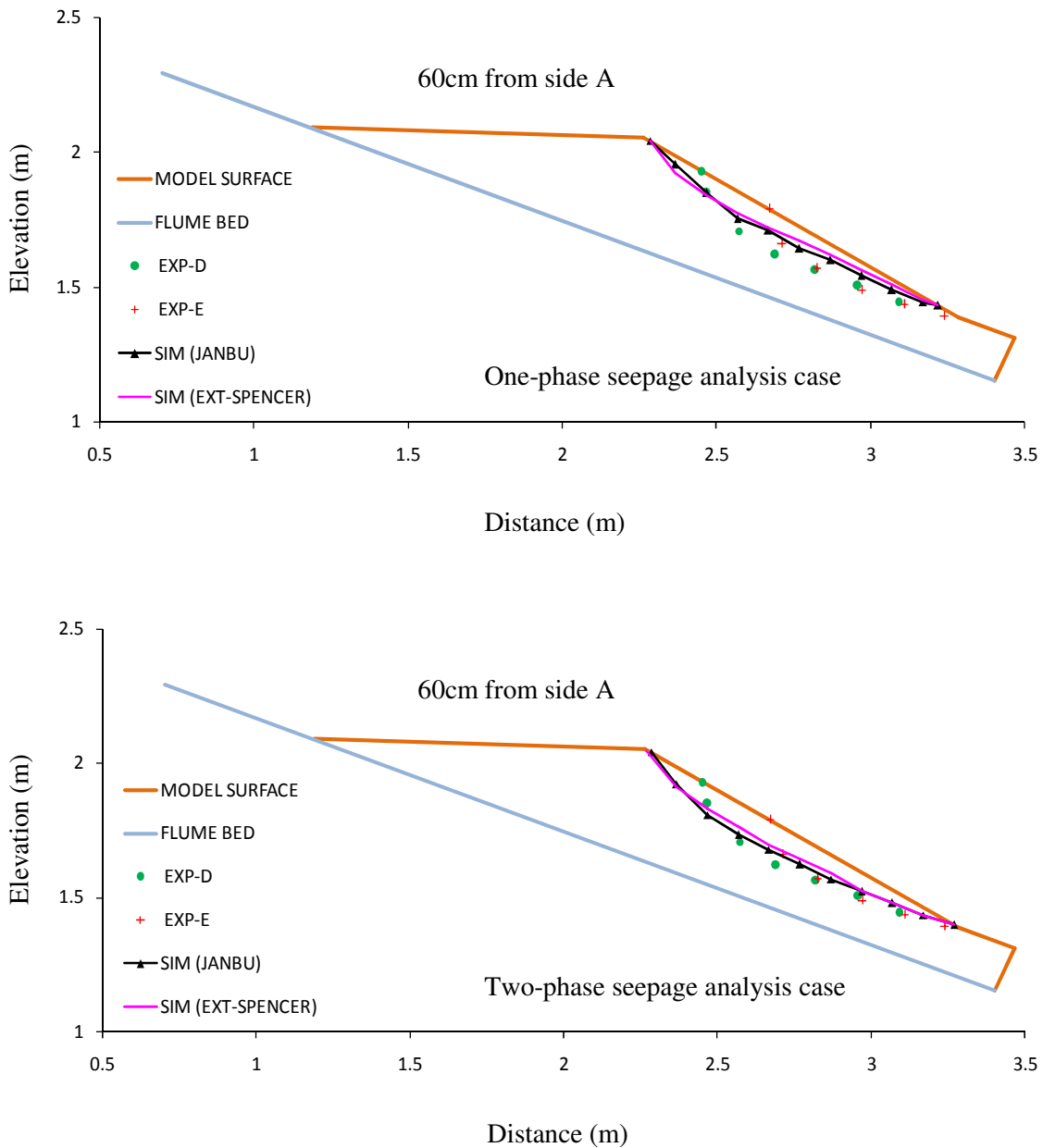


Figure 3.33 Comparison of longitudinal profiles of experimental and simulated failure surfaces at 60cm from side A (23° flume slope)

seepage analysis are respectively shown in Figures 3.41 and 3.42 in case of 23° flume slope.

3D view of the failure surface calculated by Janbu's simplified method considering one-phase seepage analysis and extended Spencer method considering two-phase seepage analysis are respectively shown in Figures 3.44 and 3.45 in case of 28° flume slope.

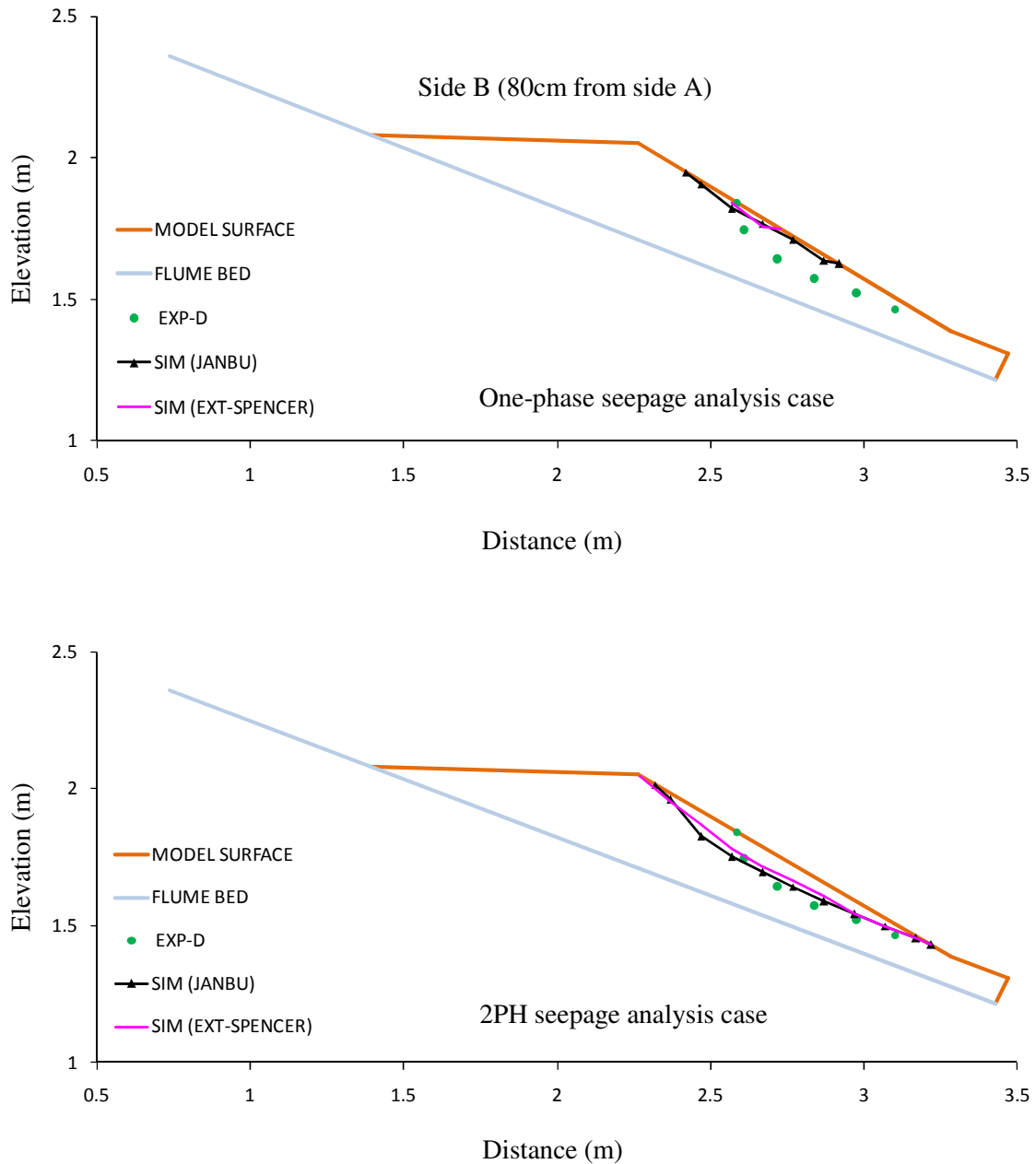


Figure 3.34 Comparison of longitudinal profiles of experimental and simulated failure surfaces in side B (23° flume slope)

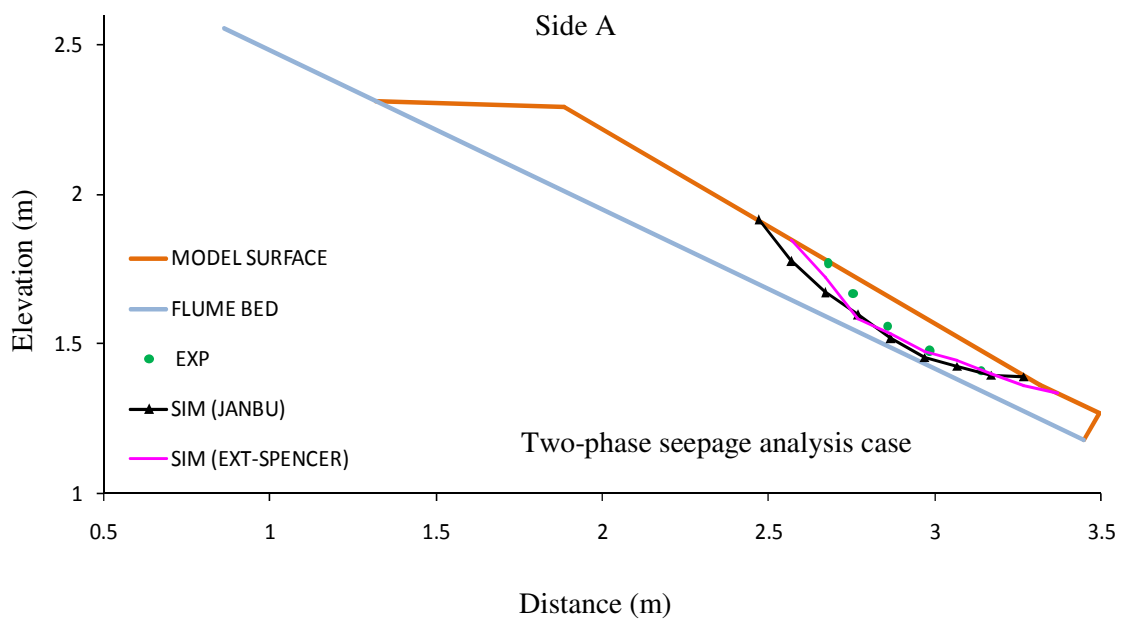
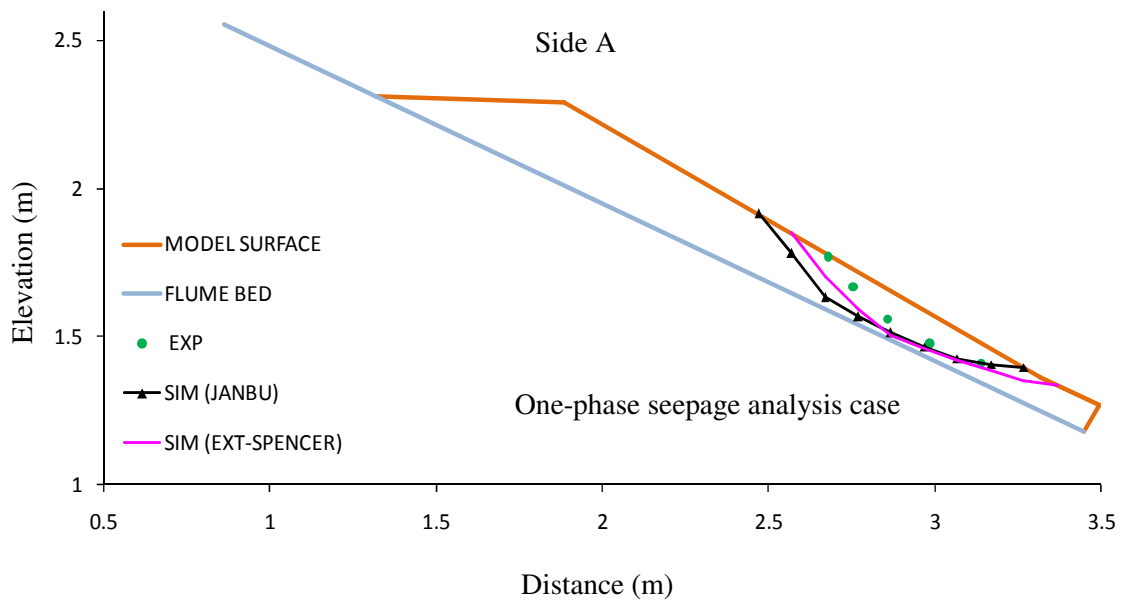


Figure 3.35 Comparison of longitudinal profiles of experimental and simulated failure surfaces in side A (28° flume slope)

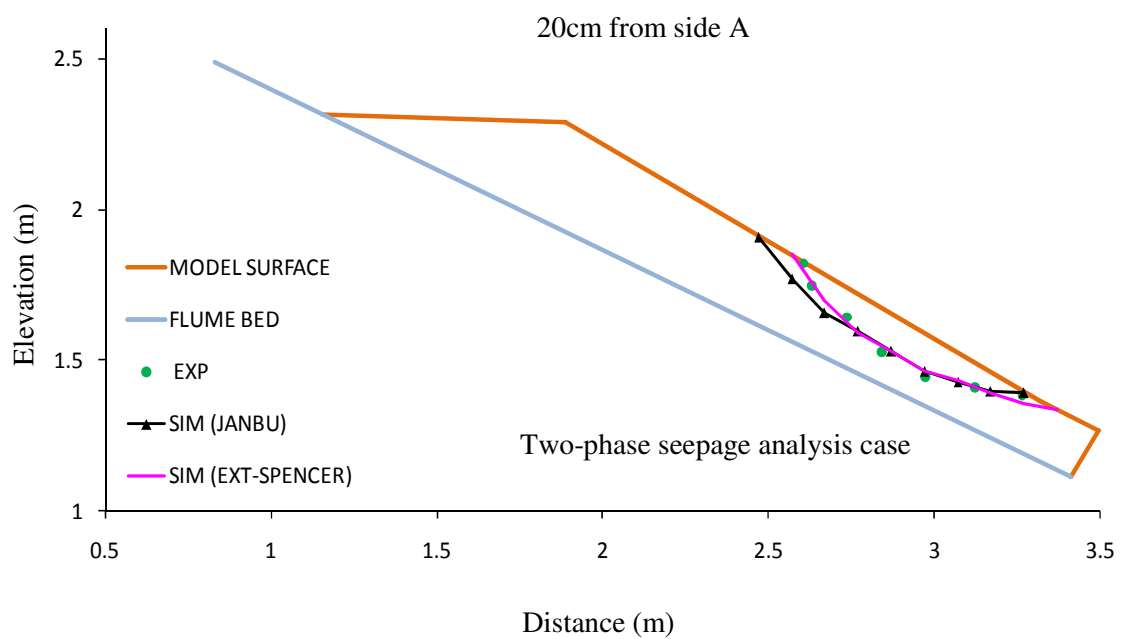
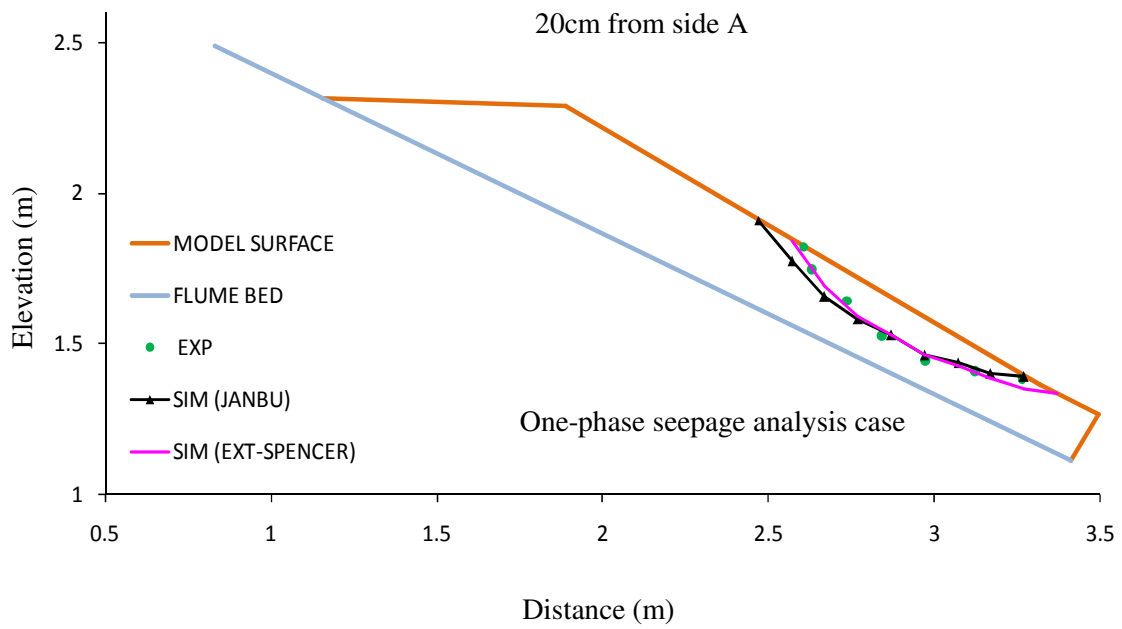


Figure 3.36 Comparison of longitudinal profiles of experimental and simulated failure surfaces at 20cm from side A (28° flume slope)

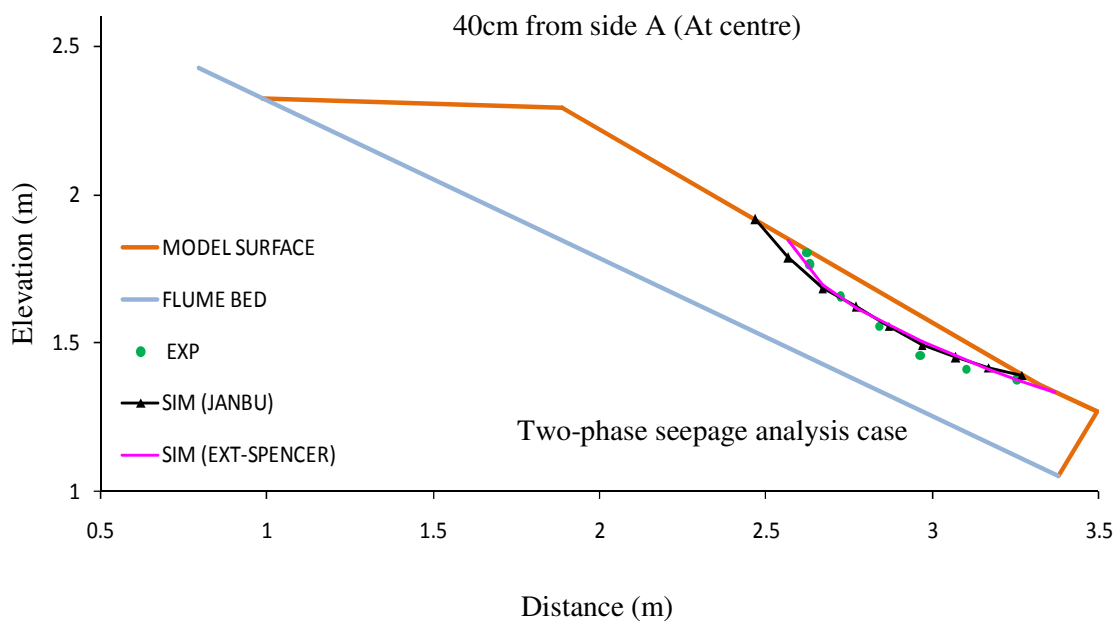
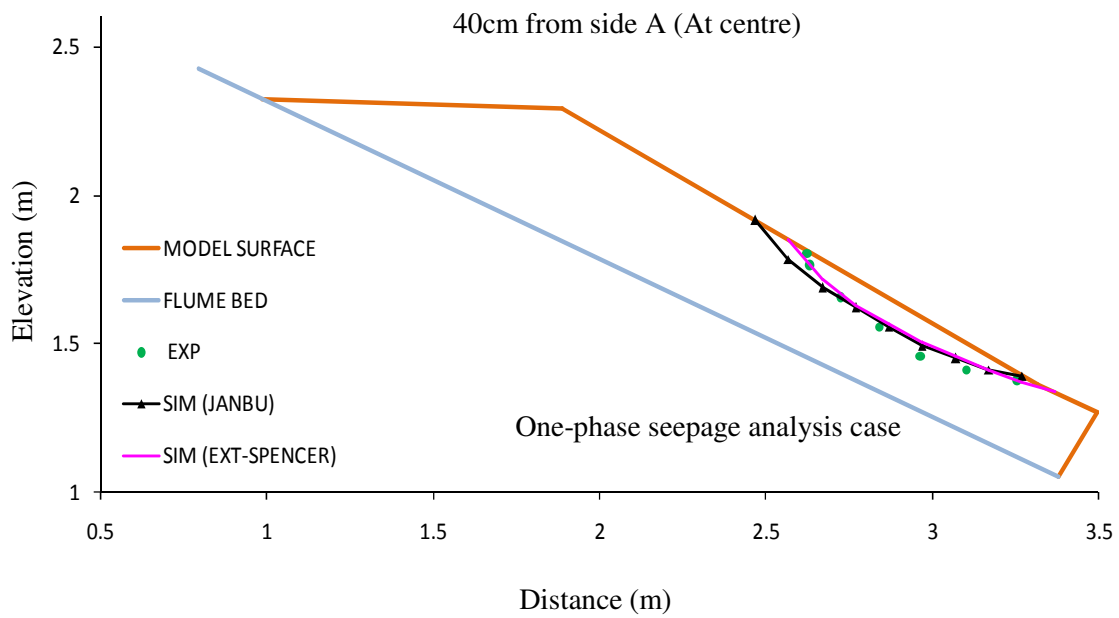


Figure 3.37 Comparison of longitudinal profiles of experimental and simulated failure surfaces at 40cm from side A ( $28^\circ$  flume slope)

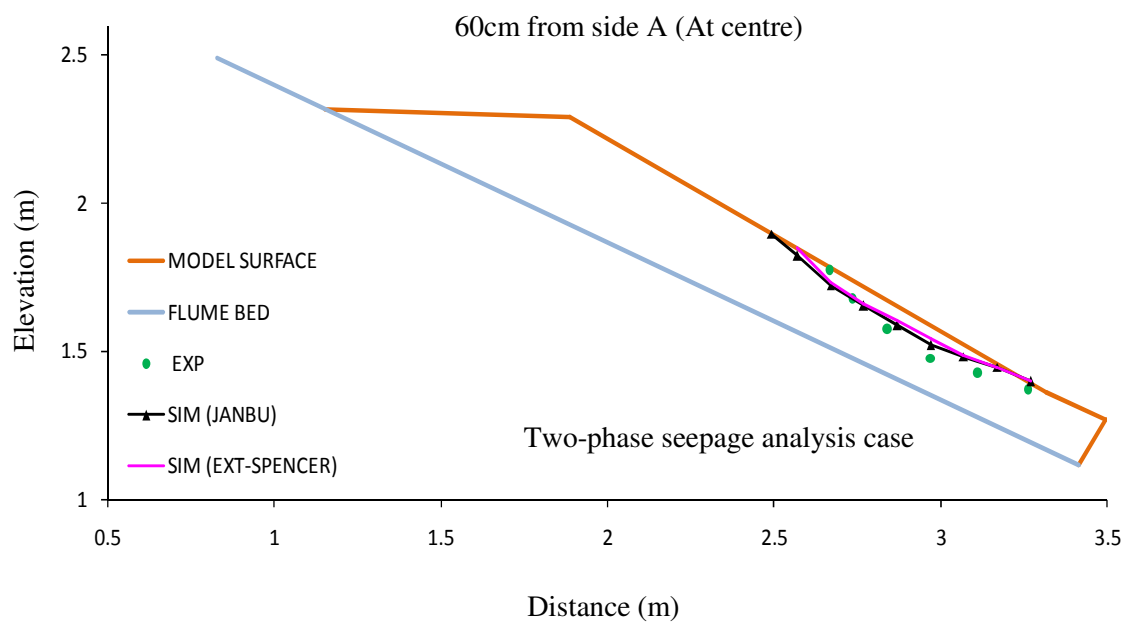
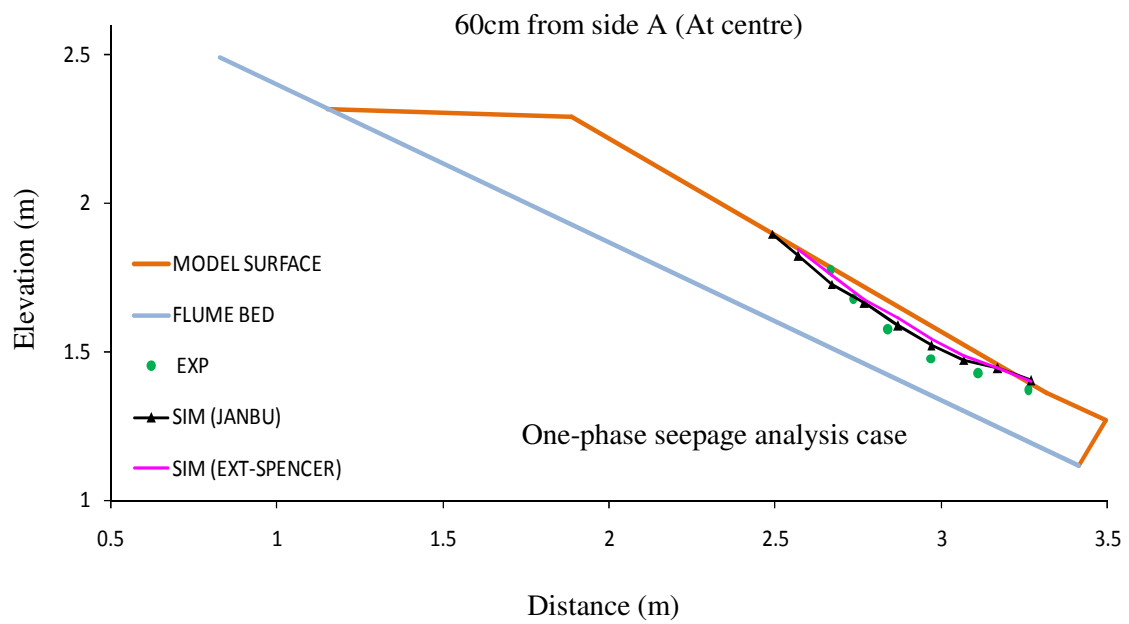


Figure 3.38 Comparison of longitudinal profiles of experimental and simulated failure surfaces at 60cm from side A ( $28^\circ$  flume slope)

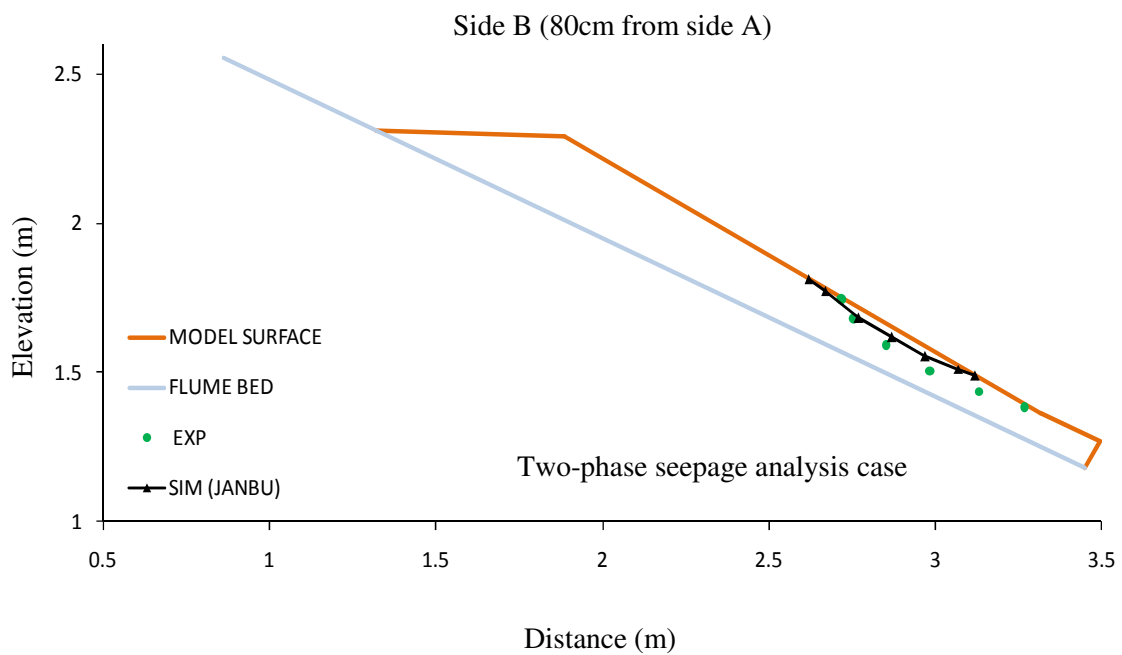
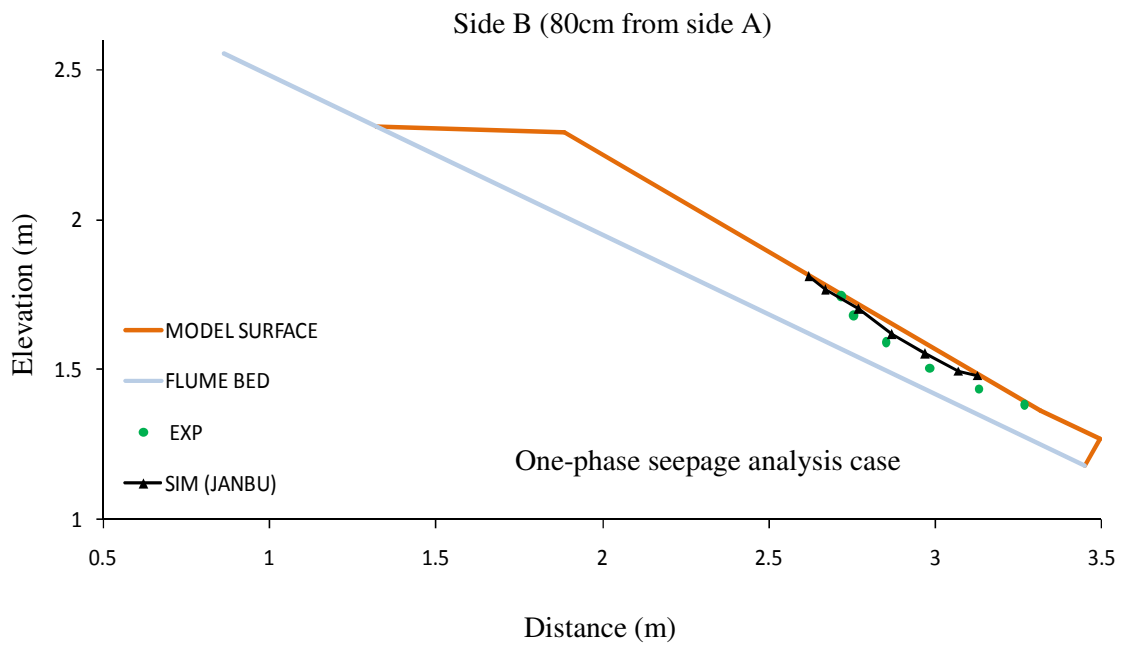


Figure 3.39 Comparison of longitudinal profiles of experimental and simulated failure surfaces in side B (28° flume slope)

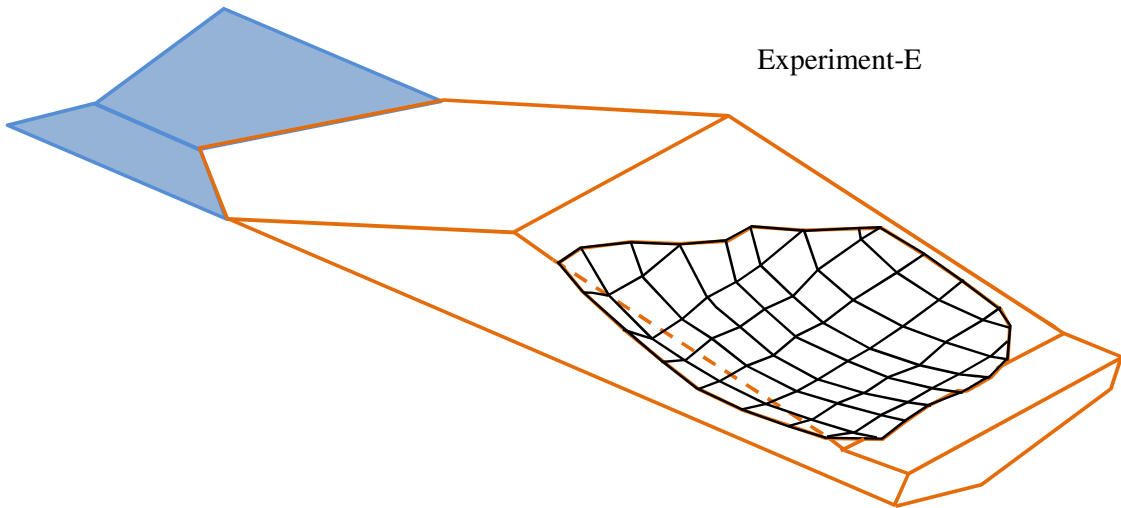
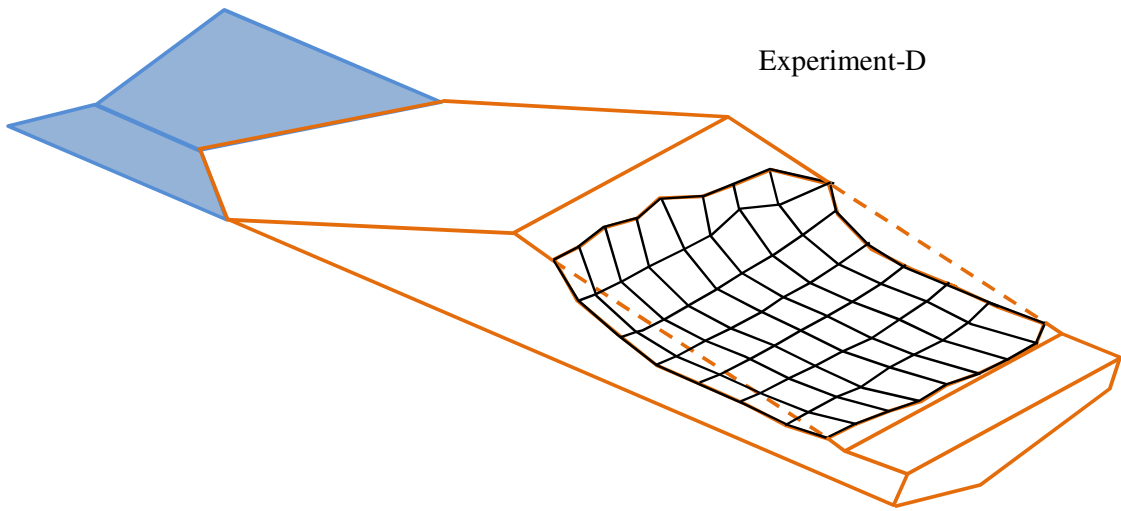


Figure 3.40 3D view of experimentally observed failure surfaces (23° flume slope)

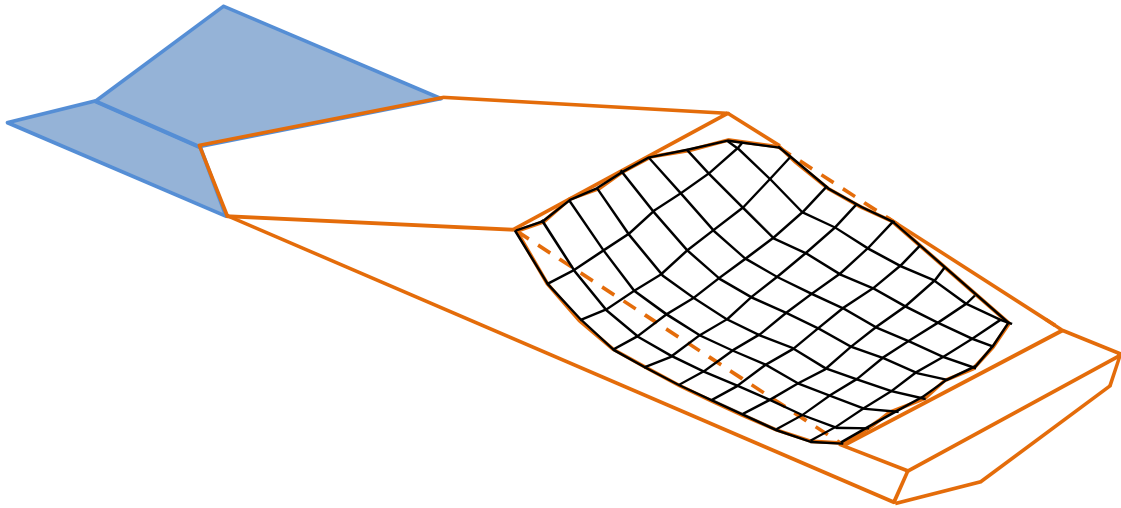


Figure 3.41 3D view of simulated failure surface using Janbu's simplified method, one-phase seepage analysis case (23° flume slope)

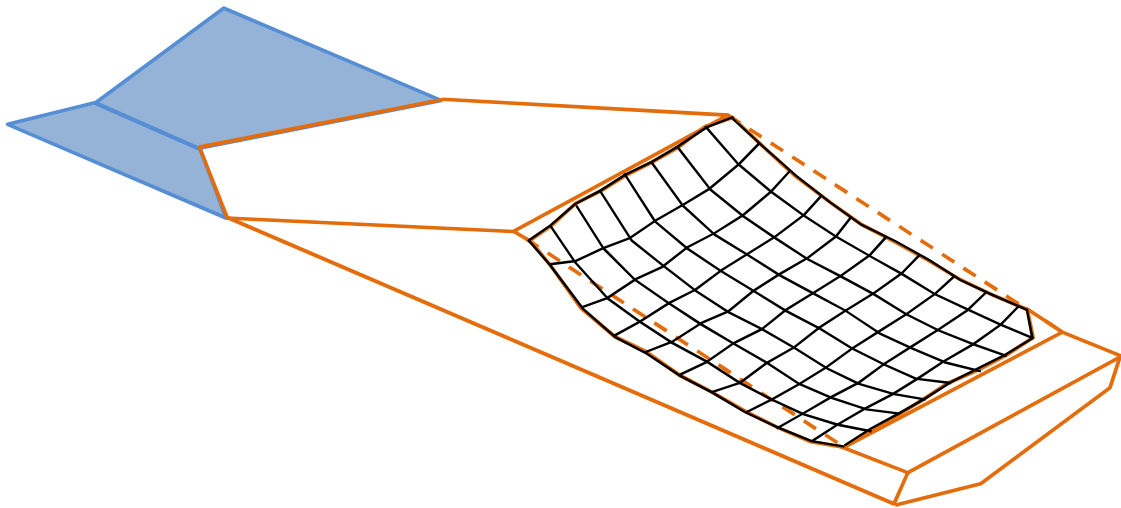


Figure 3.42 3D view of simulated failure surface using extended Spencer method, two-phase seepage analysis case (23° flume slope)

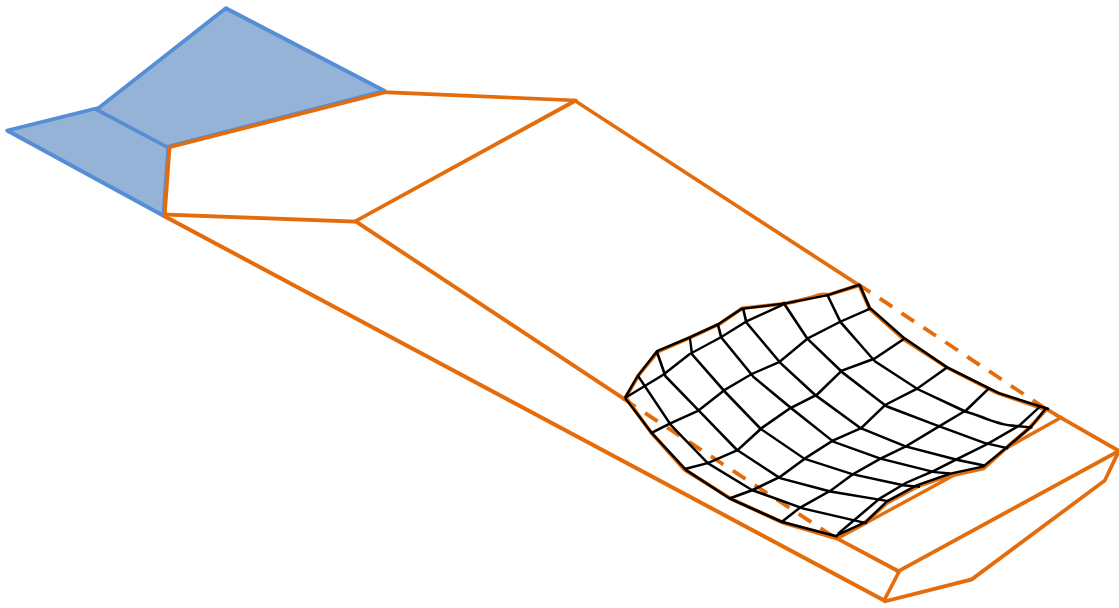


Figure 3.43 3D view of experimentally observed failure surface (28° flume slope)

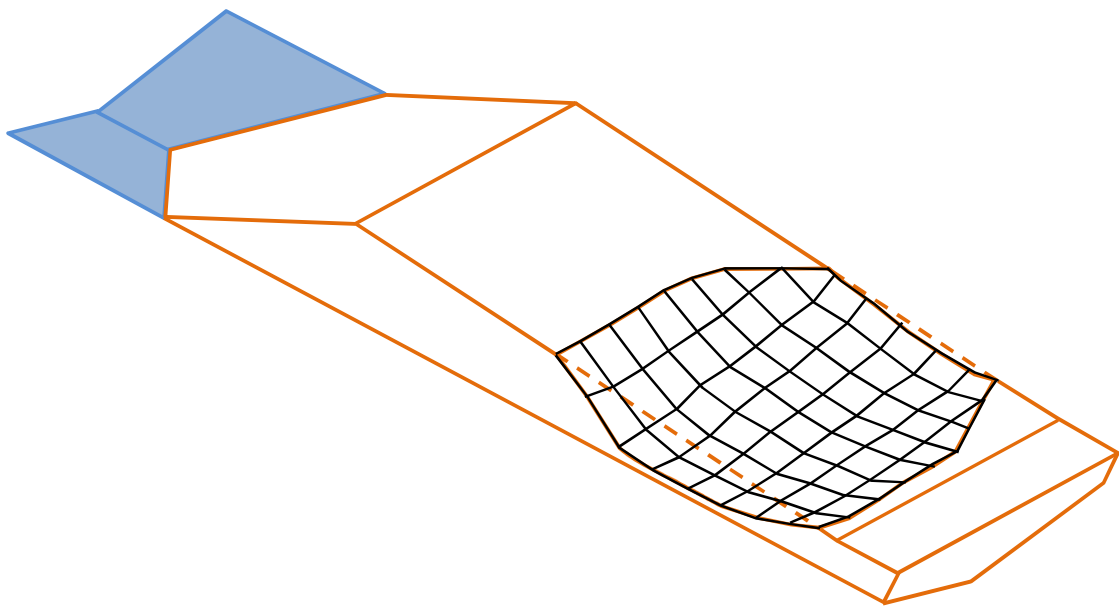


Figure 3.44 3D view of simulated failure surface using Janbu's simplified method, one-phase seepage analysis case (28° flume slope)

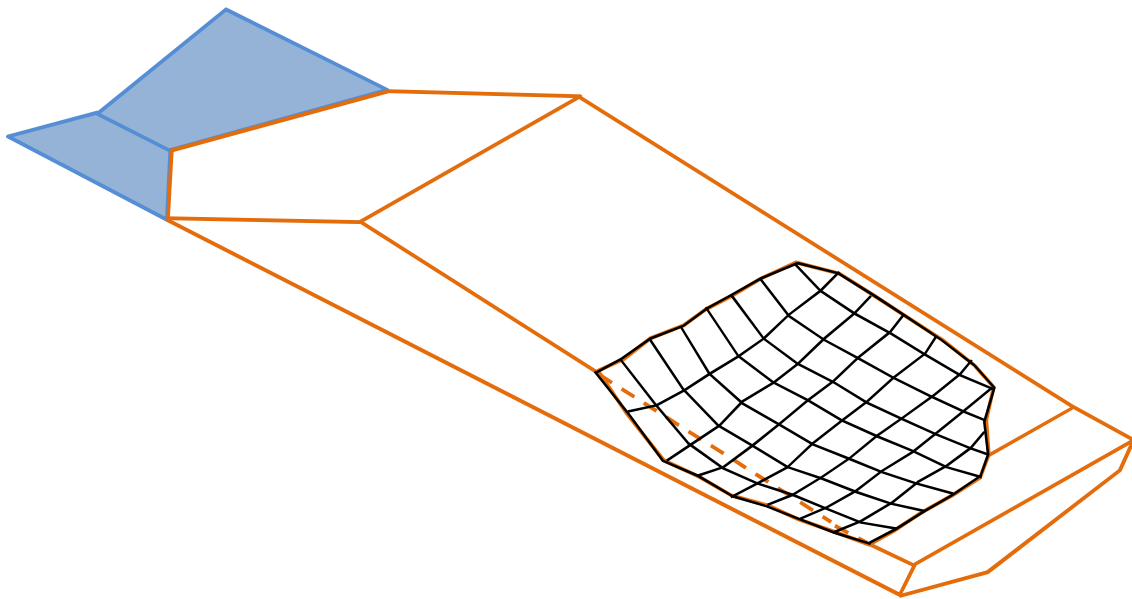


Figure 3.45 3D view of simulated failure surface using extended Spencer method, two-phase seepage analysis case (28° flume slope)

Table 3.3 Summary of slope stability analysis (23° flume slope)

Simulation					Experiment
Seepage Analysis	Slope stability analysis method				
	Janbu's simplified		Extended Spencer		
	Failure time (sec)	$F_s$	Failure time (sec)	$F_s$	
One-phase	2780	0.996	2820	0.984	2779 (EXP-D)
Two-phase	2830	0.992	2850	1.000	2830 (EXP-E)

Table 3.4 Summary of slope stability analysis (28° flume slope)

Simulation					Experiment
Seepage Analysis	Slope stability analysis method				
	Janbu's simplified		Extended Spencer		
	Failure time (sec)	$F_s$	Failure time (sec)	$F_s$	
One-phase	3020	0.994	3060	0.948	3286
Two-phase	3100	0.979	3140	0.964	

Since water-air two-phase flow model has been used to consider the air movement phenomenon inside the model slope body during seepage process, simulated moisture profiles obtained by the water-air two-phase seepage flow model are slightly delayed than that of conventional seepage flow model (Figure 3.3 and 3.4). Ultimately, failure time has also found to be delayed in Janbu's simplified method as well as extended Spencer method.

Janbu's simplified method only satisfies force equilibrium for the entire sliding mass and assumes resultant interslice forces horizontal where as extended Spencer method satisfies both the force and moment equilibrium and assumes resultant interslice forces are at some angle to the horizontal. Due to the vertical component of inclined interslice forces, calculated mobilized shear stress by the extended Spencer method is less than that of Janbu's simplified method in a given condition of moisture content. Hence the factor of safety calculated by the Janbu's simplified method is less than that of extended Spencer method, resulting the failure time of the model slope body earlier in case of Janbu's simplified method.

## **Summary**

3D conventional water-phase seepage flow model as well as the water-air two-phase seepage flow model was coupled with a 2D surface flow and erosion/deposition model for the calculation of pore water pressure, pore air pressure and moisture content within the body of model slope as well as the downstream seepage out flow, surface water head of the runoff produced by the rainfall and erosion and deposition depths on the surface. The governing equations of seepage flow model were solved using line successive over relaxation (LSOR) technique by an implicit iterative finite difference scheme. The finite difference form of the governing equations of surface flow and erosion/deposition model was obtained from the solution methods developed using Leap-Frog scheme. Janbu's simplified method as well as extended Spencer method was incorporated into an effective minimization procedure based on dynamic programming by which the minimal factor of safety and the corresponding critical non circular slip surface were determined simultaneously. The slope stability model calculates the factor of safety and the geometry of critical slip surface according to the pore water pressure and moisture content obtained by seepage flow model.

The numerical simulation and experimental results of pore water pressure pore air pressure and moisture content within the body of model slope as well as the downstream seepage out flow,

surface water forefront propagation and predicted critical slip surface and time of failure of the model slope are in good agreement. However, results obtained by water-air two-phase seepage flow model and extended Spencer method of slope stability analysis were observed more closer to the experimental results than that of conventional seepage flow model and Janbu's simplified method of slope stability analysis.

## **Chapter 4**

# **Analysis of Landslide Dam Failure**

### **4.1 Introduction**

Landslide dams are generally formed by the damming up rivers due to landslides or debris flows caused by heavy rains or earthquakes, which inundates upstream area creating dam reservoir. Outbursts of such dams releases the reservoir water to form a potentially destructive dam break flood, and it also releases the debris of the dam and any accumulated reservoir sediment to the river downstream, causing disasters. So the stability of landslide dams is of the utmost importance. Landslide dam stability depends to a large extent on the material comprising the dam. This in turn depends on the nature of the source material and on the processes that modify it during the travel of the landslide.

Most of the landslide dams break down due to the over flow of the lake water due to a gentle and gradual erosion rather than by abrupt overflow. It may also fail by sudden sliding or progressive failure. In depth knowledge of the failure mechanisms of the landslide dam and measured data are still being lacked. Numerical models from international literature allow to roughly computing the hydrograph resulting from the dam failure, (Fread 1991; Giuseppetti and Molinaro, 1989; Macchione and Sirangelo, 1988), however not giving any indications regarding the whole dam stability.

In this study, two and three dimensional conventional water-phase as well as water-air two-phase seepage flow numerical simulation models are developed individually for seepage calculation inside the body of landslide dam. Seepage flow model is then combined with respective two and three dimensional transient slope stability model to predict the failure of dam due to sudden sliding. Janbu's simplified method as well as Spencer/extended Spencer method is incorporated into dynamic programming to locate the critical slip surface of a general slope of the dam. Simulation results are compared with the experimental results obtained by Awal, 2008 so as to evaluate the capability of the model.

## 4.2 Seepage flow model

In the present analysis, single-phase seepage flow model calculates the pore water pressure and moisture content inside the dam body whereas the two-phase model calculates the pore water pressure, pore air pressure, and moisture content. To develop the seepage flow model, the governing equations are solved by Line Successive Over Relaxation (LSOR) technique used by Freeze (1971a, 1971b, 1978) by an implicit iterative finite difference scheme.

### 4.2.1 Governing equations

Equation (3.1), (3.6) and (3.7) were used for 3D seepage analysis of landslide dam and 2D form of these equations was utilized for 2D seepage analysis. 2D conventional seepage flow equation is as follows.

$$\left( C + S_w S_s \right) \frac{\partial h_w}{\partial t} = \frac{\partial}{\partial x} \left( K_x \frac{\partial h_w}{\partial x} \right) + \frac{\partial}{\partial z} \left( K_z \left( \frac{\partial h_w}{\partial z} + 1 \right) \right) \quad (4.1)$$

where,  $h_w$  is the water pressure head;  $K_x$ , and  $K_z$  are the hydraulic conductivity in  $x$  and  $z$  direction respectively;  $C = \partial \theta_w / \partial h_w$  is the specific moisture capacity,  $\theta_w$  is the soil volumetric water content;  $S_w$  is the saturation ratio;  $S_s$  is the specific storage;  $t$  is the time;  $x$  is the horizontal spatial coordinate; and  $z$  is the vertical spatial coordinate taken as positive upwards.

For 2D water-air two-phase seepage flow analysis, following equations were used.

Water-phase equation

$$C \left( \frac{\partial h_a}{\partial t} - \frac{\partial h_w}{\partial t} \right) = \frac{\partial}{\partial x} \left( K_{wx} \frac{\partial h_w}{\partial x} \right) + \frac{\partial}{\partial z} \left( K_{wz} \left( \frac{\partial h_w}{\partial z} + 1 \right) \right) \quad (4.2)$$

Air-phase equation

$$\left( (n - \theta_w) \frac{\rho_{oa}}{h_o} - \rho_a C \right) \frac{\partial h_a}{\partial t} + \rho_a C \frac{\partial h_w}{\partial t} = \frac{\partial}{\partial x} \left( \rho_a K_{ax} \frac{\partial h_a}{\partial x} \right) + \frac{\partial}{\partial z} \left( \rho_a K_{az} \left( \frac{\partial h_a}{\partial z} + \frac{\rho_a}{\rho_{ow}} \right) \right) \quad (4.3)$$

where,  $h_a$  is the air pressure head;  $h_o$  is the atmospheric pressure expressed in terms of water column height;  $C = \partial \theta / \partial h_c$  is the specific moisture capacity;  $h_c = h_a - h_w$  is capillary head;  $n$  is the porosity of soil;  $\rho_a$  is density of air;  $\rho_{oa}$  is density of air at the atmospheric pressure;  $\rho_{ow}$  is density of water at the atmospheric pressure;  $K_{wx}$  and  $K_{wz}$  are the hydraulic conductivity in  $x$  and

$z$  directions respectively; and  $K_{ax}$  and  $K_{az}$  are the air conductivity in  $x$  and  $z$  directions respectively.

## Solution approach

The finite difference form of Equation 4.1 is as follows:

$$C \left( \frac{h_{w,i,k}^t - h_{w,i,k}^{t-1}}{\Delta t} \right) = \frac{1}{\Delta x} \left[ K1 \left( \frac{h_{w,i+1,k}^t + h_{w,i+1,k}^{t-1} - h_{w,i,k}^t - h_{w,i,k}^{t-1}}{2\Delta x} \right) - K2 \left( \frac{h_{w,i,k}^t + h_{w,i,k}^{t-1} - h_{w,i-1,k}^t - h_{w,i-1,k}^{t-1}}{2\Delta x} \right) \right] + \frac{1}{\Delta z} \left[ K3 \left( \frac{h_{w,i,k+1}^t + h_{w,i,k+1}^{t-1} - h_{w,i,k}^t - h_{w,i,k}^{t-1}}{2\Delta z} + 1 \right) - K4 \left( \frac{h_{w,i,k}^t + h_{w,i,k}^{t-1} - h_{w,i,k-1}^t - h_{w,i,k-1}^{t-1}}{2\Delta z} + 1 \right) \right] \quad (4.4)$$

For vertical LSOR, the terms can be grouped as

$$-A_k h_{w,i,k+1}^t + B_k h_{w,i,k}^t - C_k h_{w,i,k-1}^t = D_k \quad (4.5)$$

where,

$$A_k = \frac{K3}{2\Delta z^2} \quad (4.6)$$

$$B_k = \frac{C}{\Delta t} + \frac{K1}{2\Delta x^2} + \frac{K2}{2\Delta x^2} + \frac{K3}{2\Delta z^2} + \frac{K4}{2\Delta z^2} \quad (4.7)$$

$$C_k = \frac{K4}{2\Delta z^2} \quad (4.8)$$

$$D_k = \frac{C}{\Delta t} h_{w,i,k}^{t-1} + K1 \left( \frac{h_{w,i+1,k}^t + h_{w,i+1,k}^{t-1} - h_{w,i,k}^t - h_{w,i,k}^{t-1}}{2\Delta x^2} \right) - K2 \left( \frac{h_{w,i,k}^{t-1} - h_{w,i-1,k}^t - h_{w,i-1,k}^{t-1}}{2\Delta x^2} \right) + K3 \left( \frac{h_{w,i,k+1}^{t-1} - h_{w,i,k}^t}{2\Delta z^2} + \frac{1}{\Delta z} \right) - K4 \left( \frac{h_{w,i,k}^{t-1} - h_{w,i,k-1}^t}{2\Delta z^2} + \frac{1}{\Delta z} \right) \quad (4.9)$$

The set of Equations 4.5 for a line scan, form a tri-diagonal matrix equation that can be solved by the well-known triangularization scheme whose solution is similar to Equation 3.14 as described in section 3.2.1. Similarly we can get the finite difference form of Equations 4.2 and 4.3.

### 4.2.2 Boundary conditions

Based on upstream reservoir water level, top surface boundary conditions are allowed as the variable head boundary or no flow boundary in the equation for water-phase. However, in equation for air phase no air flow at the surface or variable air pressure head is allowed. Downstream boundary condition is modeled as seepage face with zero pressure head; and

upstream, left and right boundaries are considered as no flow boundaries for both water and air phase equations.

### 4.3 Slope stability model

For 3D slope stability analysis of landslide dam, Equations 3.71, 3.72 and 3.73 were used and which have already been described in section 3.3. This section covers the illustration of 2D slope stability model used in the analysis.

#### 4.3.1 Janbu's simplified method

The factor of safety  $F_s$  for 2D Janbu's simplified method is expressed by the following equation (Awal et al., 2009).

$$F_s = \frac{1}{\sum_{i=1}^n (W_i + P_i) \tan \alpha_i} \sum_{i=1}^n \frac{c_e l_i \cos \alpha_i + (W_i - u_{p_i} l_i \cos \alpha_i) \tan \phi}{\cos^2 \alpha_i + \left(1 + \frac{1}{F_s} \tan \alpha_i \tan \phi\right)} \quad (4.10)$$

where  $W_i$  is the weight of each slice including surface water;  $P_i$  vertical external force i.e., surface water weight, acting on the top of the column;  $l_i$  is the length of the base of each slice;  $u_{p_i}$  is the average pore water pressure on the base of the slice;  $\alpha_i$  is the inclination of the base to the horizontal;  $n$  is the total number of slices; and  $c_e$  and  $\phi$  are the Mohr-Coulomb strength parameters..

#### 4.3.2 Spencer method

The factor of safety expressions for Spencer method (Bardet, et al., 1989) is as follows.

$$F_f = \frac{\sum_{i=1}^n [c_e l_i + \{(W_i + P_i) \cos \alpha_i - u_{p_i} l_i\} \tan \phi] / m_\alpha}{\sum_{i=1}^n (W_i + P_i) \sin \alpha_i / m_\alpha} \quad (4.11)$$

$$F_m = \frac{\sum_{i=1}^n [c_e l_i + \{(W_i + P_i) \cos \alpha_i - u_{p_i} l_i\} \tan \phi] D_i \cos(\theta_i - \delta) / m_\alpha}{\sum_{i=1}^n (W_i + P_i) \sin \alpha_i D_i \cos(\theta_i - \delta) / m_\alpha} \quad (4.12)$$

where,  $F_f$  and  $F_m$  are the factor of safety with respect to force equilibrium and moment equilibrium respectively;  $m_\alpha = \cos(\alpha_i - \delta) \{1 + (1/F) \tan(\alpha_i - \delta) \tan \phi\}$  with  $F = F_f$  for Equation 4.11 and  $F_m$  for Equation 4.12;  $\delta$  is the inclination of interslice forces to the horizontal;  $D_i$  is the distance from the base centre of the slice to an arbitrary reference point; and  $\theta_i$  is the angle between the horizontal direction and the  $D$  direction in the  $xz$  plane.

$F_f$  and  $F_m$  can separately be computed from the Equations 4.11 and 4.12 for several appropriately given values of  $\delta$ . Then, two curves showing the relationships of  $F_f - \delta$  and  $F_m - \delta$  can be plotted so that the intersection of these two curves leads to a required  $\delta_o$  value and corresponding factor of safety  $F_s$ , satisfying both force and moment equilibrium.

### 4.3.3 Dynamic programming search procedure

Baker (1980) successfully introduced DP into 2D slope stability analyses by applying it to Spencer method. Later Yamagami and Ueta (1986) applied this idea to 2D Janbu method.

Equation 4.10 can be represented by the following expression.

$$F_s = \frac{\sum_{i=1}^n R_i}{\sum_{i=1}^n T_i} \quad (4.13)$$

where,

$$R_i = \sum_{i=1}^n \frac{c_e l_i \cos \alpha_i + (W_i - u_{p_i} l_i \cos \alpha_i) \tan \phi}{\cos^2 \alpha_i + \left(1 + \frac{1}{F_s} \tan \alpha_i \tan \phi\right)} \quad (4.14)$$

$$T_i = \sum_{i=1}^n (W_i + P_i) \tan \alpha_i \quad (4.15)$$

In order to minimize the functional  $F_s$ , defined in Equation 4.13, the auxiliary functional  $G$  is defined as (Baker, 1980).

$$G = \sum_{i=1}^n [R_i - F_s T_i] = \sum_{i=1}^n DG_i \quad (4.16)$$

When applying dynamic programming, minimization of  $G$  is carried out over all admissible slip surfaces.

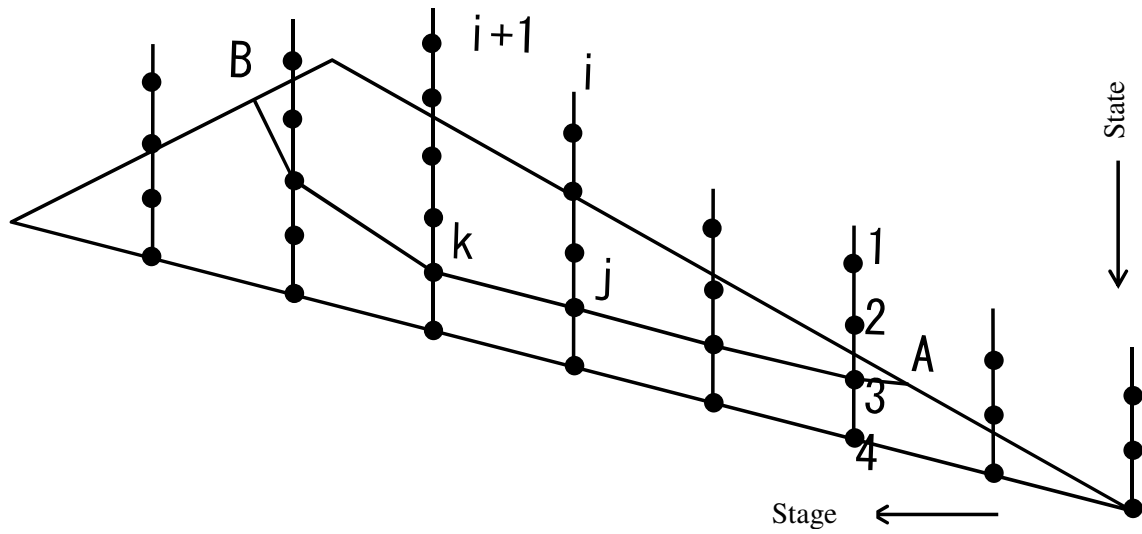


Figure 4.1 Typical schematic sample of stages, states and slip surface in a 2D slope

$$G_m = \min G = \min \sum_{i=1}^n DG_i \quad (4.17)$$

A value of  $F_s$  in Equation 4.16 is initial assumed and is updated by iteration until some convergence criterion is satisfied. Figure 4.1 illustrates stage-state system for a 2D slope (Yamagami and Jiang, 1997). An arbitrary line  $jk$  which connects points  $(i, j)$  and  $(i+1, k)$  is considered as a part of assumed slip surface.  $R_i$  and  $T_i$  on the surface  $jk$  are obtained from Equations 4.14 and 4.15 and the return function is calculated using Equation 4.18.

$$G = \sum_{i=1}^n [R_i - F_s T_i] = \sum_{i=1}^n DG_i = \sum_{i=1}^n DG_i(jk) \quad (4.18)$$

If  $H_i(j)$ , the optimal value function in dynamic programming, signifies the minimum value of  $G$  from the point  $A$  (Figure 4.1) to the point  $(i,j)$ , then based on Bellman's principle of optimality the minimum  $G$  value from  $A$  to  $(i+1,k)$  is given by Equation 4.19.

$$H_{i+1}(k) = \min [H_i(j) + DG_i(j,k)], \quad i = 1 \sim n, j = 1 \sim S_i, k = 1 \sim S_{i+1} \quad (4.19)$$

The boundary conditions are

$$H_1(j) = 0, \quad j = 1 \sim S_1 \quad (4.20)$$

$$G_m = \min G = \min [H_{n+1}(j)], \quad j = 1 \sim S_{i+1} \quad (4.21)$$

Difference between the value of  $F_s$  calculated by Equation 4.13 after this procedure and initially assumed value of  $F_s$  should be within tolerance, therefore, iteration is required to obtain exact value of  $F_s$  along the slip surface.

The search scheme by Yamagami and Jiang (1997) can also be coupled with Equations 4.11 and 4.12 separately to determine minimum values for  $F_f$  and  $F_m$  and the computation procedure is already illustrated in section 3.3.3.

## 4.4 Results and discussions

Experimental results obtained by Awal (2008) were compared with the simulation results so as to evaluate the capability of the model. He considered constant water level and the steady discharge in the upstream reservoir in case of two-dimensional experiments and steady discharge in the upstream reservoir in case of three-dimensional experiments.

In case of two-dimensional experiments a rectangular flume of length 5m, width 20cm and depth 21cm was used. The slope of the flume was set at  $17^\circ$ . A rectangular flume of 5m long, 30cm wide and 50cm deep was used in case of three-dimensional experiments. The slope of the flume was set at  $20^\circ$ . It is difficult to observe the three dimensional view of the failure surface in rectangular flume shape. So, the rectangular shape of the flume was modified to make cross slope of  $20^\circ$ . The height of the dam was 30cm in one side and decreased uniformly towards other side to 19.08cm.

Triangular dam was prepared on the rigid bed of flume by placing mixed silica sand (Mix 1-7) on the flume. Water content reflectometers (WCRs) were used to measure the temporal variation of moisture content during seepage process. Red colored sediment strips were placed in the dam body at the flume wall face so as to measure the movement of the dam slope during sliding. Some parameter values of the sediment used in the experiments are listed in Table 4.1. The grain size distributions of the sediment are shown in Figure 4.2. The two-dimensional and three-dimensional landslide dams with the arrangement of WCRs are schematically shown in Figure 4.3 and Figure 4.4 respectively.

In two dimensional analysis numerical simulation was carried out with spacing of 2mm and time

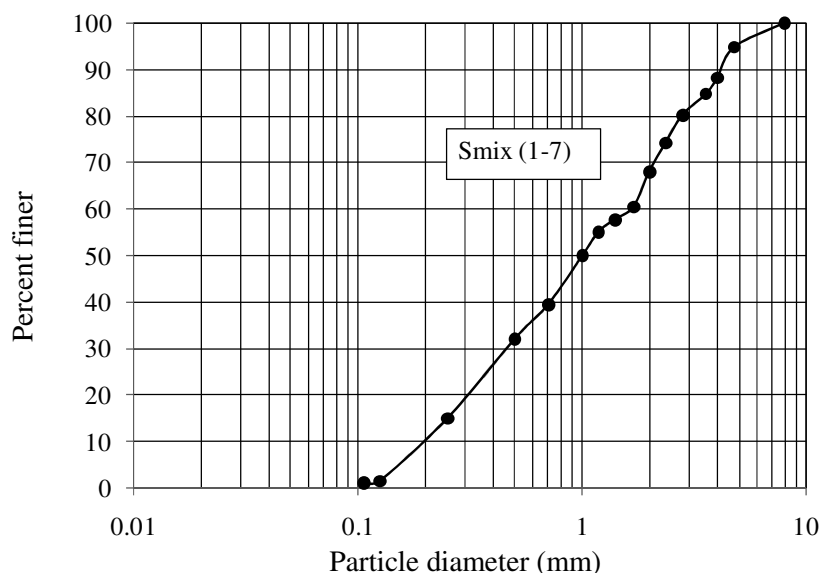


Figure 4.2 Grain size distribution of the sediment

Table 4.1 Some parameter values of the sediment considered

Sediment type	Smix (1-7)
Saturated moisture content, $\theta_s$	0.287
Residual moisture content, $\theta_r$	0.045
van Genuchten parameter, $\alpha$	5.50
van Genuchten parameter, $\eta$	3.20
Specific gravity, $G_s$	2.65
Mean grain size, $D_{50}$ (mm)	1.0
Angle of repose, $\phi$	$34^\circ$
Porosity, $n$	0.345
Compression index, CI	1.11

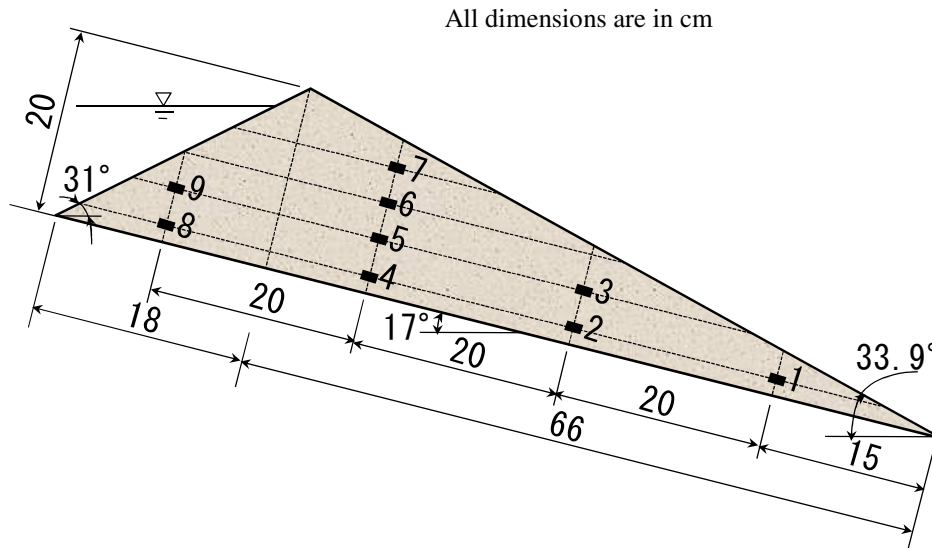


Figure 4.3 Two dimensional dam body shape and size with the arrangements of WCRs (1-9)

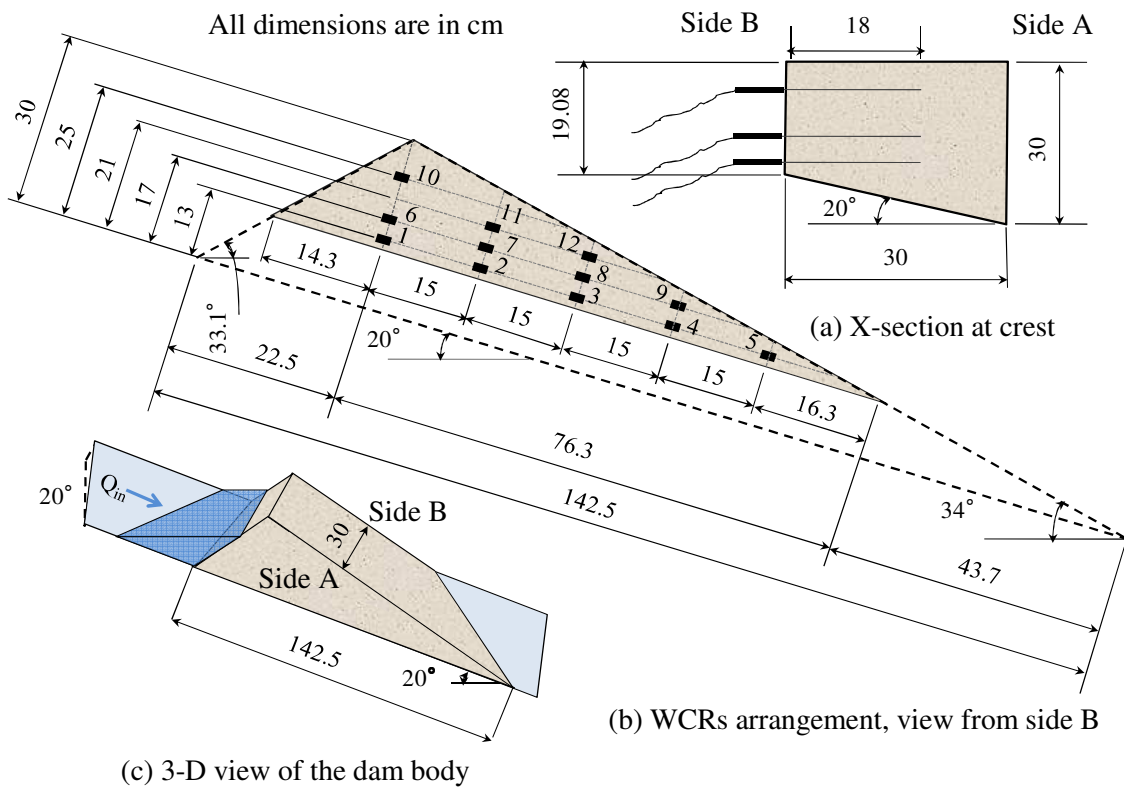


Figure 4.4 Three dimensional dam body shape and size with the arrangements of WCRs (1-12)

step of 0.004 second in seepage flow model and longitudinal spacing (parallel to dam base) of 6cm and time step of 1 second in slope stability model. In three dimensional analysis numerical simulation was carried out with spacing of 1cm and time step of 0.01 second in seepage flow model and longitudinal spacing of 5cm, lateral spacing of 3cm and time step of 1 second in slope

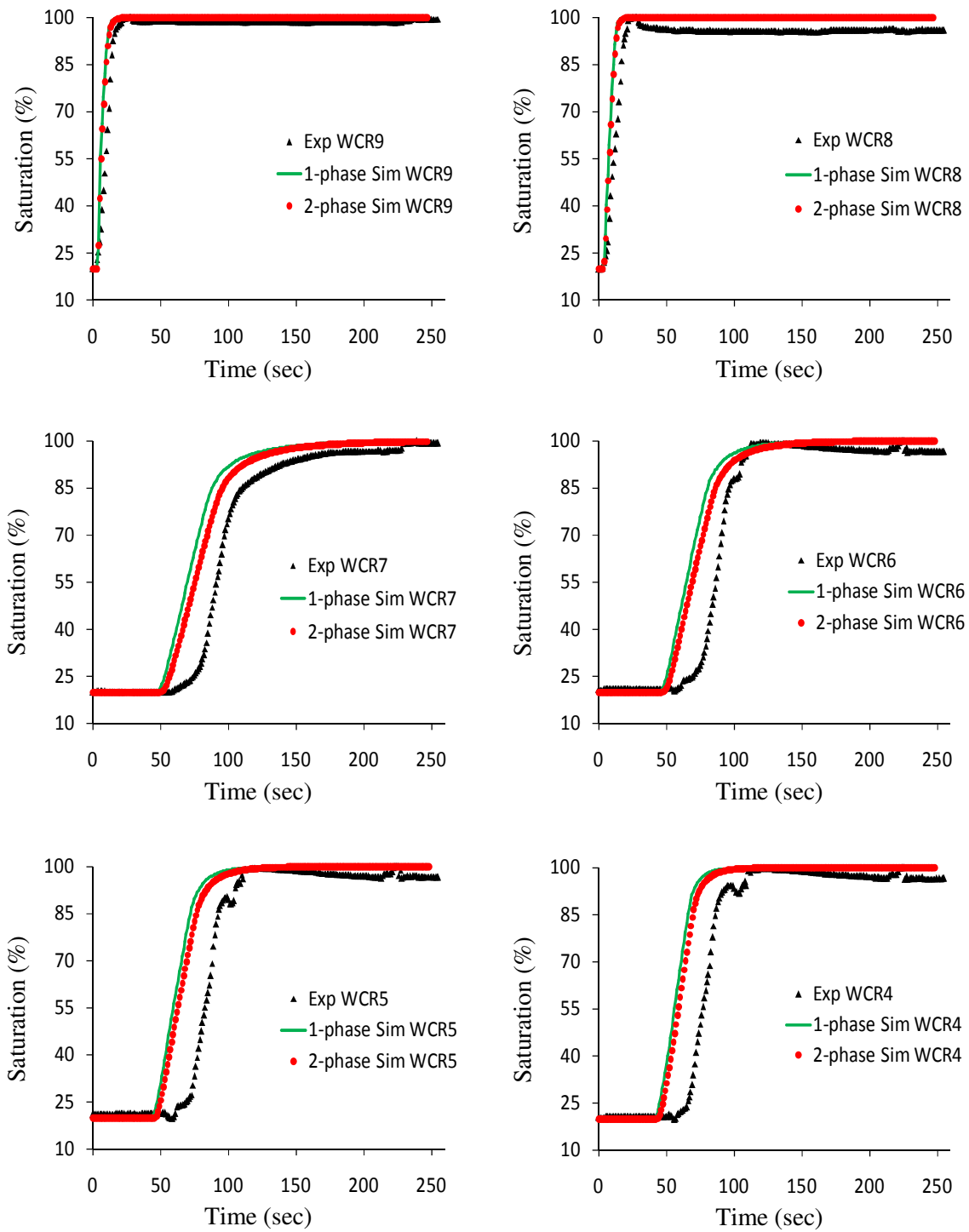


Figure 4.5 Simulated and experimental moisture content profiles for constant head in upstream reservoir (WCRs – 4 to 9), 2D case

stability model.

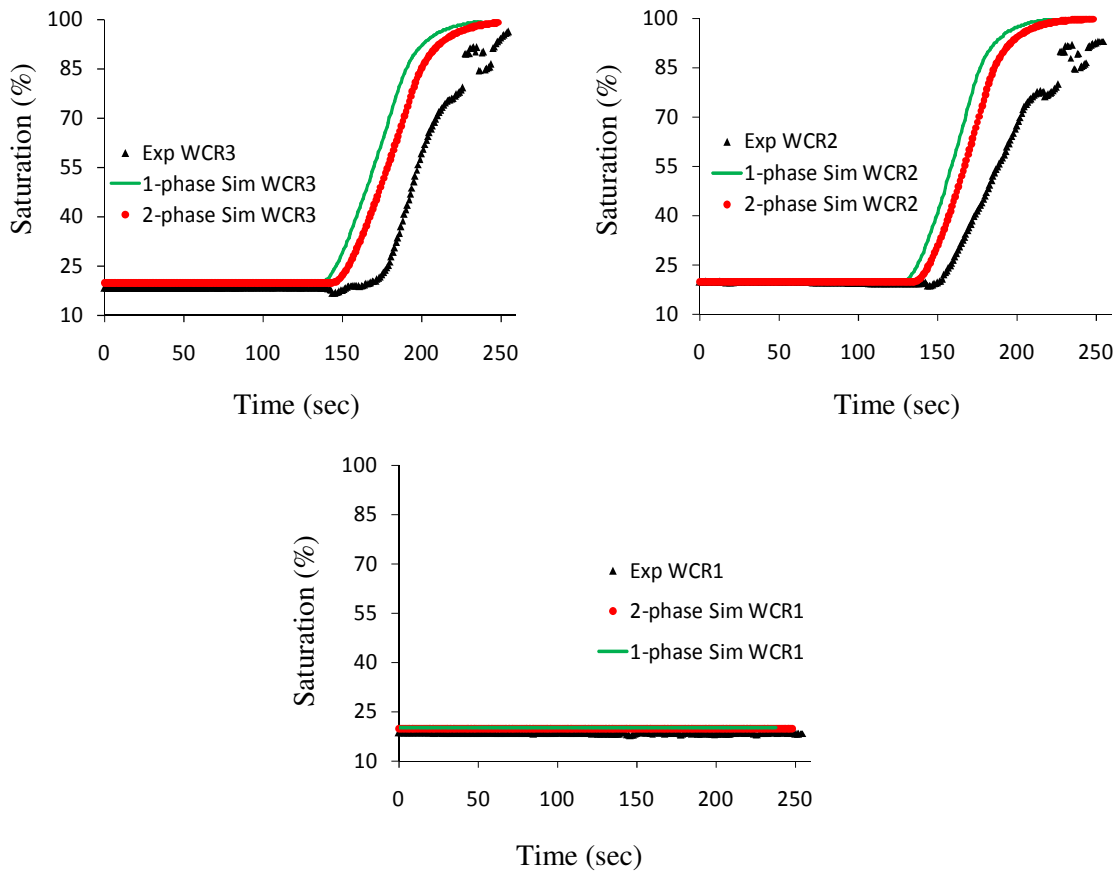


Figure 4.6 Simulated and experimental moisture content profiles for constant head in upstream reservoir (WCRs – 1 to 3), 2D case

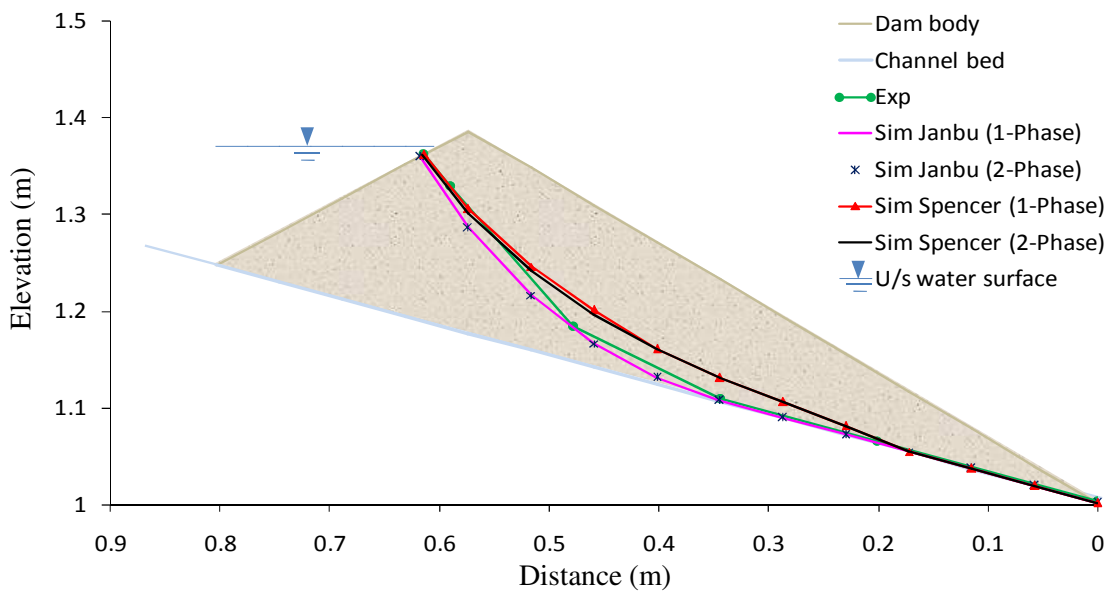


Figure 4.7 Simulated and experimental failure surfaces for constant head in upstream reservoir (2D case)

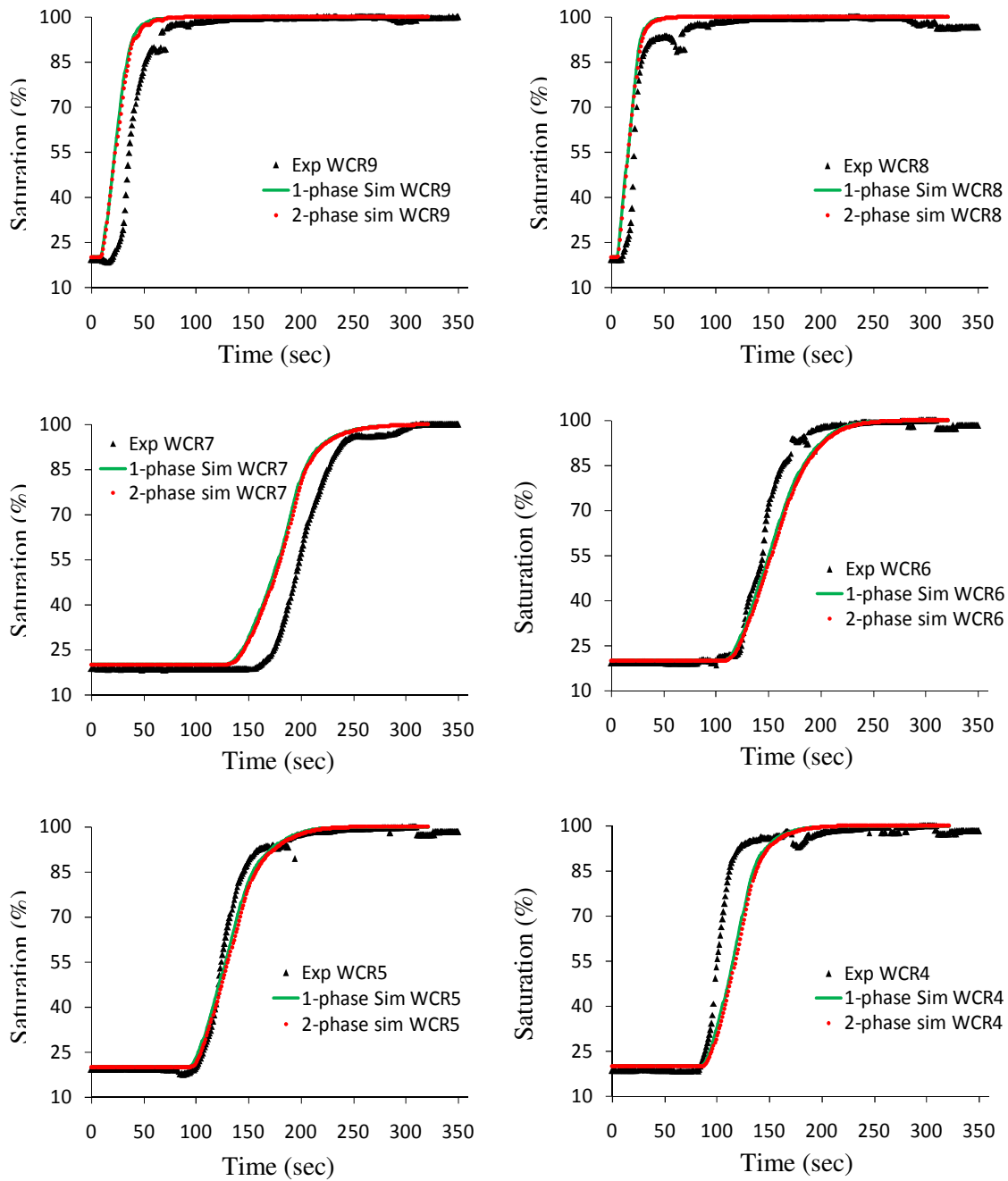


Figure 4.8 Simulated and experimental moisture content profiles for steady discharge in upstream reservoir (WCRs – 4 to 9), 2D case

In case of 2D experiment with constant water level in the upstream reservoir, water level at 16 mm below the crest level of the dam was maintained in 25 seconds and the sudden sliding of the dam was observed at 255 seconds. The simulated failure time using Janbu's simplified method of slope stability analysis was 222 and 231 seconds in conventional and water-air two-phase seepage flow considerations respectively whereas the failure time using Spencer method of

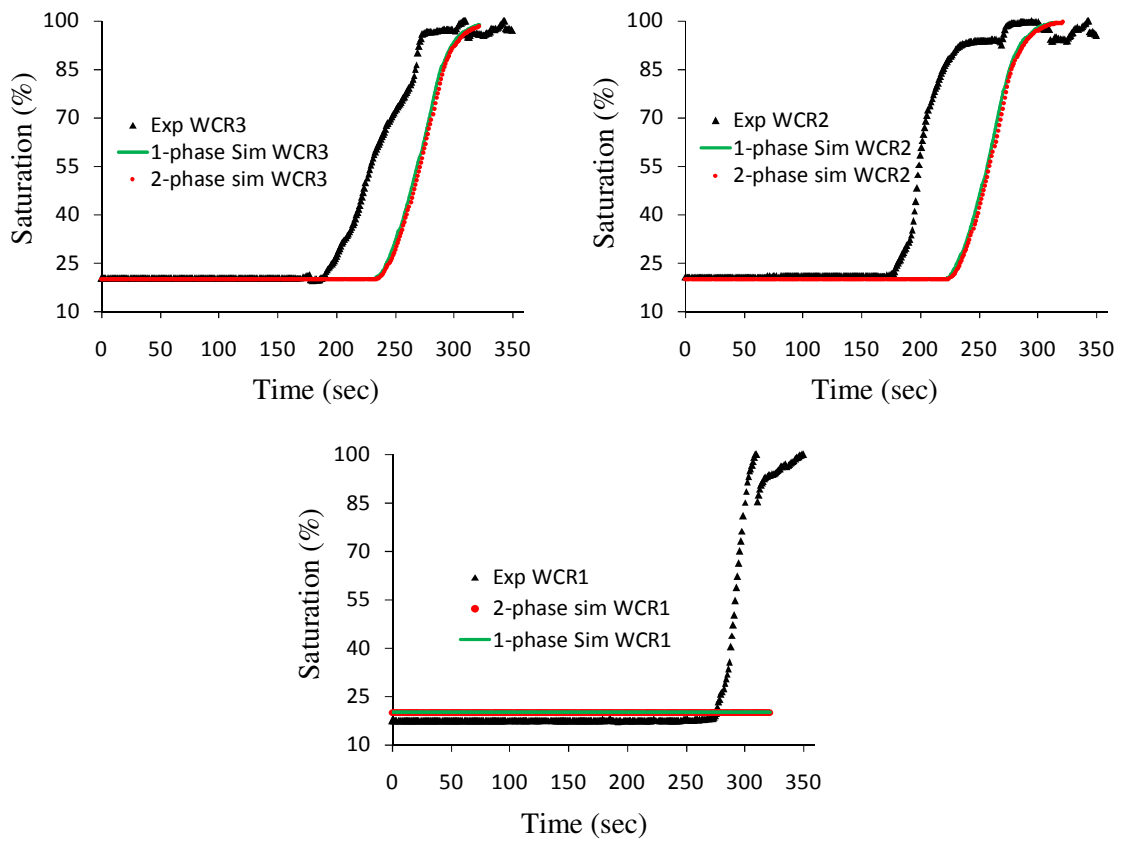


Figure 4.9 Simulated and experimental moisture content profiles for steady discharge in upstream reservoir (WCRs – 1 to 3), 2D case

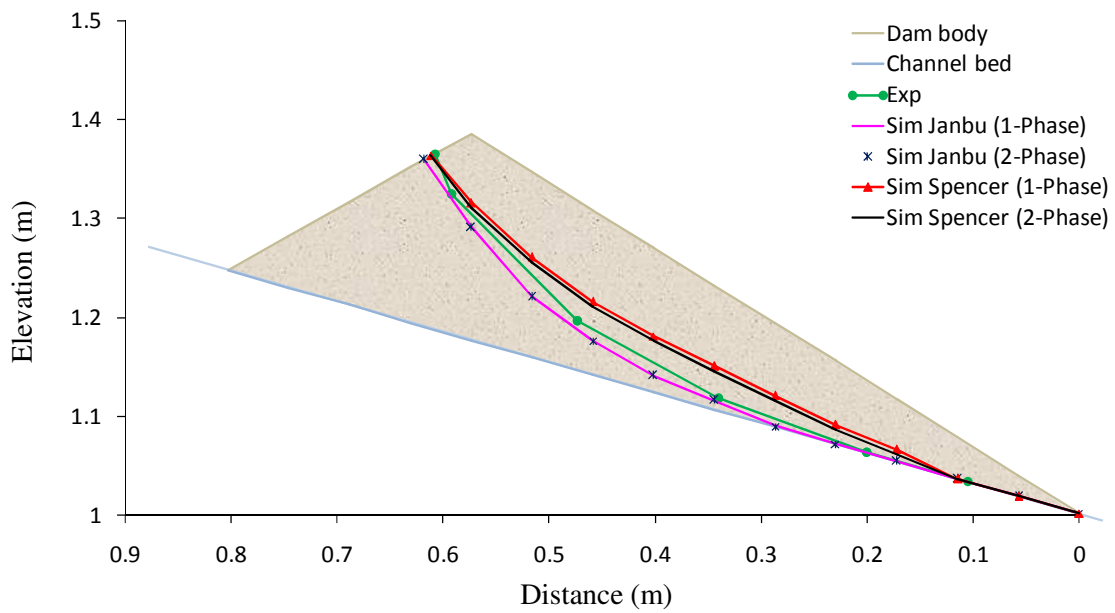


Figure 4.10 Simulated and experimental failure surfaces for steady discharge in upstream reservoir (2D case)

slope stability analysis was 248 and 257 seconds in conventional and water-air two-phase seepage flow considerations respectively. Figures 4.5 and 4.6 show the simulated and experimental moisture content profiles at WCR1 through WCR9 and Figure 4.7 shows the simulated and experimental slip surfaces.

In case of 2D experiment with steady discharge in the upstream reservoir, 39.8 cm<sup>3</sup>/sec discharge was maintained and the sudden sliding of the dam was observed at 350 seconds. The simulated failure time using Janbu's simplified method of slope stability analysis is 305 and 304 seconds in conventional and water-air two-phase seepage flow considerations respectively whereas the failure time using Spencer method of slope stability analysis is 323 and 322 seconds in conventional and water-air two-phase seepage flow considerations respectively. Figures 4.8 and 4.9 show the simulated and experimental moisture content profile at WCR1 through WCR9 and Figure 4.10 shows the simulated and experimental slip surfaces.

In most of the WCRs, simulated and experimental moisture profiles are satisfactorily in agreement although results comparison shows some simulated results have faster moisture movement than that of experimental one (WCRs 7, 9) and some have slower movement (WCRs 1,2,3,4). The WCR farthest away from the head reach and closer to the base of the dam body has maximum delayed moisture profile in simulation than experiment in comparison to others (WCR1). This indicates the movement of moisture a little bit slower in simulation than experiment. Consequently, reservoir water level raising rate is faster in simulation than experiment so that moisture reached earlier in WCRs which are closest to the head reach and surface of the dam body as well (WCRs 7, 9). Since the dam body mass in head reach is dominant for the slope failure, failure time of the dam computed in simulation also found faster than experiment. However the simulated failure shapes are also matching satisfactorily with experimental failure shapes of all considered cases. Since water-air two-phase flow model has been used to consider the air movement phenomenon inside the dam during seepage process, the water infiltration rate was slower than one-phase flow model so that the reservoir water level increased a little bit faster than one-phase flow model in steady discharge case, resulting a little bit faster sliding (1 second) than one-phase case. Such insignificant faster rate would not be dominated for the earlier failure of dam, if 3D nature of moisture movement phenomenon and shape of failure surface was considered.

In case of 3D steady discharge in the upstream reservoir,  $29.8 \text{ cm}^3/\text{sec}$  discharge was supplied and the sudden sliding of the dam was observed at 930 seconds. The simulated failure time using Janbu's simplified method of slope stability analysis is 768 and 777 seconds in conventional and water-air two-phase seepage flow considerations respectively whereas the failure time using extended Spencer method of slope stability analysis is 793 and 802 seconds in conventional and water-air air two-phase seepage flow considerations respectively. Figure 4.11 and Figure 4.12 show the simulated and experimental moisture content profile at different

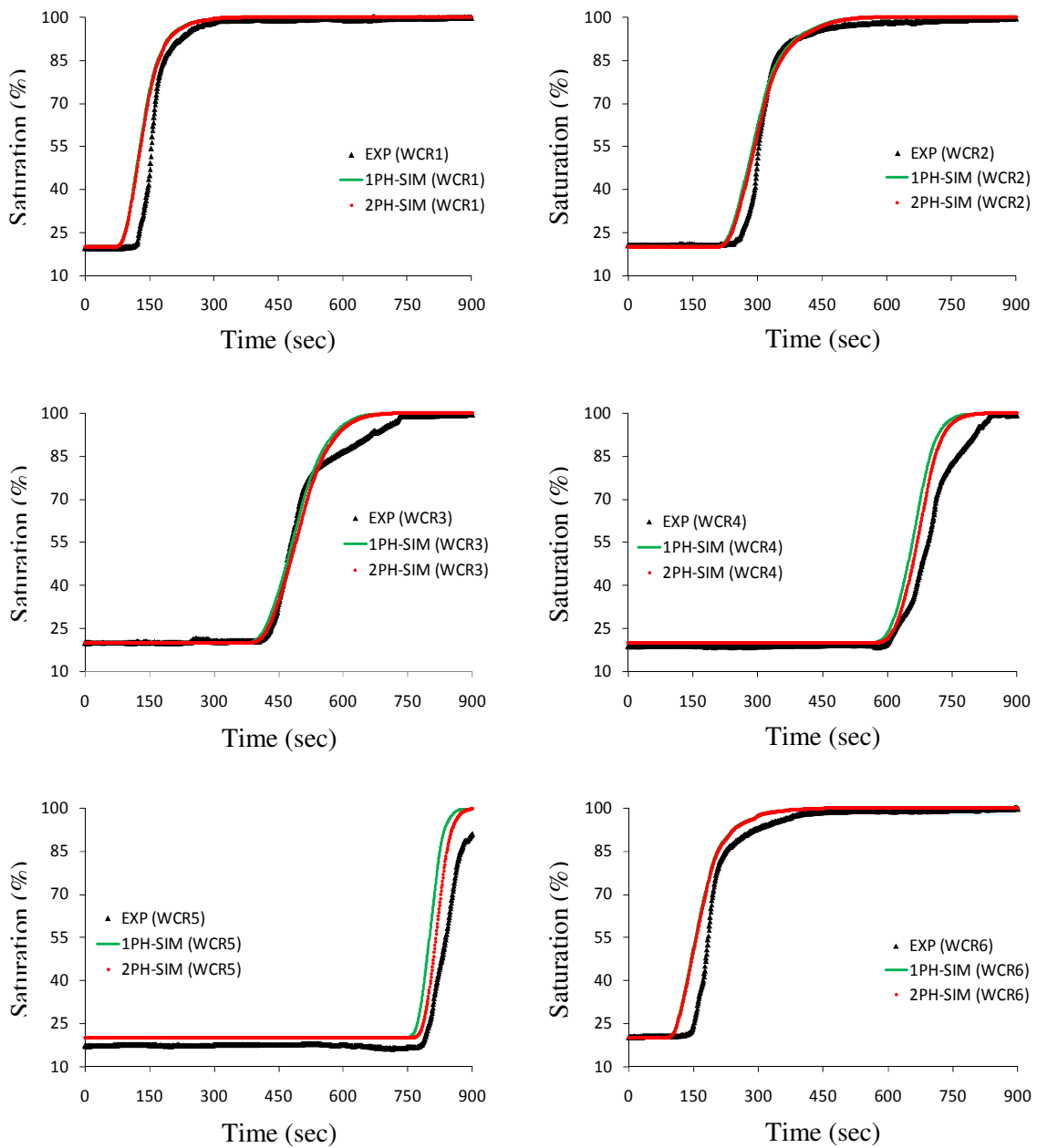


Figure 4.11 Simulated and experimental moisture content profiles at WCRs 1- 6 (3D case)

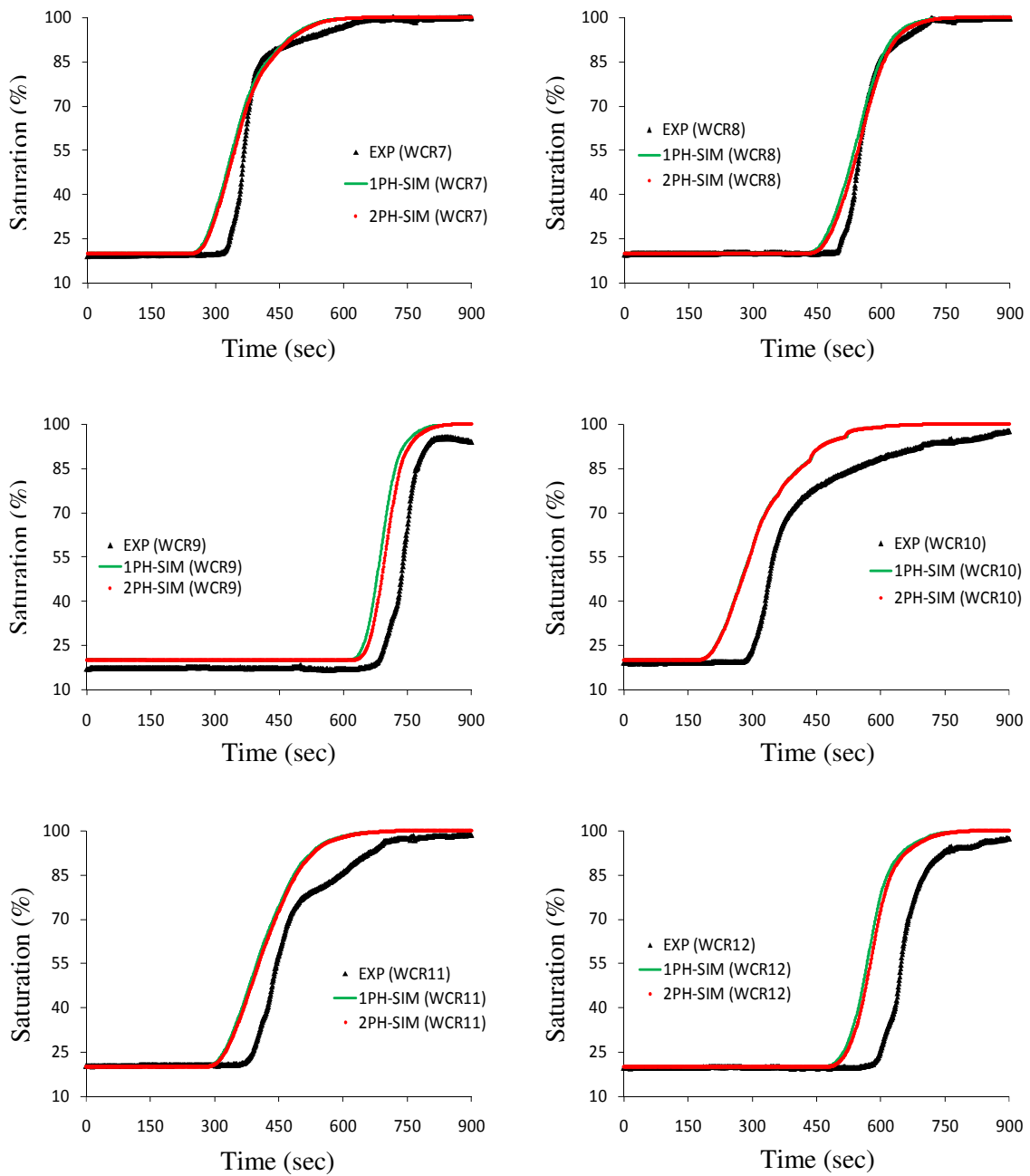


Figure 4.12 Simulated and experimental moisture content profiles at WCRs 7- 12 (3D case)

WCRs which are in good agreement with attainment of full saturation that is found to be earlier in all WCRs of simulated results rather than that of experimental. Figure 4.13 and Figure 4.14 show the simulated and experimental slip surfaces in side A and side B respectively. In side A of the dam body, computed slip surface is very close to the experimentally observed slip surface whereas in side B computed slip surface is shallower than that of experimentally observed. Table 4.2 presents the summary of the slope stability analysis.

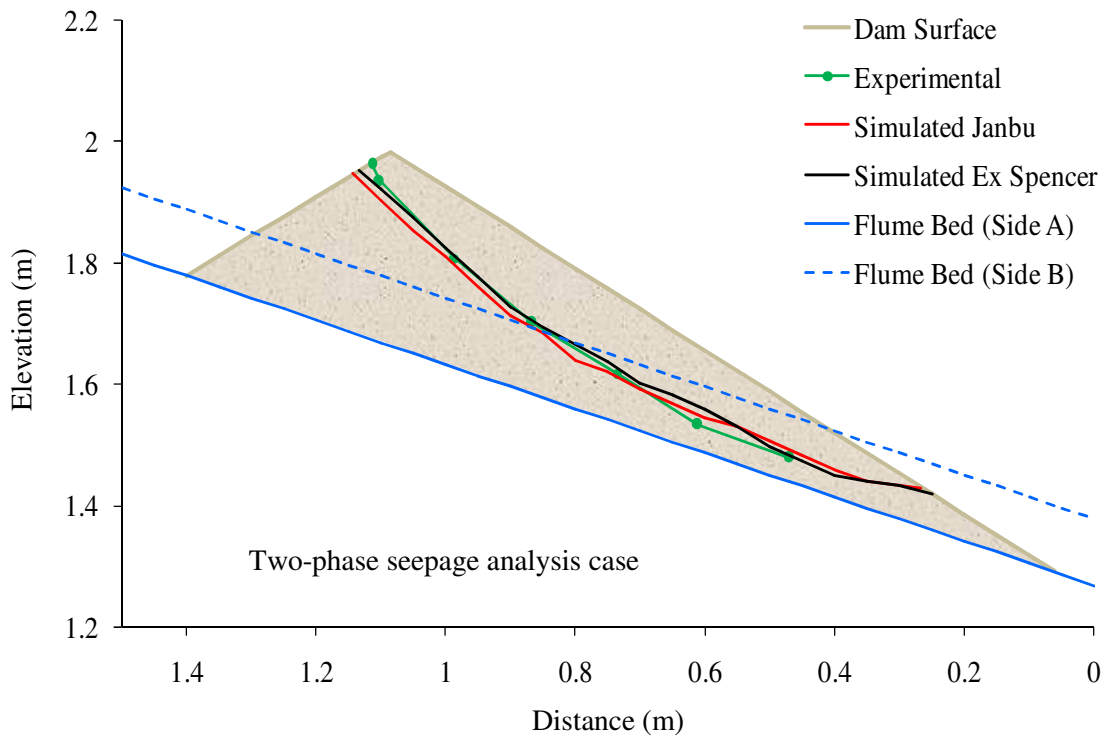
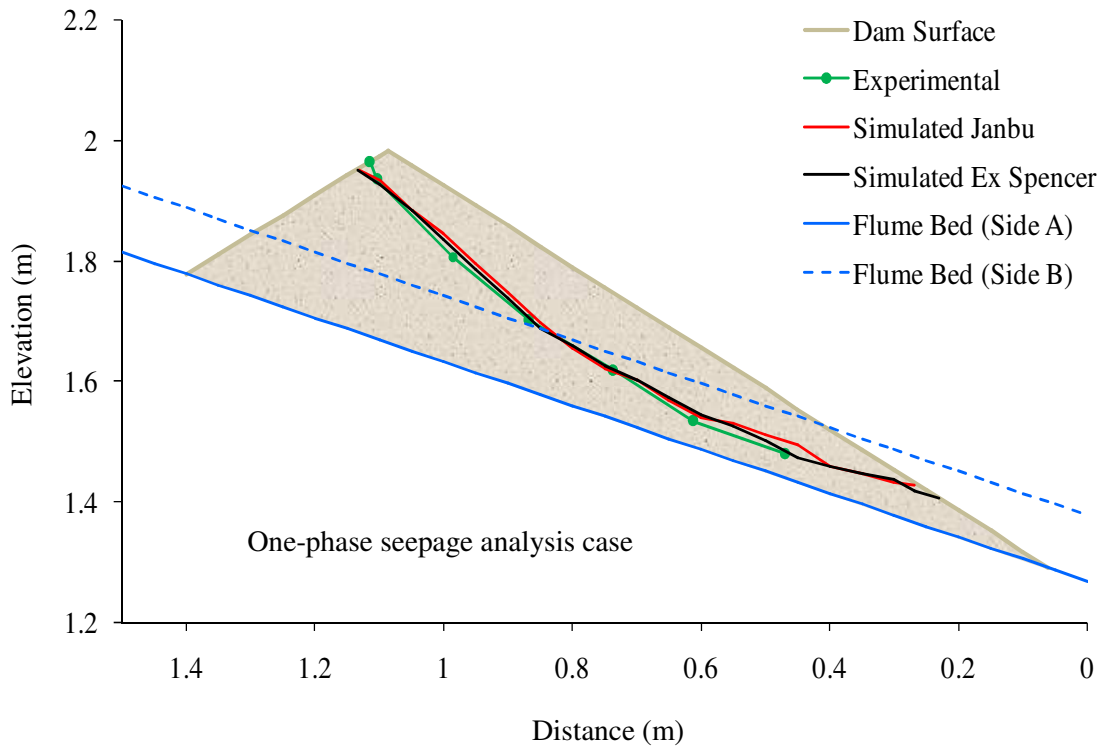


Figure 4.13 Comparison of longitudinal profiles of experimental and simulated failure surfaces in side A (3D case)

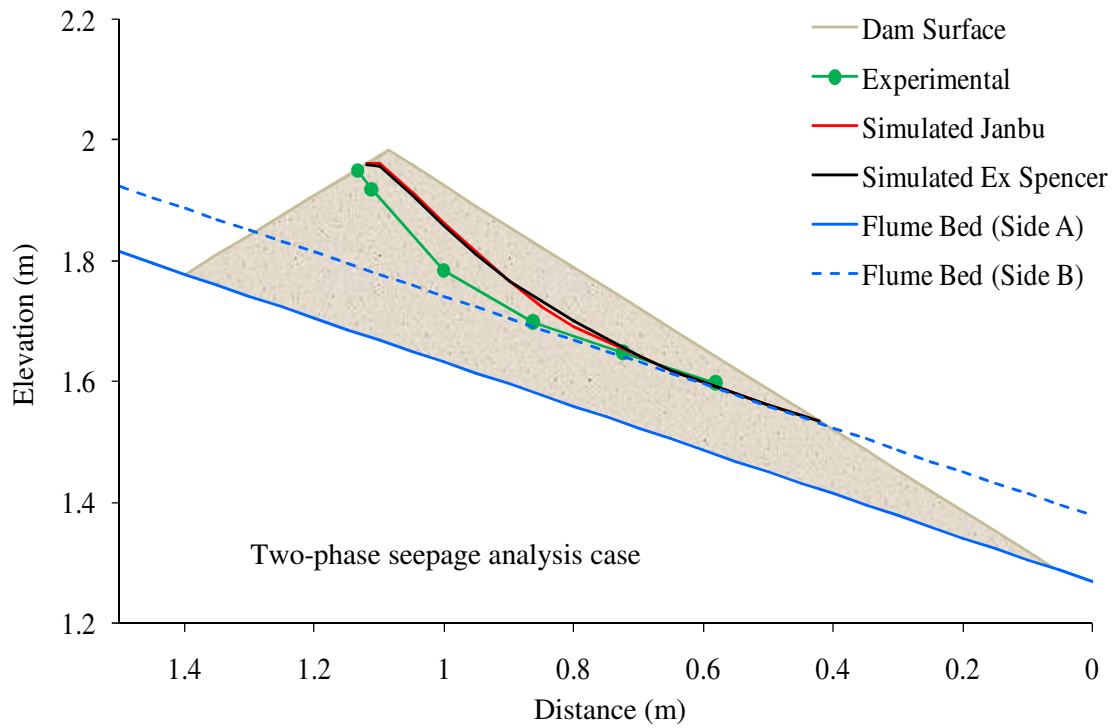
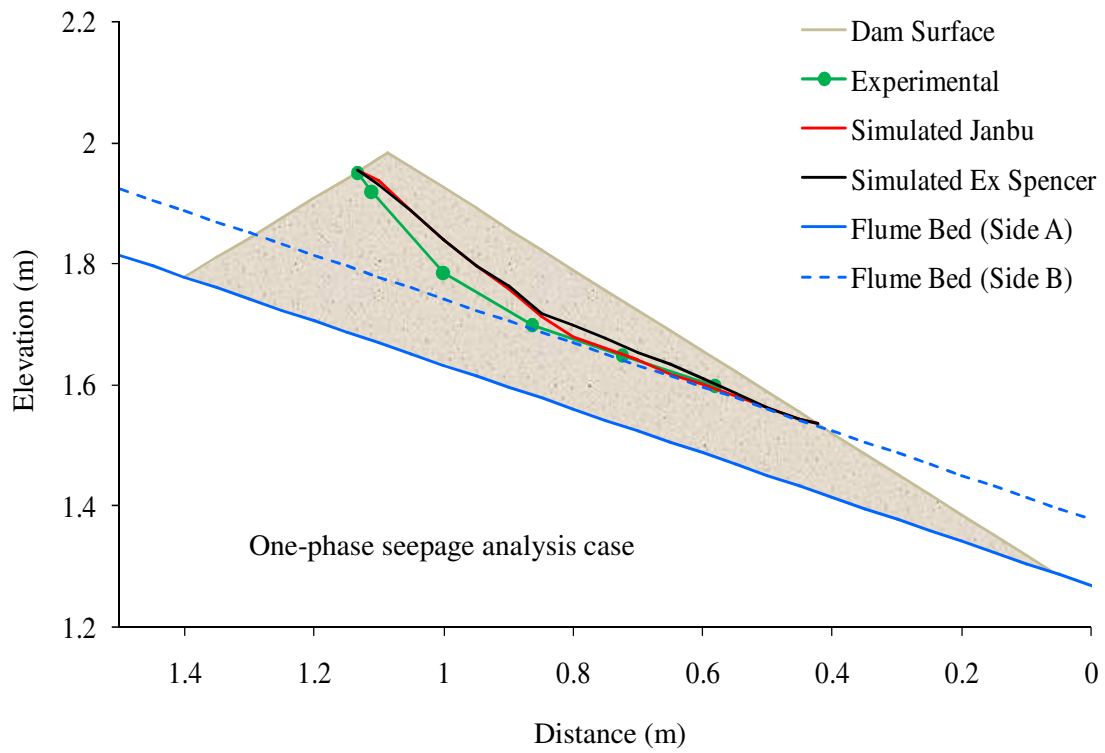


Figure 4.14 Comparison of longitudinal profiles of experimental and simulated failure surfaces in side B (3D case)

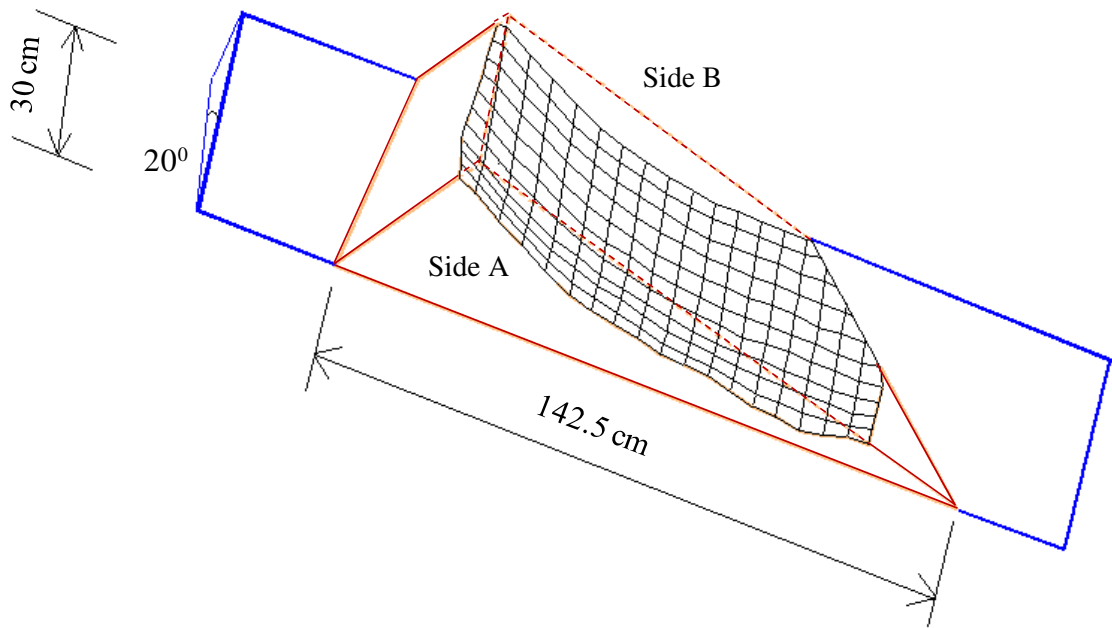


Figure 4.15 3D view of failure surface, computed by extended Spencer method (two-phase seepage consideration)

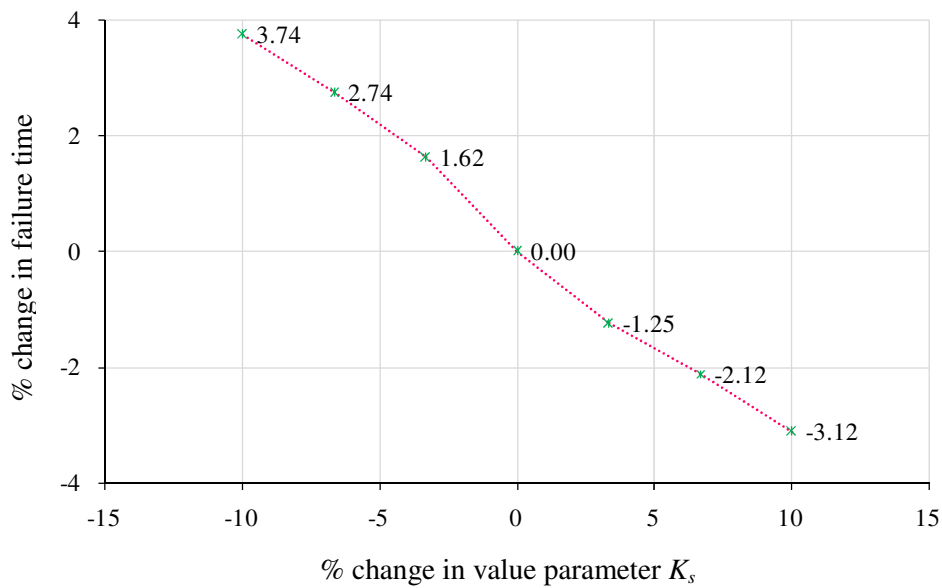


Figure 4.16 Sensitivity of dam stability to variation on  $K_s$  (two-phase seepage consideration)

Positions of almost all WCRs are closer to head reach than tail reach of the dam body. Earlier saturation of these WCRs in simulation (Figure 4.11 and 4.12) indicates that the head reach of the dam body saturated faster and tail reach saturated slower in simulation in comparison to experiment, in a given upstream discharge condition. It means upstream reservoir level rising

rate in simulation was faster than experiment. Since the dam body mass in head reach is dominant for the slope failure, numerically obtained slope failure will be earlier and shallower than experiment due to such phenomenon. However in the present study, numerically obtained failure surface was shallower only in side B. The friction on the side wall of the flume was ignored in the computation. Since the dam body contact area to the flume side wall was greater in side A than side B, the effect of friction in computation will be more significant in side A than that of side B, resulting deeper slip surface was computed in side A closer to the experimental one. Figure 4.15 presents three dimensional view of the failure surface computed by extended Spencer method considering two-phase flow.

Considering two-phase flow seepage analysis simulations were also carried out to analyze the sensitivity of dam body stability to  $K_s$  value parameter,  $K_s$  value was varied by  $\pm 10\%$ , so that its influence can be recognized. Figure 4.16 shows the % change in failure time of the dam body for % change in  $K_s$  value. Negative and positive values in % change in failure time represent respective earlier and delayed computed failure time with changed value of  $K_s$  comparison to predicted failure time when  $K_s$  value was not changed. The plot shows that increase in  $K_s$  value results rapid increase in moisture movement rate inside the dam body thereby increasing pore water pressure faster so that failure of the dam takes place earlier. Similarly, decrease in  $K_s$  value results the failure of the dam later.

The water level rising rate in upstream of the dam body depends on rate of moisture movement inside the dam. Saturated hydraulic conductivity  $K_s$  and the van Genuchten parameters ( $\alpha$  and  $\eta$ ), depends on the sand mix and its compaction, are the key parameters for guiding moisture movement and consequently failure time of the dam. It is difficult to ensure uniformity of sand mix and its compaction while determining these parameters and formation of experimental dam

Table 4.2 Summary of slope stability analysis

Simulation					Experiment
Seepage Analysis	Slope stability analysis method				
	Janbu's simplified		Extended Spencer		
	Failure time (sec)	$F_s$	Failure time (sec)	$F_s$	
One-phase	768	0.999	793	0.999	930
Two-phase	777	0.998	802	0.997	
One-phase (Awal, 2008)	770	0.991			

body. It is necessary to record the temporal variation of upstream reservoir level during experiment so that the value of these parameters can be optimized to get more accurate simulated reservoir level that may lead simulated moisture movement, dam body failure time and shape of the failure surface quite closer to the experimental one.

Since water-air two-phase flow model has been used to consider the air movement phenomenon inside the dam during seepage process, simulated moisture profiles obtained by the water-air two-phase seepage flow model are slightly delayed than that of conventional seepage flow model (Figure 4.5, 4.6, 4.8, 4.9, 4.11 and 4.12). Ultimately, failure time of the dam body has also found to be delayed in Janbu's simplified method as well as Spencer/extended Spencer method except in 2D steady discharge case.

Janbu's simplified method only satisfies force equilibrium for the entire sliding mass and assumes resultant interslice forces horizontal where as Spencer/extended Spencer method satisfies both the force and moment equilibrium and assumes resultant interslice forces are at some angle to the horizontal. Due to the vertical component of inclined interslice forces, calculated mobilized shear stress by the Spencer/extended Spencer method is less than that of Janbu's simplified method in a given condition of moisture content. Hence the factor of safety calculated by the Janbu's simplified method is less than that of Spencer/extended Spencer method, resulting the failure time of the dam body earlier in case of Janbu's simplified method.

## **Summary**

Analysis of landslide dam failure due to sudden sliding was carried out in two and three dimensions. Conventional water-phase as well as water-air two-phase seepage flow numerical simulation models are developed individually for seepage calculation inside the body of landslide dam. Seepage flow model is then combined with respective two and three dimensional transient slope stability model to predict the failure of dam due to sudden sliding. Janbu's simplified method as well as Spencer/extended Spencer method is incorporated into dynamic programming to locate the critical slip surface of a general slope of the dam. To evaluate the capability of the model, experimental results obtained by Awal (2008) were compared with the simulation results.

2D study was carried out with constant water head as well as steady water discharge in the upstream reservoir. In 3D study only steady water discharge was provided in the reservoir of the landslide dam. In all the cases, simulated and experimental moisture profiles are satisfactorily in agreement although results comparison shows some simulated results have faster moisture movement than that of experimental one and some have slower movement. Also the simulated failure shapes are matching satisfactorily with experimental failure shapes of all considered cases. However, results obtained by water-air two-phase seepage flow model and Spencer/extended Spencer method of slope stability analysis were observed slightly more closer to the experimental results than that of conventional seepage flow model and Janbu's simplified method of slope stability analysis.

## Chapter 5

### Conclusions and Recommendations

A numerical model was developed for the prediction of 3D failure surface of a slope due to a rainfall event and the time of failure. 3D conventional water-phase seepage flow model as well as the water-air two-phase seepage flow model calculates pore water pressure and moisture content within the body of the considered slope model. A 2D surface flow and erosion/deposition model calculates the surface water head of the runoff produced by the rainfall and erosion and deposition depths on the surface. The slope stability model calculates the factor of safety and the geometry of critical slip surface by utilizing the pore water pressure and moisture content obtained by seepage flow model.

2D and 3D numerical model was developed for the prediction of failure surface of a landslide dam when it fails by sudden sliding and the time of failure. As in the case of rainfall induced slope failure, a conventional water-phase seepage flow model as well as the water-air two-phase seepage flow model calculates pore water pressure and moisture content within the body of landslide dam. The slope stability model utilizes the pore water pressure and moisture content obtained from seepage flow model to compute the factor of safety and the geometry of critical slip surface of the dam.

#### 5.1 Conclusions

The conclusions of this study are summarized as follows:

##### **Analysis of rainfall induced slope failure**

The analysis of slope failure due to rainfall was carried out in 3D. The experiments were carried out on 23° and 28° flume slope. It is difficult to observe the three dimensional view of the failure surface in rectangular flume shape. So, the rectangular shape of the flume was modified to V-shape having cross slope of 20° in its bottom. The model slope was prepared on the rigid bed of flume by placing silica sand S6. Profile probes (PRs) consisting four sensors (SRs) were used to

measure the temporal variation of moisture content and pressure transducers (PTs) were used to measure the temporal variation of air pressure at different locations inside the body of the model slope. Measuring scales were placed in vertical position on the top surface of the model slope in its central longitudinal section for measuring the surface water forefront propagation. Downstream seepage outflow was measured by collecting outflow seepage water in a measuring cylinder. Red colored sediment strips and red colored cotton threads were placed respectively at the side wall faces and inside the body, normal to the flume bed, so as to measure the failure surface after sliding.

3D conventional water-phase seepage flow model as well as the water-air two-phase seepage flow model was coupled with a 2D surface flow and erosion/deposition model for the calculation of pore water pressure, pore air pressure and moisture content within the body of model slope as well as the downstream seepage out flow, surface water head of the runoff produced by the rainfall and erosion and deposition depths on the surface. The governing equations of seepage flow model were solved by line successive over relaxation (LSOR) scheme used by Freeze (1971a, 1971b, 1978) by an implicit iterative finite difference scheme. The finite difference form of the governing equations of surface flow and erosion/deposition model was obtained from the solution methods developed by Nakagawa (1989) using Leap-Frog scheme.

Limit equilibrium method of slices is widely used for slope stability analysis due to its simplicity and applicability. It usually involves two steps; one for the calculation of the factor of safety and the other for locating the most critical slip surface which yields the minimal factor of safety. In this study Janbu's simplified method as well as extended Spencer method was incorporated into an effective minimization procedure based on dynamic programming by which the minimal factor of safety and the corresponding critical non circular slip surface were determined simultaneously. Janbu's simplified method only satisfies force equilibrium for the entire sliding mass and assumes resultant inter-slice forces horizontal where as extended Spencer method satisfies both the force and moment equilibrium and assumes resultant inter-slice forces are at some angle to the horizontal. The slope stability model calculates the factor of safety and the geometry of critical slip surface according to the pore water pressure and moisture content obtained by seepage flow model.

The numerical simulation and experimental results of pore water pressure pore air pressure and moisture content within the body of model slope as well as the downstream seepage out flow,

surface water forefront propagation and predicted critical slip surface and time of failure of the model slope are in good agreement. However, results obtained by water-air two-phase seepage flow model and extended Spencer method of slope stability analysis were observed slightly delayed than that of conventional seepage flow model and Janbu's simplified method of slope stability analysis.

### **Analysis of landslide dam failure**

Analysis of landslide dam failure due to sudden sliding was carried out in two and three dimensions. Conventional water-phase as well as water-air two-phase seepage flow numerical simulation models are developed individually for seepage calculation inside the body of landslide dam. Seepage flow model is then combined with respective two and three dimensional transient slope stability model to predict the failure of dam due to sudden sliding. Janbu's simplified method as well as Spencer/extended Spencer method is incorporated into dynamic programming to locate the critical slip surface of a general slope of the dam. To evaluate the capability of the model, experimental results obtained by Awal (2008) were compared with the simulation results.

2D study was carried out with constant water head as well as steady water discharge in the upstream reservoir. In 3D study only steady water discharge was provided in the reservoir of the landslide dam. In all the cases, simulated and experimental moisture profiles are satisfactorily in agreement although results comparison shows some simulated results have faster moisture movement than that of experimental one and some have slower movement. Also the simulated failure shapes are matching satisfactorily with experimental failure shapes of all considered cases. However, results obtained by water-air two-phase seepage flow model and Spencer/extended Spencer method of slope stability analysis were observed delayed than that of conventional seepage flow model and Janbu's simplified method of slope stability analysis.

Saturated hydraulic conductivity ' $K_s$ ' is a key parameter for guiding the moisture profile and failure time of dam body which depends on the sand mix and its compaction. In 3D study, simulations were also carried out to analyze the sensitivity of dam body stability to  $K_s$  value parameter considering two-phase flow seepage analysis. The increase in  $K_s$  value resulted rapid increase in moisture movement rate inside the dam body thereby increasing pore water pressure

faster so that failure of the dam took place earlier. Similarly, decrease in  $K_s$  value resulted the failure of the dam later.

## **5.2 Recommendations for future researches**

Future researches are necessary to improve the performance of the model. The recommendations for future works are discussed here.

### **Analysis of rainfall induced slope failure**

- a) This study attempted to develop numerical model for the prediction of critical slip surface and the time of failure. However, it is also important to determine the distance moved by the failure mass and its shape and size after movement.
- b) The friction on the side wall of the flume was ignored in the proposed numerical model, which may have considerable effect in the geometry of the critical slip surface as well as the failure time of the model slope.
- c) In actual field, series of failures may occur in a slope due to a rainfall event. So, it is also necessary to carry out the experimental and numerical studies to investigate such failure mechanism in 3D.
- d) The effect of pore air flow in the soil slope is only considered in seepage flow analysis but not in slope stability analysis. The consideration of pore air pressure in the slope stability analysis will increase the safety factor of the soil due to the shear strength provided by it.
- e) The proposed numerical model was verified with limited laboratory experimental data. Field applications and more verification are necessary for its further improvement.
- f) The developed numerical models are deterministic. There are many uncertainties in soil properties of such as hydraulic conductivity, angle of friction, cohesion etc. So, probabilistic approach is necessary to overcome such uncertainties.

### **Analysis of landslide dam failure**

- a) This study attempted to develop 2D and 3D numerical model for the prediction of critical slip surface and the time of failure. However, it is also important to integrate 3D numerical model to 2D erosion/deposition model for prediction of resulting flood/debris flow hydrograph.

- b) The friction on the side wall of the flume was ignored in the proposed numerical model, which may have considerable effect in the geometry of the critical slip surface as well as the failure time of the dam body.
- c) The proposed numerical model was verified with limited laboratory experimental data. Field applications and more verification are necessary for its further improvement.
- d) The effect of pore air flow in the dam body is only considered in seepage flow analysis but not in slope stability analysis. The consideration of pore air pressure in the slope stability analysis will increase the safety factor of the dam body due to the shear strength provided by it.
- e) Landslide dam may also fail by progressive failure from toe. So, it is also necessary to develop numerical model that can treat such failure mechanism as well as the resulting flood/debris flow hydrograph.
- f) The developed numerical models are deterministic. There are many uncertainties in soil properties of such as hydraulic conductivity, angle of friction, cohesion etc. So, probabilistic approach is necessary to overcome such uncertainties.



## References:

- Affuso, A. M., Casagli, N., Dapporto, S., Gabbani, G., Gargini, A., and Rinaldi, M.: Monitoring and modelling of unsaturated flow and effects on streambank failures, in: Landslides research, theory and practice, edited by: Bromhead, E., Dixon, N., and Ibsen, M. L., *Proc. of eighth international symposium on landslides*, 26-30 June 2000, Cardiff, 2000.
- Aleotti, P., Polloni, G., Casagli, N., and Dapporto, S.: Shallow failures triggered by the November 2002 meteoric event in the Albaredo Valley, Valtellina (Italian Central Alps): mechanics and stability analyses, in: Landslides, Evaluation and Stabilization, edited by: Lacerba, W. A., Ehrlich, M., Fontoura, S. A. B., and Sayão, A. S. F., *Proc. of the ninth international symposium on landslides*, 28 June, 2 July, 2004, Rio de Janeiro, 2004.
- Anderson, M. G. and Howes, S.: Development and application of a combined soil water-slope stability model, *Quarterly Journal of Engineering Geology*, Vol.18, pp.225-236, 1985.
- Anderson, M. G. and Lloyd, D. M.: Using a combined slope hydrology/stability model to develop cut slope design charts, *Proc. Inst. Civil Engineers*, Vol.91, No.2, pp.705-718, 1991.
- Anderson, S.A. and Sitar, N.: Analysis of rainfall-induced debris flow, *Journal of Geotechnical Engineering*, ASCE, Vol.121, No.7, pp.544-552, 1995.
- Au, S.W.C.: Rainfall and slope failure in Hong Kong, *Engineering Geology*, Vol.36, pp.141-147, 1993.
- Awal, R.: Study on landslide dam failure due to sliding and overtopping, *Ph.D. Thesis*, Kyoto University, 2008.
- Awal, R., Nakagawa, H., Kawaike, K., Baba, Y. and Zhang, H.: An integrated approach to predict outflow hydrograph due to landslide dam failure by overtopping and sliding, *Annual Journal of Hydraulic Engineering*, JSCE, Vol.52, pp.151-156, 2008.
- Awal, R., Nakagawa, H., Kawaike, K., Baba, Y. and Zhang, H.: Three dimensional transient seepage and slope stability analysis of landslide dam, *Annals of Disaster Prevention Research Institute*, Kyoto University, No.52B, pp.689-696, 2009.
- Baker, R.: Determination of the critical slip surface in slope stability computations, *International Journal for Numerical and Analytical Methods in Geomechanics*, Vol.4, pp.333-359, 1980.
- Bardet, J.P. and Kapuskar, M.M.: A simplex analysis of slope stability, *Computers and Geotechnics*, Vol.8, pp.329-348, 1989.
- Baum, R.L., Savage, W.Z. and Godt, J.W.: TRIGRS - a Fortran program for transient rainfall infiltration and grid-based regional slope stability analysis, Virginia, *US Geological Survey*, Open file report 02-424, 2002.
- Bishop, A.W.: Progressive failure-with special reference to the mechanism causing it, *Proceedings of Geotechnical Conference*, Oslo, Norway, Vol.2, pp.142-150, 1967.
- Bishop, A.W.: The stability of tips and spoil heaps, *Quarterly Journal of Engineering Geology*, Vol.6, pp.335-376, 1973.
- Borga, M., Fontana, G.D., De Ros, D. and Marchi L.: Shallow landslide hazard assessment using a physically based model and digital elevation data, *Environmental Geology*, Vol.35, pp.81-88, 1998.
- Brand, E.W.: Landslides in Southeast Asia: a state of the art report, *In Proceedings of the 4<sup>th</sup> International Symposium on Landslides*, Toronto, Canada, Vol.1, pp.377- 384, 1984.

- Brand, E.W.: Some thoughts on rainfall induced slope failures, *Proceedings of 10<sup>th</sup> International Conference on Soil Mechanics and Foundation Engineering*, pp.373-376, 1981.
- Brenner, R.P., Tam, H.K. and Brand, E.W.: Field stress path simulation of rain-induced slope failure, *Proceedings of 11<sup>th</sup> International Conference on Soil Mechanics and Foundation Engineering*, Vol.2, pp.373-376, 1985.
- Bronstert, A.: Modellierung der Abflussbildung und der Bodenwasserdynamik von Hangen, *Universitat Karlsruhe*, 46 pp, 1994.
- Brooks, S. M. and Richards, K. S.: The significance of rainstorm variations to shallow translational hillslope failure, *Earth Surface processes and landforms*, Vol.19, No.1, pp.85-94, 1994.
- Bunza, G.: Investigation and monitoring of landslides with torrential significance in the Bavarian Alps. In: Bromhead, E., Dixon, N., Ibsen, M.L. (Eds.), *Landslides in research, theory and practice, Proceedings 8<sup>th</sup> International Symposium on Landslides*, 26-30 June, Cardiff., pp.195-202, 2000.
- Butler, D.R., Malanson, G.P., Oelfke, J.G.: Potential catastrophic flooding from landslide-dammed lakes, Glacier National Park, Montana, USA, *Zeitschrift fqr Geomorphologie*, Supplementband Neue Folge 83, pp.195-209, 1991.
- Cai, F., Ugai, K.: Numerical analysis of rainfall effects on slope stability, *International Journal of Geomechanics*, ASCE, Vol.4, No.2, 69-78, 2004.
- Caine, N.: The rainfall intensity-duration control of shallow landslides and debris-flows, *Geografiska Annaler*, Vol.62A, pp.23-27, 1980.
- Cannon, S.H. and Ellen, S.D.: Rainfall conditions for abundant debris avalanches in the San Francisco Bay region, California: *California Geology*, Vol.38, No.12, pp.267-272, 1985.
- Casagli, N., Dapporto, D., Ibsen, M. L., Tofani, V. and Vannocci, P.: Analysis of triggering mechanism during the storm of 20–21 Novembre 2000, in northern Tuscany, *Landslides*, Vol.3, No.1, 13-21, 2005.
- Casagrande, A.: On liquefaction phenomenon, *Ge´otechnique*, London, U.K., Vol.21, No.3, pp.197-202, 1971.
- Castro, G.: Liquefaction of sands, *PhD Thesis*, Harvard University, Cambridge, MA, 1969.
- Castro, G., Poulos, S.J.: Factors affecting liquefaction and cyclic mobility, *Journal of the Geotechnical Engineering Division*, ASCE, Vol.103, pp.501-516, 1977.
- Chatterjea, K.: Observations on the fluvia and slope processes in Singapore and their impact on the urban environment, *Ph.D Thesis*, National University of Singapore, 1989.
- Chen, J., Hopmans, J. W. and Grismer, M. E.: Parameter estimation of two-fluid capillary pressure-saturation and permeability functions, *Advances in Water Resources*, Vol. 22, No.5, pp.479-493, 1999.
- Cho, S.E. and Lee, S.R.: Instability of unsaturated soil slopes due to infiltration, *Computers and Geotechnics*, Vol.28, pp.185-208, 2001.
- Collins, B. D. and Znidarcic, D.: Stability analyses of rainfall induced landslides, *J. Geotechnical Geoenvironmental Eng.*, Vol.130, pp.362-372, 2004.
- Copal Electronics: Pressure transducer with amplifier PA-850, *Copal Electronics*, 2007.

- Corominas, J.: Landslides and Climate, *Keynote Lectures from the 8th International Symposium on Landslides*, Vol.4, pp.1-33, 2001.
- Costa, J.E., Schuster, R.L.: Documented historical landslide dams from around the world, *Open-File Report* (United States Geological Survey), pp.91-239, 1991.
- Crosta, G.: Regionalization of rainfall thresholds: an aid to landslide hazard evaluation, *Environmental Geology*, Vol.35, pp.2-3, 1998.
- Crosta, G. B. and Dal Negro, P.: Observations and modelling of soil slip-debris flow initiation processes in pyroclastic deposits: the Sarno 1998 event, *Nat. Hazards Earth Syst. Sci.*, Vol.3, pp.53-69, 2003.
- Crosta, G.B. and Frattini, P.: Distributed modeling of shallow landslides triggered by intense rainfall, *Nat Haz Earth Syst Sci*, Vol.3, pp.81-93, 2003.
- Crozier, M. J.: Landslides: Causes, Consequences and Environment, *Croom Helm*, London, pp.252, 1986.
- Crozier, M. J.: 'Landslide hazard assessment: a review of papers presented to theme G4', in Bell, D. (Ed.), *Landslides, Proceedings of Sixth International Symposium on Landslides Christchurch*, 10-14 February 1992, Vol.3, Balkema, Rotterdam, pp.1843-1848, 1995.
- Crozier, M. J.: Prediction of rainfall-triggered landslides: a test of the Antecedent Water Status Model, *Earth Surface Processes and Landforms*, Vol.24, pp.825-833, 1999.
- Cruden, D.M.: A simple definition of a landslide, *Bulletin of the International Association of Engineering Geology*, No.43, 27-29, 1991.
- Dakshanamurthy, V., Fredlund, D.G. and Rahardjo, H.: Coupled three-dimensional consolidation theory of unsaturated porous media, *Proceedings of the fifth international conference on expansive soils*, Adelaide, South Australia, pp.99-103, 1984.
- Dam, J.C. van and Feddes, R.A.: Numerical simulation of infiltration, evaporation and shallow groundwater levels with the Richards equation, *Journal of Hydrology*, Vol.233, pp72-85, 2000.
- Davies, T.R., Manville, V., Kunz, M. and Donadini, L.: *Modeling landslide dambreak flood magnitudes: case study*, *Journal of Hydraulic Engineering*, Vol.133, No.7, pp.713-720, 2007.
- Davies, T.R.H.: Landslide-dambreak floods at Franz Josef Glacier township, Westland, New Zealand: a risk assessment, *Journal of Hydrology New Zealand*, Vol.41, pp.1-17, 2002.
- Davies, T.R.H., Scott, B.K.: Dambreak flood hazard from the Callery River, Westland, New Zealand, *Journal of Hydrology New Zealand*, Vol.36, pp.1-13, 1997.
- Day, P. R. and Luthin, J. N.: A numerical solution of the differential equation of flow for a vertical drainage problem, *Proceedings*, Soil Science Society of America, Vol. 20, pp. 443-447, 1956.
- Delta-T Devices Ltd.: Profile Probe type PR2, Advanced technology soil moisture sensor for monitoring and irrigation control, *Delta-T Devices Ltd.*, Quick Start Guide Version 1.0, 2004a.
- Delta-T Devices Ltd.: User manual for the profile probe type PR2, *Delta-T Devices Ltd.*, User Manual Version: PR2-UM-2.0, 2004b.
- Daiki Rika Kogyo Co., Ltd.: Daiki soil & moisture DIK-3422 multi-fold pF meter, <http://www.daiki.co.jp/PDF/3422.PDF>.
- D'Odorico, P., Fagherazzi, S. and Rigon, R.: Potential for landsliding: dependence on hyetograph characteristics, *J Geophys Res Earth Surf* 110(F1), 2005.

- Eckersley, J.D.: Flow slides in stockpiled coal, *Engineering Geology*, Vol.22, pp.13-22, 1985.
- Eckersley, J.D.: The institution and development of slope failures with particular reference to flow slides, *PhD thesis*, James Cook University of North Queensland, 1986.
- Ev-K2-CNR, Pakistan Representative Office: Executive summary on Attabad landslide survey in Hunza, *Ev-K2-CNR Committee Via San Bernardino*, 14524126 Bergamo, Italy, 7-17 April 2010.
- Fang, J., Kawasaki, A. and Sadohara, S.: The development of the slope failure management system, *Research in Urban Earthquake Disaster Mitigation*, Vol.1, 2003.
- Finlay, P. J., Fell, R. and Maguire, P. K.: The relationship between the probability of landslide occurrence and rainfall, *Canadian Geotechnical Journal*, Vol.34, No.6, 811-824, 1997.
- Frattoni, P., Crosta, G.B., Fusi, N. and Negro, P.D.: Shallow landslides in pyroclastic soil: a distributed modeling approach for hazard assessment, *Engineering Geology*, Vol.73, pp.277-295, 2004.
- Fread D.: The NWS dambrk model: theoretical background/user documentation, *National Weather Service*, NOAA: Silver Spring, Maryland, 1991.
- Fredlund, D.G. and Rahardjo, H.: Soil mechanics for unsaturated soils, *John Wiley and Sons Inc.*, 517, 1993.
- Fredlund, D.G., Morgenstern, N.R. and Widger, R.A.: The shear strength of unsaturated soils, *Canadian Geotechnical Journal*, Vol.15, pp.313-321, 1978.
- Freeze, R.A.: The mechanism of natural groundwater recharge and discharge 1. One-dimensional, vertical, unsteady, unsaturated flow above a recharging and discharging groundwater flow system, *Water Resources Research*, Vol.5, pp.153-171, 1969.
- Freeze, R.A.: Three dimensional transient, saturated unsaturated flow in a groundwater basin, *Water Resources Research*, Vol.7, pp.347-366, 1971a.
- Freeze, R.A.: Influence of the unsaturated flow domain on seepage through earth dams, *Water Resources Research*, Vol.7, pp.929-941, 1971b.
- Freeze, R. A.: Mathematical models of hillslope hydrology, in Kirkby, M. J., ed., *Hillslope Hydrology*, John Wiley, pp. 177-225, 1978.
- Fukuzono, T.: Experimental study of slope failure caused by heavy rainfall, Erosion and Sedimentation in the Pacific Rim, *Proceedings of the Corvallis Symposium*, August, 1987.
- Gasmo, J.M., Rahardjo, H. and Leong, E.C.: Infiltration effects on stability of a residual soil slope, *Computers and Geotechnics*, Vol.26, pp.145-165, 2000.
- Geo-Slope: SEEP/W model and User manual 2000, *Geo-Slope International*, 2003a.
- Geo-Slope: SLOPE/W model and User manual 2000, *Geo-Slope International*, 2003b.
- Giuseppetti, G. and Molinaro, P.: A mathematical model of the erosion of an embankment dam by overtopping, *Proceedings of International Symposium on analytical evaluation of dam related safety problems*, Copenhagen, 1989.
- Glade, T., Crozier, M., and Smith, P.: Applying Probability Determination to Refine Landslide-triggering Rainfall Thresholds Using an Empirical "Antecedent Daily Rainfall Model", *Pure Appl. Geophys.*, Vol.157, pp.1059-1079, 2000.

- Govi, M. and Sorzana, P. F.: Landslides susceptibility as a function of critical rainfall amount in Piedmont Basins, *Studia Geomorphologica Carpatho-Balcanica*, Vol.14, pp.43-61, 1980.
- Griffiths, D.V. and Lu, N.: Unsaturated slope stability analysis with steady infiltration or evaporation using elasto-plastic finite elements, *Int. J. Numer. Anal. Meth. Geomech.*, Vol.29, pp.249-267, 2005.
- Guzzetti, F., Malamud, B.D., Turcotte, D.L., Reichenbach, P.: Power-law correlations of landslide areas in central Italy, *Earth and Planetary Science Letters*, Vol.195, 169-183, 2002.
- Hanisch, J.: Usoi landslide dam in Tajikistan-the world's highest dam. First stability assessment of the rock slopes at Lake Sarez. In: Rybar, J., Stemberk, J., Wagner, P. (Eds.), *Landslides, Proceedings 1<sup>st</sup> European Conference on Landslides*, 24-26 June 2002, Prague, Balkema, Rotterdam, pp.189-192, 2002.
- Hird, H.H. and Hassona, F.A.K.: Some factors affecting the liquefaction and flow of saturated sands in laboratory tests, *Engineering Geology*, Vol.28, pp.149-170, 1990.
- Horiuchi, S., Akanuma, J., Ogawa, K., Kuraoka, S., Sugiyama, M., Morita, T., Itoh, T., Mizuyama, T.: Hydraulic model tests for debris flow due to break of a small natural landslide dam, Interparaevent 2010, *International Symposium in Pacific Rim*, Taipei, Taiwan, pp.157-167, 2010.
- Ishihara, K.: Liquefaction and flow failure during earthquakes, *Geotechnique*, Vol.43, No.3, pp.349-451, 1993.
- Ishihara, K., Okusa, S., Oyagi, N. and Ischuk, A.: Liquefaction induced flow slide in the collapsible loess deposit in Soviet Tajik, *Soils and Foundations*, Vol.30, No.4, pp.73-89, 1990.
- Iverson, R. M.: Landslide triggering by rainfall infiltration, *Water Resources Research*, Vol.36, pp.1987-1910, 2000.
- Jakob, M. and Weatherly, H.: A hydroclimatic threshold for landslide initiation on the North Shore Mountains of Vancouver, British Columbia, *Geomorphology*, Vol.54, pp.137-156, 2003.
- Jiang, J.C. and Yamagami, T.: Three-dimensional slope stability analysis using an extended Spencer method, *Soils and Foundations*, Japanese Geotechnical Society, Vol.44, No.4, pp.127-135, 2004.
- Johnson, K. A. and Sitar, N.: Hydrologic conditions leading to debris-flow initiations, *Canadian Geotechnical Journal*, Vol.27, pp.789-801, 1990.
- Kees, E. and Miller T.: Higher order time integration methods for two-phase flow, *Advances in Water Resources*, Vol.25, pp.159-177, 2002.
- Keim, R.F. and Skaugset, A.E.: Modelling effects of forest canopies on slope stability, *Hydrol Process*, Vol.17, Vol.1457-1467, 2003.
- Kim, S. K., Hong, W. P., and Kim, Y. M.: Prediction of rainfall-triggered landslides in Korea, in: *Proceedings of the 6th International Symposium on Landslides*, edited by: Bell, D. H., Christchurch, New Zealand, Balkema, Rotterdam, pp.989-994, 1991.
- Kirkby, M.J.: Hillslope Hydrology, *John Wiley & Sons*, 389 pp., 1978.
- Ko Ko, C., Flentje, P., and Chowdhury, R.: Interpretation of probability of landsliding triggered by rainfall, *Landslides*, Springer-Verlag, Vol.1, pp.263-275, 2004.
- Korup, O.: Recent research on landslide dams - a literature review with special attention to New Zealand, *Progress in Physical Geography*, Vol.26, pp.206-235, 2002.

- Lan, H.X., Lee, C.F., Zhou, C.H. and Martin, C.D.: Dynamic characteristics analysis of shallow landslides in response to rainfall event using GIS, *Environmental Geology*, Vol.47, pp.254-267, 2005.
- Laroche, C. and Vizika, O.: Two-phase flow properties prediction from small-scale data using pore network modeling, *Transport in Porous Media*, Vol.61, pp.77-91, 2005.
- Leong, E.C. and Rahardjo, H.: Review of soil-water characteristic curve equations, *Journal of Geotechnical and Geo-environmental Engineering*, Vol.123, No.12, pp.1106-1117, 1997.
- Li, M.H., Hsu, M.H., Hsieh, L.S., Teng, W.H.: Inundation potentials analysis for Tsao-Ling landslide lake formed by Chi- Chi earthquake in Taiwan, *Natural Hazards*, Vol. 25, pp.289-303, 2002.
- Liu, N.: the experience on carrying out the mitigation measures for relieving the large-scale landslide damming river hazard, taking the Tangjiashan landslide and the Yigong landslide event for examples, *Ministry of Water Resource of People's Republic of China*, 2008 (Poster).
- Lumb, P.: Slope failures in Hong Kong, *Quarterly Journal of Engineering Geology*, Vol.8, pp.31-65, 1975.
- Macchione, F. and Sirangelo, B.: Study of earth dam erosion due to overtopping, *Proceedings of technical conference of hydrology of disasters*, WMO, Ginevra, 1988.
- Mizuyama, T.: Countermeasures to cope with landslide dams – prediction of the outburst discharge, *Proc. of 6th Japan-Taiwan Joint Seminar on Natural Disaster Mitigation*, 2006.
- Mizuyama, T., Satofuka, Y., Ogawa, K. and Mori, T.: Estimating the outflow discharge rate from landslide dam outbursts, *Proceedings of the INTERPRAEVENT International Symposium on Disaster Mitigation of Debris Flows, Slope Failures and Landslides*, Vol.1, pp.365-377, 2006.
- Mizuyama T., Tabata,S., Mori T., Watanabe F. and Inoue K.: Outburst of Landslide dams and their prevention, Internationales Symposium, INTERPRAEVENT 2004-RIVA/TRIENT, IV, pp.221-229, 2004.
- Montgomery, D.R. and Dietrich, W.E.: A physically based model for the topographic control on shallow landslide, *Water Resources Research*, Vol.30, pp.83-92, 1994.
- Morita, T., Sakaguchi, T., Sawa, Y., Mizuyama, T., Satofuka, Y., Ogawa, K., Usuki, N. and Yoshino, K.: Method of estimation for flood discharges caused by overflow erosion of landslide dams and its application in as a countermeasure, Interparaevent 2010, *International Symposium in Pacific Rim*, Taipei, Taiwan, pp.293-302, 2010.
- Moriwaki, H., Inokuchi, T., Hattanji, T., Sassa, K., Ochiai, H. and Wang, G.: Failure processes in a full-scale landslide experiment using a rainfall simulator, *Landslides*, Vol.1, pp.277-288, 2004.
- Mukhlisin, M. and Taha, M.R.: Slope Stability Analysis of a Weathered Granitic Hillslope as Effects of Soil Thickness, *European Journal of Scientific Research*, Vol.30, No.1, pp.36-44, 2009.
- Nakagawa, H.: Study on risk evaluation of flood and sediment inundation disaster, *Doctoral Thesis*, Kyoto University, 1989 (in Japanese).
- Nakagawa, H., Takahashi, T., Satofuka, Y. and Kawaike, K.: Numerical simulation of sediment disasters caused by heavy rainfall in Camuri Grande basin, Venezuela 1999, *Proceedings of the Third Conference on Debris-Flow Hazards Mitigation: Mechanics, Prediction, and Assessment*, Switzerland, Rotterdam, pp.671-682, 2003.

- Ng, C.W.W. and Shi, Q.: A numerical investigation of the stability of unsaturated soil slopes subjected to transient seepage, *Computers and Geotechnics*, Vol.22, No.1, pp.1-28, 1998.
- Okata, K., Sugiyama, T., Muraishi, H., Noguchi, T., and Samizo, M.: Statistical risk estimating method for rainfall on surface collapse of a cut slope, *Soils Foundation*, Vol.34, No.3, pp.49-58, 1994.
- Oostrom, M. and Lenhard, R.: Comparison of relative permeability-saturation-pressure parametric models for infiltration and redistribution of a light non-aqueous phase liquid in sandy porous media, *Advances in Water Resources*, Vol.21, No.2, pp.145-157, 1998.
- Pasuto, A. and Silvano, S.: Rainfall as a trigger of shallow mass movements - A case of study in the Dolomites, Italy, *Environmental Geology*, Vol.35, No.2-3, pp.184-189, 1998.
- Pitts, J.: An investigation of slope stability on the NTI campus, Singapore, *Applied Research project RPI/83*, Nanyang Technological Institute, Singapore, 1985.
- Pradel, D., and Raad, G.: Effect of permeability on surficial stability of homogeneous slopes, *Journal of Geotechnical Engineering*, Vol.119, No.2, pp.315-332, 1993.
- Rahardjo, H., Leong, E.C., Casmo, J.M. and Tang S.K.: Assessment of rainfall effects on stability of residual soil slopes, *In Proceedings of 2<sup>nd</sup> Int. Conf. on Unsaturated Soils*, Beijing, China, Vol.1, pp.280-285, 1998.
- Rahardjo, H., Lim, T.T., Chang, M.F. and Fredlund, D.G.: Shear strength characteristics of a residual soil, *Canadian Geotechnical Journal*, Vol.32, pp.60-77, 1995.
- Rahardjo, H., Li, X.W., Toll, D.G., and Leong, E.C.: The effect of antecedent rainfall on slope stability, *Geotechnical and Geological Engineering*, Vol.19, pp.371-399, 2001.
- Richards, L.A.: Capillary conduction of liquids in porous mediums, *Physics*, Vol.1, pp.318-333, 1931.
- Rinaldi, M., Casagli, N., Dapporto, S., and Gargini, A.: Monitoring and modelling of pore water pressure changes and riverbank stability during flow events, *Earth Surface Processes and Landforms*, Vol.29, pp.237-254, 2004.
- Risley, J., Walder, J. and Denlinger, R.: Usoid dam wave overtopping and flood routing in the Bartang and Panj Rivers, Tajikistan, *U.S. Geological Survey Water-Resources Investigations Report 03-4004*, pp.28, 2006.
- Sanderson, F., Bakkehoi, S., Hestenes, E., and Lied, K.: The influence of meteorological factors on the initiation of debris flows, rockfalls, rockslides and rockmass stability, in: *Landslides. Proceedings 7<sup>th</sup> International Symposium on Landslides*, edited by: Senneset, K., A.A. Balkema, 1996.
- Sarkar, S., Bonnard, C., Noverraz, F.: Risk assessment of potential landslide dams in the valleys of La Veveyse and Veveyse de Fegire, Switzerland. In: Bromhead, E., Dixon, N., Ibsen, M.L. (Eds.), *Proceedings 8<sup>th</sup> International Symposium on Landslides*, 26-30 June, Cardiff, Landslides in Research, Theory and Practice, pp.1309-1314, 2000.
- Sassa, K.: The mechanism starting liquefied landslides and debris flows, *Proceedings of 4<sup>th</sup> International Symposium on Landslides*, Toronto, Canada, vol.2, pp.349-354, 1984.
- Sassa, K.: Mechanisms of landslide triggered debris flow. In: Sassa, K. (Ed.), "Environmental Forest Science", *Proceedings of IUFRO Div. 8 Conference*, Kluwer Academic Publishing, Kyoto, pp.471-490, 1998b.
- Sassa, K.: Prediction of earthquake induced landslides, *Special Lecture of 7<sup>th</sup> International Symposium on Landslides*, "Landslides", vol.1, pp.115-132, 1996.

- Sassa, K.: Recent urban landslide disasters in Japan and their mechanisms, *Proc. 2<sup>nd</sup> International Conference on Environmental Management*, ‘‘Environmental Management’’, vol.1, pp.47-58, 1998a.
- Sassa, K.: Analysis on slope stability: I, Mainly on the basis of the indoor experiments using the standard sand produced in Toyoura, Japan, *Journal of the Japan Society of Erosion Control Engineering*, Vol.25, No.2, pp.5-17, 1972 (in Japanese with English abstract).
- Sassa, K.: Analysis on slope stability: II, Mainly on the basis of the indoor experiments using the standard sand produced in Toyoura, Japan, *Journal of the Japan Society of Erosion Control Engineering*, Vol.26, No.3, pp.8-19, 1974 (in Japanese with English abstract).
- Satofuka, Y., Mori, T., Mizuyama, T., Ogawa, K., and Yoshino, K.: Prediction of floods caused by landslide dam collapse, *Journal of Disaster Research*, Vol.5, No.3, pp.288-295, 2010.
- Schuster, R.L. and Wieczorek, G. F.: Landslide triggers and types, *Proceedings of the First European Conference on Landslides*, A.A. Balkema Publishers, pp.59-78, 2002.
- Schuster, R.L., Wieczorek, G.F. and Hope, II, D.G.: Landslide dams in Santa Cruz County, California, resulting from the earthquake, *U.S. Geological Survey Professional Paper 1551-C*, pp.51-70, 1998.
- Seed, H.B.: Landslides during earthquakes due to soil liquefaction, *Journal of the Soil Mechanics and Foundations Division*, ASCE, Vol.94, No.5, pp.1055-1122, 1966.
- Seed, H.B.: Soil liquefaction and cyclic mobility evaluation for level ground during earthquakes, *Journal of the Geotechnical Engineering Division*, ASCE, Vol.105, pp.201-255, 1979.
- Sharma, R.H.: Study on integrated modeling of rainfall induced sediment hazards, *Doctoral Thesis*, Kyoto University, 2006.
- Sidle, R. C. and Dhakal, A. S.: Potential effects of environmental change on landslide hazards in forest environments, in: *Environmental Change and Geomorphic Hazards in Forests*, edited by: Sidle, R. C., *IUFRO Research Series*, No. 9, pp. 123-165, CAB International Press, Oxen, UK, 2002.
- Sidle, R.C. and Swanston, D.N.: Analysis of a small debris slide in coastal Alaska, *Canadian Geotechnical Journal*, Vol.19, pp.167-174, 1982.
- Sitar, N., Anderson, S.A. and Johnson, K.A.: Conditions leading to the initiation of rainfall-induced debris flows, *Proceedings of the Journal of the Geotechnical Engineering Division Specialty Conference on Stability and Performance of Slopes and Embankments-II*, ASCE, New York, NY, pp.834-839, 1992.
- Sugiyama, T., Okata, K., Muraishi, H., Noguchi, T., and Samizo, M.: Statistical rainfall risk estimating method for a deep collapse of a cut slope, *Soils Foundation*, Vol.35, No.4, pp.37-48, 1995.
- Suzuki, H., and Matsuo, M.: Procedure of slope failure prediction during rainfall based on the back analysis of actual case records, *Soils Foundation*, Vol.28, No.3, pp.51-63, 1988.
- Takahama, J., Fujita, Y. and Kondo, Y.: Study on analysis method for migration from debris flow to hyperconcentrated flow, *Journal of Hydrosience and Hydraulic Engineering*, Vol.44, pp.683-686, 2000. (In Japanese with English abstract)
- Takahashi T.: Debris flow, Monograph Series of IAHR, *Balkema*, pp.1-165, 1991.
- Takahashi, T. and Nakagawa, H.: Flood/debris flow hydrograph due to collapse of natural dam by overtopping, *Journal of Hydrosience and Hydraulic Engineering*, JSCE, Vol.12, No.2, pp.41-49, 1994.

- Takahashi, T. and Kuang, S. F.: Hydrograph prediction of debris flow due to failure of landslide dam, *Annals Disaster Prevention Research Institute*, Kyoto Univ., No.31, B-2, pp.601-615, 1988.
- Terlien, M. T. J.: Modelling spatial and temporal variations in rainfall-triggered landslides. *ITC Publ. 32*, Enschede, Netherlands, 50 pp, 1996.
- Terlien, M. T. J.: The determination of statistical and deterministic hydrological landslide-triggering thresholds, *Environmental Geology*, Vol.35, pp.2-3, 1998.
- Terzaghi, K.: Mechanism of landslides, In: Paige, S. (Ed.), Application of Geology to Engineering Practice (Berkey Volume), *Geological Society of America*, New York, pp.83-123, 1950.
- Terzaghi, K.: Varieties of submarine slope failures, *Proceedings of 8th Texas Conference on Soil Mechanics and Foundation Engineering*, University of Texas, Austin, pp.1-41, 1956.
- Tohari, A., Nishigaki, M. and Komatsu, M.: Laboratory rainfall-induced slope failure with moisture content measurement, *ASCE Journal of Geotechnical and Geoenvironmental Engineering*, Vol.133, No.5, pp.575-587, 2007.
- Toll, D.G.: Rainfall-induced landslides in Singapore, Proc. Institution of Civil Engineers, *Geotechnical Engineering*, Vol.149, No.4, pp.211-16, 2001.
- Touma, J. and Vauclin, M.: Experimental and numerical analysis of two-phase infiltration in a partially saturated soil, *Transport in Porous Media*, Vol.1, pp.27-55, 1986.
- Tsai, T.L.: The influence of rainstorm pattern on shallow landslide, *Environmental Geology*, 2007.
- Tsai, T.L., Chen, H.E. and Yang, J.C.: Numerical modeling of rainstorm-induced shallow landslides in saturated and unsaturated soils, *Environmental Geology*, Vol.55, pp.1269-1277, 2008.
- Tsai, T.L. and Yang, J.C.: Modeling of rainfall-triggered shallow landslide, *Environmental Geology*, Vol.50, No.4, pp.525-534, 2006.
- Tsaparas, I.: Field Measurements and Numerical Modelling of Infiltration and Matric Suctions within Slopes, *Ph.D Thesis*, University of Durham, 2002.
- Tsutsumi, D. and Fujita, M.: Relative importance of slope material properties and timing of rain fall for the occurrence of landslides, *International Journal of Erosion Control Engineering*, Vol.1, No.2, 2008.
- Van Asch, T. W. J., Buma, J., and Van Beek, L. P. H.: A view on some hydrological triggering systems in landslides, *Geomorphology*, Vol.30, pp.25-32, 1999.
- Van Dijke, M. I. J., Van Der Zee, S. E. A. T. M. and Van Duijn, C. J.: Multi-phase flow modeling of air sparging, *Advances in Water Resources*, Vol.18, No.6, pp.319-333, 1995.
- van Genuchten, M. T.: A closed-form equation for predicting the hydraulic conductivity of unsaturated soils, *Soil Science Society of America Journal*, Vol.44, No.5, pp.892-898, 1980.
- Varnes, D. J.: Landslide Hazard Zonation: a review of principles and practice, Natural Hazards Series, 3, UNESCO, Paris, 63 pp., 1984.
- Vasconcellos, C. A. B. de and Amorim, J. C. C.: Numerical simulation of unsaturated flow in porous media using a mass conservative model, em "*Proceeding of COBEM. 2001, Fluid Mechanics*", Vol.8, pp.139-148, Uberlândia, MG, 2001.

- Wang, G. and Sassa, K.: Pore-pressure generation and movement of rainfall-induced landslides; effects on grain size and fine-particle content, *Journal of Engineering Geology*, Vol.69, pp.109-125, 2003.
- Wieczorek, G. F.: Landslide triggering mechanisms, in: Landslides Investigation and Mitigation, edited by: Turner, A. K. and Schuster, R. L., special report 247, *National Academy Press*, Washington D.C., 1996.
- Wieczorek, G. F.: Effect of rainfall intensity and duration on debris flows in central Santa Cruz Mountains, California, *Geolog. Soc. Amer.*, Reviews in Engineering Geology, Vol.7, 1987.
- Wilkinson, P.L., Anderson, M.G. and Lloyd, D.M.: An Integrated hydrological model for rain induced landslide prediction, *Earth Surface Processes and Landforms*, Vol.27, pp.1285-1297, 2002.
- Wolle C.M. and Hachichi, W.: Rain-induced landslides in southeastern Brazil, *In Proceedings of the 12th International Conf. on Soil mechanics and Foundation Engineering*, Rio de Janeiro, pp.1639-1642, 1989.
- Wu, W. and Slide, R.C.: A distributed slope stability model for steep forested basins, *Water Resources Research*, Vol.31, pp.2097-2110, 1995.
- Xu, Q., Fan, X.M., Huang, R.Q. and Westen, C.V.: Landslide dams triggered by the Wenchuan Earthquake, Sichuan Province, south west China, *Bull Eng Geol Environ*, Vol.68, pp.373-386, 2009.
- Yamagami, T. and Jiang, J.-C.: A search for the critical slip surface in three-dimensional slope stability analysis, *Soils and Foundations*, Vol.37, No.3, pp.1-16, 1997.
- Yamagami, T. and Ueta, Y.: Noncircular slip surface analysis of the stability of slopes: An application of dynamic programming to the Janbu method, *Journal of Japan Landslide Society*, Vol. 22, No.4, pp.8-16, 1986.
- Yan, J., Cao, Z., Liu, H., Chen, L.: Experimental study of landslide dam-break flood over erodible bed in open channels, *Journal of Hydrodynamics*, Science direct, Vol.21, No.1, pp.124-130, 2009.
- Zhang, X., Zhu, Y., Fang, C. and Chen, S.: Numerical Simulation of water-air two-phase flow in soil slope under water level rise condition, *Journal of Natural Sciences*, Vol.14, No.5, pp.442-446, 2009.

## List of Figures

- Figure 1.1 Helicopter view of the artificial spillway in the Tangjiashan landslide dam (3)
- Figure 1.2 Impounded water flowing through the artificial spillway, taken at 11:00 (Beijing time) 10 June 2008 when the discharge reached its maximum (3)
- Figure 1.3 Hunza landslide dam in Pakistan (4)
- Figure 1.4 View of the lake from the upper side of the Hunza landslide dam (4)
- Figure 1.5 Slope failure in Krishnabhir in 2000 (5)
- Figure 1.6 Krishnabhir in 2006, after the bio-engineered slope stabilisation (5)
- Figure 1.7 Slope failure due to torrential rainfall of the Bai-u front (Minamata City, Kumamoto Prefecture, July 1997) (6)
- Figure 1.8 Slope failure due to torrential rainfall of the Bai-u front (Hanakura Area, Kagoshima City, Kagoshima Prefecture August 6, 1993) (6)
- Figure 1.9 Slope failure in Uenoyama Area in Kozushima Village (July 2000, Kozushima Village, Tokyo) (6)
- 
- Figure 2.1 Experimental setup (18)
- Figure 2.2 Multi-fold pF meter (19)
- Figure 2.3  $\theta_w-h_w$  relationship curve for silica sand S6 (20)
- Figure 2.4 Grain size distribution of the sediment (20)
- Figure 2.5 Profile probe type PR2 (21)
- Figure 2.6 Typical calibration curve for a sensor of profile probe PR2 (22)
- Figure 2.7 Pressure transducers (22)
- Figure 2.8 Point gauge (23)
- Figure 2.9 Model slope with the arrangement of SRs, PTs and surface water forefront measurement scales (Flume slope 23°) (24)
- Figure 2.10 Model slope with the arrangement of SRs, PTs and surface water forefront measurement scales (Flume slope 28°) (25)
- Figure 2.11 Picture showing the position of measuring scales for surface water forefront propagation (23° flume slope) (25)
- Figure 2.12 Typical sketches showing the alignment of threads/sand strips before and after the failure of slope in a particular L-section (26)
- Figure 2.13 Distribution of rainfall intensity (in mm/hr) over the flume (27)
- Figure 2.14 Water content profiles observed in experiment (23° flume slope) (27)

- Figure 2.15 Water content profiles observed in experiment (28° flume slope) (28)
- Figure 2.16 Air pressure head profiles observed in experiment (23° flume slope) (28)
- Figure 2.17 Air pressure head profiles observed in experiment (28° flume slope) (28)
- Figure 2.18 Seepage Outflow observed in experiment (23° flume slope) (28)
- Figure 2.19 Seepage Outflow observed in experiment (28° flume slope) (28)
- Figure 2.20 Observed slope sliding (23° flume slope - Experiment D) (29)
- Figure 2.21 Observed slope sliding (23° flume slope - Experiment E) (30)
- Figure 2.22 Observed slope sliding (28° flume slope) (30)
- Figure 2.23 Alignment of failure plane in a particular L-section within the body of a model slope (31)
- 
- Figure 3.1 Hydraulic variables arrangement on meshes (41)
- Figure 3.2 Hydraulic variables arrangement and calculation methodology (42)
- Figure 3.3 Simulated and experimental moisture content profiles (23° flume slope) (46)
- Figure 3.4 Simulated and experimental moisture content profiles (28° flume slope) (47)
- Figure 3.5 Simulated and experimental air pressure head profiles (23° flume slope) (48)
- Figure 3.6 Simulated and experimental air pressure head profiles (28° flume slope) (48)
- Figure 3.7 Moisture counter at longitudinal section through centre line (23° flume slope) (50)
- Figure 3.8 Moisture counter at cross section through PR1 (23° flume slope) (51)
- Figure 3.9 Moisture counter at cross section through PR2 (23° flume slope) (52)
- Figure 3.10 Moisture counter at cross section through PR3 (23° flume slope) (53)
- Figure 3.11 Moisture counter at longitudinal section through centre line (28° flume slope) (54)
- Figure 3.12 Moisture counter at cross section through PR1 (28° flume slope) (55)
- Figure 3.13 Moisture counter at cross section through PR2 (28° flume slope) (56)
- Figure 3.14 Moisture counter at cross section through PR3 (28° flume slope) (57)
- Figure 3.15 Air pressure head counter at longitudinal section through centre line (23° flume slope) (58)
- Figure 3.16 Air pressure head counter at cross section through PT1 (23° flume slope) (58)
- Figure 3.17 Air pressure head counter at cross section through PT2 (23° flume slope) (59)
- Figure 3.18 Air pressure head counter at cross section through PT3 (23° flume slope) (59)
- Figure 3.19 Air pressure head counter at longitudinal section through centre line (28° flume slope) (60)
- Figure 3.20 Air pressure head counter at cross section through PT1 (28° flume slope) (60)
- Figure 3.21 Air pressure head counter at cross section through PT2 (28° flume slope) (61)

- Figure 3.22 Air pressure head counter at cross section through PT3 (28° flume slope) (61)
- Figure 3.23 Surface water front on the soil surface at longitudinal section through centre line (23° flume slope) (62)
- Figure 3.24 Surface water front on the soil surface at longitudinal section through centre line (28° flume slope) (63)
- Figure 3.25 Seepage Outflow (23° flume slope) (64)
- Figure 3.26 Seepage Outflow (28° flume slope) (64)
- Figure 3.27 Three dimensional general slip surface and forces acting on a typical column (65)
- Figure 3.28 A stage-state system and dividing scheme for a 3D slope (69)
- Figure 3.29 Columns between two adjacent stages  $i$  and  $i+1$  (69)
- Figure 3.30 Comparison of longitudinal profiles of experimental and simulated failure surfaces in side A (23° flume slope) (71)
- Figure 3.31 Comparison of longitudinal profiles of experimental and simulated failure surfaces at 20cm from side A (23° flume slope) (72)
- Figure 3.32 Comparison of longitudinal profiles of experimental and simulated failure surfaces at 40cm from side A (23° flume slope) (73)
- Figure 3.33 Comparison of longitudinal profiles of experimental and simulated failure surfaces at 60cm from side A (23° flume slope) (74)
- Figure 3.34 Comparison of longitudinal profiles of experimental and simulated failure surfaces in side B (23° flume slope) (75)
- Figure 3.35 Comparison of longitudinal profiles of experimental and simulated failure surfaces in side A (28° flume slope) (76)
- Figure 3.36 Comparison of longitudinal profiles of experimental and simulated failure surfaces at 20cm from side A (28° flume slope) (77)
- Figure 3.37 Comparison of longitudinal profiles of experimental and simulated failure surfaces at 40cm from side A (28° flume slope) (78)
- Figure 3.38 Comparison of longitudinal profiles of experimental and simulated failure surfaces at 60cm from side A (28° flume slope) (79)
- Figure 3.39 Comparison of longitudinal profiles of experimental and simulated failure surfaces in side B (28° flume slope) (80)
- Figure 3.40 3D view of experimentally observed failure surfaces (23° flume slope) (81)
- Figure 3.41 3D view of simulated failure surface using Janbu's simplified method, one-phase seepage analysis case (23° flume slope) (82)

- Figure 3.42 3D view of simulated failure surface using extended Spencer method, two-phase seepage analysis case (23° flume slope) (82)
- Figure 3.43 3D view of experimentally observed failure surfaces (28° flume slope) (83)
- Figure 3.44 3D view of simulated failure surface using Janbu's simplified method, one-phase seepage analysis case (28° flume slope) (83)
- Figure 3.45 3D view of simulated failure surface using extended Spencer method, two-phase seepage analysis case (28° flume slope) (84)
- 
- Figure 4.1 Typical schematic sample of stages, states and slip surface in a 2D slope (92)
- Figure 4.2 Grain size distribution of the sediment (94)
- Figure 4.3 Two dimensional dam body shape and size with the arrangements of WCRs (1-9) (95)
- Figure 4.4 Three dimensional dam body shape and size with the arrangements of WCRs (1-12) (95)
- Figure 4.5 Simulated and experimental moisture content profiles for constant head in upstream reservoir (WCRs – 4 to 9), 2D case (96)
- Figure 4.6 Simulated and experimental moisture content profiles for constant head in upstream reservoir (WCRs – 1 to 3), 2D case (97)
- Figure 4.7 Simulated and experimental failure surfaces for constant head in upstream reservoir (2D case) (97)
- Figure 4.8 Simulated and experimental moisture content profiles for steady discharge in upstream reservoir (WCRs – 4 to 9), 2D case (98)
- Figure 4.9 Simulated and experimental moisture content profiles for steady discharge in upstream reservoir (WCRs – 1 to 3), 2D case (99)
- Figure 4.10 Simulated and experimental failure surfaces for steady discharge in upstream reservoir (2D case) (99)
- Figure 4.11 Simulated and experimental moisture content profiles at WCRs 1- 6 (3D case) (101)
- Figure 4.12 Simulated and experimental moisture content profiles at WCRs 7- 12 (3D case) (102)
- Figure 4.13 Comparison of longitudinal profiles of experimental and simulated failure surfaces in side A (3D case) (103)
- Figure 4.14 Comparison of longitudinal profiles of experimental and simulated failure surfaces in side B (3D case) (104)

Figure 4.15 3D view of failure surface, computed by extended Spencer method (two-phase seepage consideration) (105)

Figure 4.16 Sensitivity of dam stability to variation on  $K_s$  (two-phase seepage consideration) (105)



## List of Tables

Table 2.1 Some parameter values of the sediment considered (20)

Table 2.2 Surface water forefront propagated time to measuring scales (29)

Table 3.1 Surface water forefront propagated time to measuring scales (23° flume slope) (64)

Table 3.2 Surface water forefront propagated time to measuring scales (28° flume slope) (64)

Table 3.3 Summary of slope stability analysis (23° flume slope) (84)

Table 3.4 Summary of slope stability analysis (28° flume slope) (84)

Table 4.1 Some parameter values of the sediment considered (94)

Table 4.2 Summary of slope stability analysis (28° flume slope) (106)



## **Curriculum Vitae**

Name            REGMI Ram Krishna

Citizenship    Nepal

Birth            1975 August 27, Gorkha, Nepal

Ph.D. Student (2008 - 2011)

Department of Civil and Earth Resources Engineering  
Kyoto University, Kyoto, Japan

M. Sc. in Water Resources Engineering (2003 - 2005)

Department of Civil Engineering, Institute of Engineering  
Tribhuvan University, Kathmandu, Nepal

B.E. in Civil Engineering (1996 - 2000)

Department of Civil Engineering, Institute of Engineering  
Tribhuvan University, Kathmandu, Nepal



## Papers based on the Thesis

Regmi, R.K., Nakagawa, H., Kawaike, K., Baba, Y. and Zhang, H.: Experimental and numerical study of rainfall induced slope failure, *Annals of the Disaster Prevention Research Institute*, Kyoto University, No.54B, October 2011. (to appear)

Regmi, R.K., Nakagawa, H., Kawaike, K., Baba, Y. and Zhang, H.: Three dimensional study of landslide dam due to sudden sliding, *Annual Journal of Hydraulic Engineering*, JSCE, Vol.55, pp.139-144, February 2011.

Regmi, R.K., Nakagawa, H., Kawaike, K., Baba, Y. and Zhang, H.: Three dimensional slope stability analysis of landslide dam failure by sudden sliding, *Proceedings of the Twelfth International Summer Symposium*, JSCE, Funabashi, Japan, pp.143-146, September 18, 2010.

Regmi, R.K., Nakagawa, H., Kawaike, K., Baba, Y. and Zhang, H.: Three dimensional analysis of landslide dam failure by sudden sliding, *Proceedings of the 29<sup>th</sup> Annual Meeting of the Japan Society for Natural Disaster Science*, pp.167-168, September 16-17, 2010.

Regmi, R.K., Nakagawa, H., Kawaike, K., Baba, Y. and Zhang, H.: Seepage and slope stability analysis of landslide dam, *International Symposium on a Robust and Resilient Society against Natural Hazards & Environmental Disasters and the Third AUN/SEED-Net Regional Conference on Geo-Disaster Mitigation*, Kyoto Univ., Japan, pp.361-370, August 24-26, 2010.

Regmi, R.K., Nakagawa, H., Kawaike, K., Baba, Y. and Zhang, H.: Analysis on sudden sliding of landslide dam due to transient seepage, *International Symposium on Sediment Disasters and River Environment in Mountainous Area*, JSPS Asia-Africa Science Platform Program, Kyoto, Japan, pp.45-46, August 24, 2010.

Regmi, R.K., Nakagawa, H., Kawaike, K., Baba, Y. and Zhang, H.: Two and three dimensional slope stability analysis of landslide dam failure due to sliding, *Annals of the Disaster Prevention Research Institute*, Kyoto University, No.53B, pp.617-627, Jun 2010.

Regmi, R.K., Nakagawa, H., Kawaike, K., Baba, Y. and Zhang, H.: Analysis of landslide dam failure due to transient seepage, *Proceedings of the International Symposium on Water and Sediment Disaster in East Asia*, Kyoto, Japan, pp.64-71, March 23-25, 2010.